Mathematical Modeling and Analysis of Cellular Clocks

by

Jae Kyoung Kim

A dissertation submitted in partial fulfillment
of the requirements for the degree of
Doctor of Philosophy
(Applied and Interdisciplinary Mathematics)
in the University of Michigan
2013

Doctoral Committee:

Associate Professor Daniel B. Forger, Co-Chair
Assistant Professor Victoria Booth, Co-Chair
Assistant Professor Marisa C. Eisenberg
Professor Trachette L. Jackson
Assistant Professor Lei Yin

To my lord and my family

ACKNOWLEDGEMENT

I have been very lucky to have had such great committee members from various areas who advised me throughout my graduate studies. First and foremost, I would like to express my deep gratitude to my advisor Daniel Forger for the tremendous amount of time spent for guiding me on how to conduct research, collaborate with experimental lab, write manuscripts, and balance life between work and family. These and so much more were all directed at helping me to become an independent scholar. I cannot imagine having a better advisor. I am also deeply grateful to my co-advisor, Victoria Booth, for her invaluable advise on neuronal modeling. In particular, without our many discussions on the different characteristics of neurons, I could not have come up with the idea of intercellular coupling of p53 pulses. I owe a debt of gratitude to Trachette Jackson for her advise on cancer modeling. It was great experience for me to study the p53 regulatory system with her. Furthermore, thanks to her, I could participate in the summer program at Mathematical Bioscience Institute (MBI), which a very timely opportunity that was pivotal in my decision to focus my research on mathematical biology. I would like to thank Lei Yin and Marisa Eisenberg for serving on my committee. I want to express my thanks to Lei Yin for providing me with an experimental point of view on circadian rhythms. I also would like to thank Marisa Eisenberg, for her advise on my next step, MBI post-doctoral life based on her previous experience.

I would also like to offer my sincere thanks to Sangkwon Chung and Onam Kwon at Seoul National University, who supported and encouraged me to pursue graduate study in the USA. Furthermore, your letters and annual Christmas cards on my desk have always encouraged me whenever I struggled with research.

I would like to thank Kevin Walton, Cheng Chang, and Travis Wager at Pfizer for wonderful collaboration. I want to thank Cheng for your kind advises for pharmacokinetics. I also would like to thank Kevin and Travis for sharing your valuable experimental data. I look forward to being involved in more of your exciting future work.

I would like to thank to many researchers at other universities, specifically Toru Takumi (RIKEN), Jihwan Myung (RIKEN), Hiroki Ueda (RIKEN), David Virshup (DUKE), Chris Hong (UC), Justin Blau (NYU), John Hogenesch (U Penn) and Choogon Lee (FSU) for valuable discussions on my research on circadian rhythms. I also would like to thank Gait Lahav (Harvard) for the great feedback on my p53 pulses research.

I am grateful for my fellow students in Math, who made my life at Michigan much more pleasurable. In particular, I will remember every moment of the games with my basketball team, the Math All Stars. I also thank the present and past members of mathematical biology community, in particular Santiago Schnell, David Lubensky, Yangjin Kim, Richard Yamada, Justin Dunmyre, Seth Marvel, Daniel DeWoskin, and Olivia Walch for all valuable discussions. I would like to thank my program director, Peter Miller and other staff for all your support for my graduate studies. I thank a course coordinator, Yvonne Lai for recognizing my passion for teaching and giving me a chance to mentor new international graduate student instructors. I also thank Chris Feak at ELI for her sincere advice for my academic writing throughout my graduate studies. I also thank Matthew Bennet for technical support for high performance computing.

I would like to acknowledge the financial support that I received from the Air Force, Pfizer and the Human Frontier Science Program. I am also grateful to the Rackham School of Graduate Studies for awarding me the Rackham International Student Fellowship and many travel grants.

I also would like to thank members of Campus Town Church of Ann Arbor for their prayers and making my life at Michigan so joyful. I would especially like to express my thanks to Ps. Sang Samuel Park for his prayers and for giving me a chance to serve on our church's board.

My heartfelt thanks go out to my wife, Kyunga Jun. Without her sincere support and love, I could not have completed this thesis. My son, Minchai and daughter, Eunchai have been a great joy of my life and their smile greeting has always released all of my stress from the work. Finally, my deepest appreciation goes out to my parents and my parents-in-law for their supports, encouragement and love.

PREFACE

The work in Chapter 2 and 3 of this dissertation was advised by Daniel Forger. Chapter 2 was previously published as: JK Kim and DB Forger, *SIAM J. APPL. MATH.*, 72: 1842-1855 (2012). Chapter 3 consists of two previously published papers: JK Kim and DB Forger, *Molecular Systems Biology* 8, (2012) and JK Kim, DB Forger, M Marconi, D Wood, A Doran, TT Wager, C Chang and K Walton, *CPT:Pharmacometrics & Systems Pharmacology* 2 (2013).

The work in chapter 4 was advised by Trachette Jackson. Chapter 4 was previously published as: JK Kim and TL Jackson, *PLOS ONE* 8 (2013)

TABLE OF CONTENTS

LIST OF FIGURES

LIST OF TABLES

LIST OF APPENDICES

Chapter 1 Introduction

The cell has various biological clocks that generate rhythms with periods from seconds to weeks. These rhythms control important aspects of cell physiology including cell division, embryogenesis, DNA damage repair and metabolism (1-4), which are essential functions for the survival of organisms. For instance, circadian (~24hr) rhythms control daily events, such as the sleep/wake cycle, blood pressure, body temperature and hormone (e.g. melatonin) secretion, which allow organisms to adapt to the appropriate time of day (5). Another interesting cellular rhythm is the oscillation of p53 (a tumor suppressor), which is essential to repair DNA damage (6). The oscillations of cell cycle also control cell growth and division (7).

These cellular rhythms can be disrupted in various ways including mutation of genes, which has a profound effect on the function of the cell. The importance of maintaining cellular rhythms has led to considerable research interest in mechanisms that generate and maintain these rhythms (2, 4, 8). In particular, since the molecular biology revolution of the 1980s, many genes and proteins that constitute biochemical networks involving cellular rhythms have been identified (9-12). The identification of these biochemical networks has provided a fundamental framework to study cellular rhythms (13) and has significantly improved our understanding of cellular rhythms (4). However, despite a tremendous amount of experimental work since the 1980s, our understanding of these biochemical networks is still far from complete due to limitations of current experimental techniques (13-17).

In chapter 2, we proposed a new approach to reveal biochemical networks underlying biological clocks. While detecting biochemical interactions and measuring their biochemical rate constants requires a tremendous amount of experimental work, measuring the timecourse of these components is relatively easy with advanced techniques, such as luciferase assay and microarray analysis (18, 19). Given the amount of timecourse data, we sought to answer the following question: “If we can accurately record the timecourses of genes and proteins in a biological clock, what can we infer about the biochemical network generating the rhythms?” We formulated this question as an existence and uniqueness problem and proved that the network interactions, and even biochemical rates, can sometimes uniquely be determined from only gene and protein timecourses. This theory provides a simple algorithm that determines whether two given species have a biochemical interaction based on their timecourses. We also showed that the repetitive application of this algorithm to all pairs of species in the network can reveal the global structure of biochemical networks.

While revealing biochemical networks is an important step towards the understanding of biological clock functions, having complete knowledge of the biochemical network structure does not give a complete understanding of biological clock function. That is, even with the knowledge of all the components and interactions that constitute biological clocks, further studies are needed to understand the following questions: Why does the loss of some components completely disrupt rhythms, while the loss of other components cause little effect on them? Why does the loss of some components increase period or amplitude, but the loss of other components decrease period or amplitude? To answer these fundamental questions regarding cellular rhythms, biochemical interactions underlying biological clocks should be studied systemically (4, 8, 20). In this systematic approach, mathematical modeling has been an important tool (2, 8). That is, simulation and analysis of mathematical models of biological clocks allow for a integrative interpretation of data, illumination core dynamics, and explanation of the role of each component underlying biological clocks (2, 4, 7, 8, 21-23). For instance, mathematical models have found core mechanisms for rhythm generation in various cellular rhythms, such as circadian rhythms, cell cycle and p53 rhythms (2, 4, 8, 20). Furthermore, mathematical modeling found that the positive feedback loop that is commonly observed in various biological clocks is essential to maintain rhythms over a wide range of conditions and tune periods (3).

In chapter 3, we studied how molecular circadian clocks generate rhythms and maintain a 24-hour period over a wide range of conditions by developing the most detailed and accurate mathematical model of this system to date. This model was developed by piecing together data from accumulated experimental studies published in the last two decades. In particular, the model accurately reproduces the phenotype of known mutations of genes in the circadian clock, which was not achieved by previous models. By analyzing the simulations of various mutant phenotypes, we found an essential condition for rhythm generation and period regulation: a 1-1 stoichiometric balance between activators and repressors of a core negative feedback loop in the circadian clocks (i.e. a similar ratio between the amount of activators and repressors). Furthermore, we found that an additional negative feedback loop in the circadian clock helps maintain a 1-1 stoichiometric balance, leading to rhythm generation and tight regulation of period over a wide range of conditions. We also verified that these properties are sufficient to generate rhythms whose period shows little change over a wide range of conditions by developing and analyzing a simple model based on these properties. Finally, by using the detailed mathematical model, we explored how the phases of circadian rhythms can be manipulated pharmacologically. This pharmacological modulation of circadian phase points to a novel way to treat the misalignment of circadian clocks, which increase the risk of various diseases including depression, insomnia, jet lag, coronary heart disease, neurodegenerative disorders, and cancer (24).

In Chapter 4, we explored another type of cellular rhythm, namely p53 rhythms. p53 protein is one of the most important tumor suppressors, which regulates key functions to prevent tumorigenesis in response to cellular stress (e.g. DNA damage and genomic instability), such as DNA repair, cell cycle arrest and apoptosis (25). While a low p53 level is maintained in the normal condition, the level of p53 becomes rhythmic in response to cellular stresses, such as γ-irradiation that induces DNA damage (26). Recent study found that sustaining p53 pulses is essential to repair DNA damage and to prevent tumorigenesis (6). However, little research has investigated how cells can sustain p53 pulses even with genetic heterogeneity, intrinsic noise and different environmental conditions. We investigated mechanisms that enhance the sustainability of p53 pulses by developing a mathematical model of the p53 rhythm regulatory system. First, we found that an additional intracellular positive feedback loop is important for sustaining p53 rhythms. That is, when the recently identified positive feedback loop between p53 and Rorα is included in the currently known p53 rhythm regulatory system, the sustainability of p53 rhythms is significantly improved over a wide range of conditions. We also found that DNA damaged cells behave like type II neurons, which act as resonators. The fact that type II neurons easily synchronize their rhythms when they are coupled led to the question of whether neighboring cells also synchronize p53 rhythms. We found that Cytochrome-c, which is known to induce a radiation induced bystander effect (27), can be a potential coupling signal and can synchronize p53 rhythms among neighboring cells after DNA damage. Interestingly, the coupling also significantly reduces the chance of failure in sustaining p53 pulses in the presence of heterogeneity among cells. In summary, this work points to the importance of both intra and inter cellular positive feedback loops via Roaα and Cytochrome-c in sustaining p53.

In Chapter 5, we review these studies and highlight the importance of our mathematical approaches on solving fundamental problems of cellular rhythms. Furthermore, we also propose future directions to expand these studies.

Chapter 2 On the Existence and Uniqueness of Biological Clock Models Matching Experimental Data

2.1 Introduction

A tremendous amount of data has become available on biological clocks during the past 15 years. Most of this data comes in the form of timecourses, i.e. measurements over time of the concentrations of chemical species with GFP (green fluorescent protein), luciferase, or microarray techniques. Many mathematical modeling studies have used timecourse data to estimate the parameters of their models (e.g. (28, 29)). This raises the question of whether timecourses can do more than the parameter estimation. That is, can timecourses reveal information about network structure?

We answer this question with a common form of ordinary differential equation (ODE) models for biological clocks (30-32):

$$\frac{dr}{dt} = f(s) - g(r) \tag{1.1}$$

in which $f(s)$ represents the production of a species r (e.g. protein or gene) based on some other species, s in the network and $g(r)$ is the rate of clearance of r. Here, we consider the following questions: given precise measurements of two oscillating timecourses $r(t)$ and $s(t)$ with the same period,

Question 1. (existence) Can we find f and g such that the solution of (1.1) matches the given timecourses $r(t)$ and $s(t)$?

Question 2. (uniqueness) If we can find f and g, are they unique?

The existence of f and g implies that the production of r is controlled by s. The uniqueness of f and g implies that the timecourses are enough to determine the quantitative relationships (i.e. biochemical rates).

The questions we ask here are related to several other well-studied problems.

1) Control theorists consider a related problem called "identifiability" (33, 34). This problem usually focuses on the identification of parameters of a given ODE with control of inputs and measurable outputs (e.g. timecourses). Here, we look for functions of ODEs rather than parameters of ODEs matching timecourses without control of input.

2) Symbolic dynamics and reverse engineering techniques have been used to determine the qualitative functional relationships between species (i.e. whether activation or repression occurred) (35-38). Here, we pursue more detailed information. For instance, we ask whether the timecourses contains information for the quantitative relationship (e.g. determining f and g) as well as qualitative relationships.

3) Recently, harmonic balance techniques have been proposed to select an ODE model from a class of models based on the best match to given oscillating timecourses (39, 40). However, here we search for the models matching timecourses exactly, instead of selecting an ODE matching timecourses better than the other candidates.

4) One of the classical results in the theory of ODEs is that, given a sufficiently smooth ODE and an initial condition, a unique solution exists (41). Here, we ask the opposite question: Given the oscillating solution of an ODE, can we find an ODE matching this solution, and is this ODE unique?

5) Chemical reaction network theory has shown that the same ODE system may result from different reaction network diagrams (42). Here, we study the relationship between the ODE model and timecourses rather than that between the ODE model and reaction network. A previous study often equates dynamics (i.e. timecourses of key chemical species) with an ODE model (42). However, in practical applications, an ODE model is rarely known, and almost never known fully. Thus, it is important to know how the timecourses determine ODE dynamics.

Our main finding is a necessary condition for Question 1 that provides a tool for detecting the relationship among the species solely from their timecourses. We also find necessary and sufficient conditions for Question 2, when timecourse data is enough to determine an ODE model of the form (1.1) uniquely. Finally, we show that another class of models of the form (1.2) (previously proposed in (17)), as well as the class of models of the form (1.3) have uniqueness and existence over a broad class of timecourses:

$$\frac{df(r)}{dt} = s + g(r), \tag{1.2}$$

$$\frac{dr}{dt} = f(r)s - g(r). \tag{1.3}$$

This chapter is organized in the following way. In section 2.2, we outline our results. In section 2.3, we present the necessary conditions for existence of (1.1) and examples to show how it can reveal the structure from timecourse data. In section 2.4, we present the necessary and sufficient conditions for uniqueness of (1.1). Section 2.5 demonstrates that existence and uniqueness hold for (1.2) and (1.3).

2.2 Overview of existence and uniqueness of models

Definition 2.1. *$r(t)$ and $s(t)$ are smooth oscillating timecourses with period τ (τ-periodic) and with one maximum and one minimum per period.*

In this paper, we consider only smooth (C^∞) functions because most biological problems are smooth. However, most of the results still hold when this assumption is relaxed.

Definition 2.2. *If* $k(t)$ *is a smooth timecourse with period* τ *and with one maximum and one minimum over a period, then* $\hat{k}(t):[-\tau/2,\tau/2)\to[-\tau/2,\tau/2)$ *is a one to one function such that* $k(\hat{k}(t))=k(t)$ *and* $\hat{k}(t)\neq t$ *unless t is a maximum or minimum of* $k(t)$.

For example,

$$\hat{\cos}(2\pi t/\tau)=\begin{cases} -t & -\tau/2<t<\tau/2 \\ -\tau/2 & t=-\tau/2 \end{cases}$$

and

$$\hat{sin}(2\pi t/\tau)=\begin{cases} -t+\tau/2 & 0<t<\tau/2 \\ -t-\tau/2 & -\tau/2\le t\le 0 \end{cases}$$

Definition 2.3. *Given* $r(t)$ *and* $s(t)$, $\phi(t):=\hat{s}(\hat{r}(t))$.

Our results are described in Figure 2-1. The fixed points of $\phi(t)$ and its iteration $\phi^n(t)$ play a pivotal role in determining the existence and uniqueness of models given timecourses $r(t)$ and $s(t)$. Theorem 3.1 shows that the existence of fixed points satisfying (3.2) implies the non-existence of (1.1). Theorem 4.3 shows that a model of the form (1.1) is unique as long as the set of fixed points is of measure zero. Theorem 5.2 shows the existence and uniqueness of (1.2) for a broad class of timecourses. Theorem 5.3 shows that (1.2) can be converted into a more canonical form (1.3) if $\phi(t)$ does not have a fixed point.

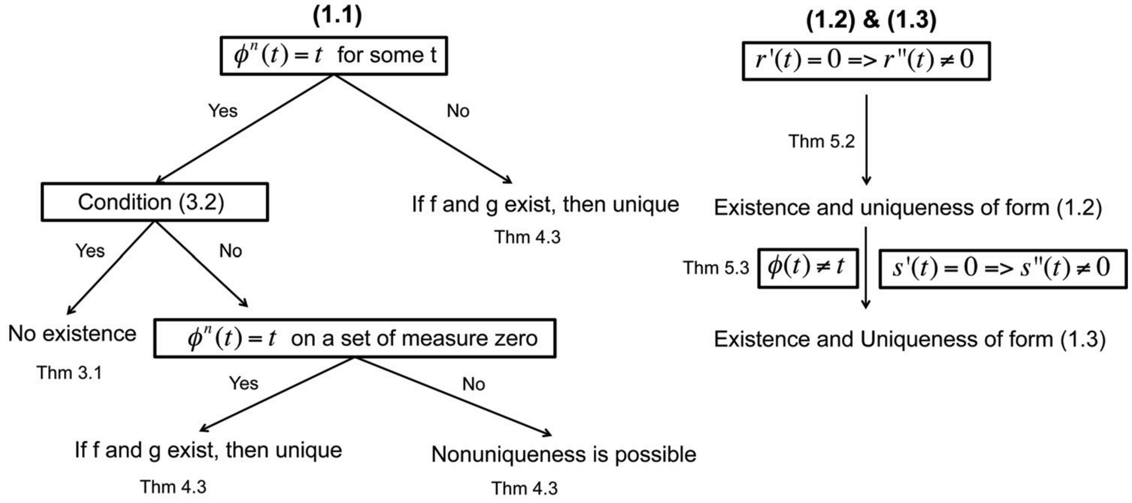

Figure 2-1. Existence and uniqueness of *f* and *g* of forms (1.1), (1.2) and (1.3) matching timecourses *r*(*t*) and *s*(*t*) .

2.3 A Necessary condition for the existence of form (1.1)

THEOREM 3.1. *If there exist a* $\hat{t} \in [-\tau/2, \tau/2)$ *and an* $n \in N$ *for* $r(t)$ *and* $s(t)$ *such that*

(3.1) $\phi^n(\hat{t}) = \hat{t}$

(3.2) $$\frac{dr}{dt}_{t=\hat{t}} + \frac{dr}{dt}_{t=\phi(\hat{t})} + \dots + \frac{dr}{dt}_{t=\phi^{n-1}(\hat{t})} \neq \frac{dr}{dt}_{t=\hat{r}(\hat{t})} + \frac{dr}{dt}_{t=\hat{r}(\phi(\hat{t}))} + \dots + \frac{dr}{dt}_{t=\hat{r}(\phi^{n-1}(\hat{t}))},$$

then functions f and g *of form* (*1.1*) *do not exist.*

Proof. This can be proved by showing that if there exist f and g satisfying (1.1), then (3.1) implies the equality in (3.2).

Equation (3.1) implies that

(3.3) $$\hat{t} = t_0 \xrightarrow{\hat{r}} t_1 \xrightarrow{\hat{s}} t_2 \xrightarrow{\hat{r}} t_3 \dots \xrightarrow{\hat{s}} t_{2n-2} \xrightarrow{\hat{r}} t_{2n-1} \xrightarrow{\hat{s}} t_0 = \hat{t}\ .$$

Since $\hat{r}^{-1}(t) = \hat{r}(t)$ and $\hat{s}^{-1}(t) = \hat{s}(t)$,

$$(3.4)\quad \hat{t} = t_0 \xleftarrow{\hat{r}} t_1 \xleftarrow{\hat{s}} t_2 \xleftarrow{\hat{r}} t_3 .... \xleftarrow{\hat{s}} t_{2n-2} \xleftarrow{\hat{r}} t_{2n-1} \xleftarrow{\hat{s}} t_0 = \hat{t}$$

Let us show that (3.1) implies the equality in (3.2). If we assume that there exist f and g satisfying (1.1), then

$$\begin{aligned}
&\left.\frac{dr}{dt}\right|_{t=\hat{t}} + \left.\frac{dr}{dt}\right|_{t=\phi(\hat{t})} + ... + \left.\frac{dr}{dt}\right|_{t=\phi^{n-1}(\hat{t})} \\
(3.5)\quad &= f(s(\hat{t})) - g(r(\hat{t})) + f(s(\phi(\hat{t}))) - g(r(\phi(\hat{t}))) + ... + f(s(\phi^{n-1}(\hat{t})) - g(r(\phi^{n-1}(\hat{t})) \\
&= f(s(t_0)) - g(r(t_0)) + f(s(t_2)) - g(r(t_2)) + ... + f(s(t_{2n-2})) - g(r(t_{2n-2})) \\
&= (f(s(t_0)) + f(s(t_2)) + ... + f(s(t_{2n-2}))) - (g(r(t_0)) + g(r(t_2)) + ... + g(r(t_{2n-2})))
\end{aligned}$$

Since $r(\hat{r}(t)) = r(t)$, $s(\hat{s}(t)) = s(t)$, and (3.4),

(3.6)

$$\begin{aligned}
&(f(s(t_0)) + f(s(t_2)) + ... + f(s(t_{2n-2}))) - (g(r(t_0)) + g(r(t_2)) + ... + g(r(t_{2n-2}))) \\
&= (f(s(\hat{s}(t_0))) + f(s(\hat{s}(t_2))) + ... + f(s(\hat{s}(t_{2n-2})))) - (g(r(\hat{r}(t_0))) + g(r(\hat{r}(t_2))) + ... + g(r(\hat{r}(t_{2n-2}))) \\
&= (f(s(t_{2n-1})) + f(s(t_1)) + ... + f(s(t_{2n-3}))) - (g(r(t_1)) + g(r(t_3)) + ... + g(r(t_{2n-1}))) \\
&= f(s(t_1)) - g(r(t_1)) + f(s(t_3)) - g(r(t_3)) + ... + f(s(t_{2n-1})) - g(r(t_{2n-1})) \\
&= r'(t_1) + r'(t_3) + ... + r'(t_{2n-1}) \\
&= \left.\frac{dr}{dt}\right|_{t=\hat{r}(\hat{t})} + \left.\frac{dr}{dt}\right|_{t=\hat{r}(\phi(\hat{t}))} + ... + \left.\frac{dr}{dt}\right|_{t=\hat{r}(\phi^{n-1}(\hat{t}))}
\end{aligned}$$

.

Equations (3.5) and (3.6) imply that if there exist f and g satisfying (1.1), then (3.1) contradicts (3.2). Therefore, conditions (3.1) and (3.2) imply that f and g of (1.1) do not exist. □

A simple example to illustrate Theorem 3.1 is provided in Figure 2-2. Since $\phi(t_0) = \hat{s}(\hat{r}(t_0)) = \hat{s}(t_1) = t_0$, both $r(t)$ and $s(t)$ have the same value at t_0 and t_1, so both

$g(r(t))$ and $f(s(t))$ do as well. This implies the equality of (3.2) or $r'(t_0) = r'(t_1)$ if there exists a model (1.1). However, $r'(t_0) \neq r'(t_1)$ unless $r'(t_0) = 0$ and $r'(t_1) = 0$ since the signs of $r'(t_0)$ and $r'(t_1)$ are opposite (Figure 2-2). Therefore, the condition (3.1) implies the non-existence of the model (1.1) unless $r'(t_0) = 0$ and $r'(t_1) = 0$.

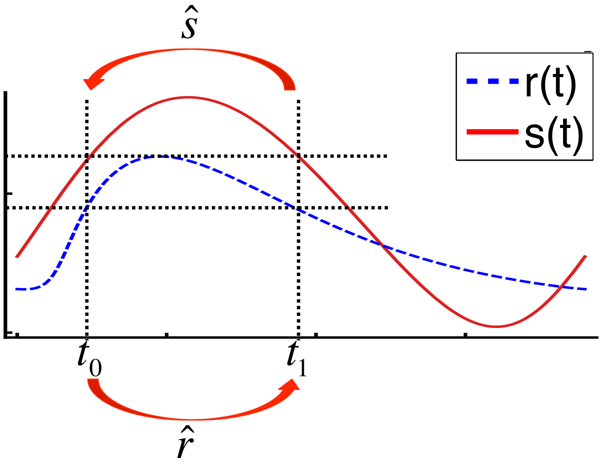

Figure 2-2. Fixed point of $\phi(t)$ implies the non-existence of the model (1.1).

Theorem 3.1 provides a way to determine the structure of the molecular network by showing the non-existence of (1.1) among unrelated species. Let us apply this to reveal the structure of biological clock model (3.7) based on the Goodwin oscillator (30-32).

$$\begin{aligned} \frac{dm}{dt} &= \frac{1}{1+p_4^{10}} - 0.4m \\ \frac{dp_1}{dt} &= m - 0.4p_1 \\ \frac{dp_2}{dt} &= p_1 - 0.4p_2 \\ \frac{dp_3}{dt} &= p_2 - 0.4p_3 \\ \frac{dp_4}{dt} &= p_3 - 0.4p_4 \end{aligned} \tag{3.7}$$

Simulating this model generates 5 timecourses, which are interrelated in a single negative feedback loop. From these timecourses, we seek to reconstruct the model's structure, without knowledge of (3.7). Given the 5 timecourses, 10 interactions are possible of the form given in (1.1) (see Figure 2-3C). Can Theorem 3.1 be used to find the relevant interactions? To determine whether two components of the system are related via (1.1) with Theorem 3.1, we check whether there exist some t obeying (3.1) and at that t, (3.2) is also satisfied. As shown in Figure 2-3A, we find that there exists t such that $\phi^2(t) = t$ as well as (3.2) are satisfied between the pair $m(t)$ and $p_3(t)$, and the pair $p_1(t)$ and $p_4(t)$. Thus, we can rule out these interactions. In a similar way, by checking $\phi^3(t) = t$ and (3.2), three more interactions are excluded: $m(t)$ and $p_2(t)$, $p_1(t)$ and $p_3(t)$, and $p_2(t)$ and $p_4(t)$ (Figure 2-3B). The only remaining interactions now match the original feedback loop structure (Figure 2-3C). Thus from the timecourse data and Theorem 3.1, we were able to reconstruct the original feedback loop.

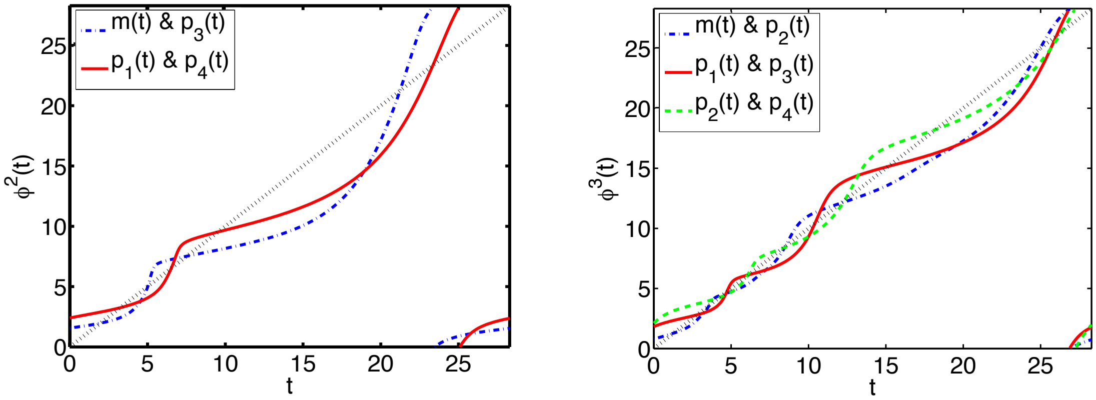

A. $\varphi^2(t) = t$ B. $\varphi^3(t) = t$

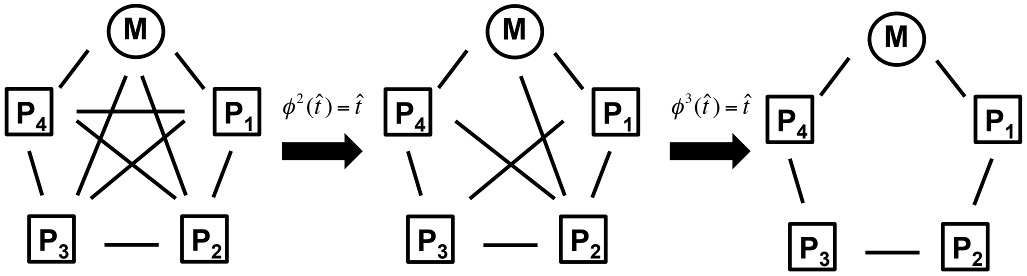

C. Reconstruction of (3.7)

Figure 2-3. Theorem 3.1 excludes unrelated pair of signals of (3.7), so the original feedback loop structure is identified from the timecourses.

We also apply Theorem 3.1 to another problem to determine whether it can be used to distinguish between two independent Goodwin oscillators. For this, we construct two

Goodwin oscillators with different Hill-coefficients, (3.8) and (3.9). By choosing *ts* =1.356 in all the reactions of (3.9), we can match the periods of (3.8) and (3.9).

$$
\begin{aligned}
\frac{dM}{dt} &= \frac{1}{1+P_2^9} - 0.1M \\
\frac{dP_1}{dt} &= M - 0.1P_1 \\
\frac{dP_2}{dt} &= P_1 - 0.1P_2
\end{aligned}
\tag{3.8}
$$

$$
\begin{aligned}
\frac{dN}{dt} &= ts(\frac{1}{1+Q_2^{20}} - 0.1N) \\
\frac{dQ_1}{dt} &= ts(N - 0.1Q_1) \\
\frac{dQ_2}{dt} &= ts(Q_1 - 0.1Q_2)
\end{aligned}
\tag{3.9}
$$

There are 15 possible interacting pairs between the 6 variables of (3.8) and (3.9) (e.g. Q_1 and M, and P_1 and P_2) (see Figure 2-4). For 2 pairs of variables, there exists a *t* such that $\phi(t) = t$ as well as (3.2), which means they are not related. By checking $\phi^2(t) = t$, 4 more pairs are excluded. $\phi^3(t) = t$ excludes 1 more pair. Now, 7 pairs among the original 15 pairs are excluded. By comparing them with (3.8) and (3.9), we see that 7 of the 9 unrelated pairs are correctly excluded. This shows how Theorem 3.1 can be used to identify incorrect functional relationships between variables and reveal the structure.

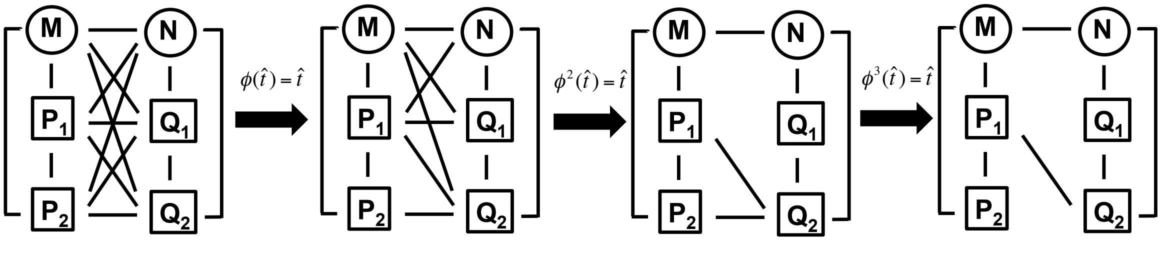

Figure 2-4. Theorem 3.1 excludes most of unrelated two components of two independent Goodwin oscillators, (3.8) and (3.9). (Initial condition used: M(0)=0.0227, $P_1(0)$=0.1472, $P_2(0)$=1.7531, N(0)=0.0034, $Q_1(0)$=0.1269, and $Q_2(0)$=2.4147).

Theorem 3.1 considers a simple model (1.1), in which each component is regulated by only one other component. However, in real biological systems, this assumption may be too simplistic. If more than one component, s_1, s_2, …, s_n controls the production of a chemical species, we have the following form:

$$\frac{dr}{dt} = f(s_1, s_2 ...., s_n) - g(r)$$

One particular case of this is

$$\frac{dr}{dt} = f_1(s_1) + f_2(s_2) - g(r),$$

where we have more freedom to choose f_1 and f_2 than if we can choose only one f as in (1.1). Therefore, we can expect that the existence is more likely to occur as more species or variables are included in the model. Since $\phi(t) = \hat{s}(\hat{r}(t))$ plays the key role in the study of (1.1), similar techniques could be used to study the generalized models by finding a new version of $\phi(t) = \hat{s}(\hat{r}(t))$, which describes the relationship of more than two timecourses. It may also be helpful to experimentally keep some of the signals, (e.g. s_2, s_3, …) constant, which would reduce the problem to that of the form (1.1).

2.4 Necessary and sufficient conditions for uniqueness of form (1.1)

Given two timecourses, for which an appropriate f and g of (1.1) can be found, we next consider whether the functions f and g are unique? One trivial way to achieve non-uniqueness is to add the same constant to both f and g since we are concerned only with their difference in the ODE. To avoid this, we assume that $f(0) = 0$. However, as shown by the following theorem, this alone does not guarantee uniqueness.

THEOREM 4.1. *Given two timecourses* $r(t)$ *and* $s(t)$, *for which* f *and* g *of* (*1.1*) *exist, smooth functions* f and g *are unique if and only if there are no smooth functions m and n such that*

$$m(s(t)) = n(r(t)) \text{ and } m(0) = 0 . \tag{4.1}$$

Proof. (only if). Let us assume that there are f_1, g_1, f_2 and g_2 such that

$$\frac{dr}{dt} = f_1(s) - g_1(r) = f_2(s) - g_2(r) .$$

By defining,

$$m(s) := f_1(s) - f_2(s),$$
$$n(r) := g_1(r) - g_2(r),$$

we show that $m(s)=n(r)$ and $m(0)=f_1(0) - f_2(0) = 0 – 0 =0$.

(If). Now, let us assume there exist *m* and *n* such that $m(s) = n(r)$ and $m(0) = 0$ and show that f and g of (1.1) are not unique. Then,

$$\frac{dr}{dt} = f(s) - g(r) = f(s) + m(s) - n(r) - g(r) .$$

Let

$$\begin{aligned} \tilde{f}(s) &:= f(s) + m(s), \\ \tilde{g}(r) &:= g(r) + n(r). \end{aligned} \tag{4.2}$$

Then, $r(t)$ and $s(t)$ become solutions of (1.1) with these new functions and $\tilde{f}(0) = f(0) + m(0) = 0 + 0 = 0$. □

The class of functions $s(t)$ and $r(t)$, which do not have uniqueness is not apparent immediately since determining the existence of *m* and *n* such that $m(s) = n(r)$ is difficult, especially when non-monotonic m and n are allowed. The following corollary is useful in seeing how large the space of $s(t)$ and $r(t)$ with non-unique f and g is.

COROLLARY 4.2 *Given two timecourses* $r(t)$ *and* $s(t)$*, for which* f *and* g *of* (*1.1*) *exist, smooth functions* f and g *are unique if and only if there is no smooth function m such that*

$$m(s(-t')) = m(s(t'))\ and\ m(0) = 0 \tag{4.3}$$

for the scaling of time $t'(t)$*, with which* $r(t')$ *is an even function.*

Proof. We can shift time so that $r(t)$ has a maximum at *t=0*. Then, we can always find the scaling of time $t'(t)$, with which $r(t')$ becomes an even function (see [3] for details). Then, $n(r(t'))$ of (4.1) also becomes an even function. This causes the non-uniqueness condition (4.1) with respect to the scaling of time $t'(t)$ to be that $m(s(t'))$ is an even function. □

This corollary shows that if *f* and *g* of (1.1) exist given $r(t)$ and $s(t)$, then *f* and *g* are not unique when $s(t)$ is in the preimage of an oscillating even function with time scaled so that $r(t)$ becomes an even function. The preimage of oscillating even functions is broad and contains even functions, odd functions, simple harmonic functions $\sin(t + m\pi / n)$, and so on. At first glance, non-uniqueness seems to frequently occur because, regardless of what $r(t)$ is, there always exists a large space (the preimage of oscillating even functions in the new scaling of time) of $s(t)$, in which nonunique *f* and *g* of (1.1) exist. However, the following theorem shows that non-uniqueness is less likely to occur by showing that an $s(t)$ which is the preimage of oscillating even function cannot be a solution of (1.1) in most cases.

THEOREM 4.3. *Given timecourses* $r(t)$ *and* $s(t)$*, for which* f *and* g *of* (*1.1*) *exist,* f and g *of form (1.1) are unique if and only if* $\phi^n(t) \neq t$ *for almost every* t *and for all* $n \in N$.

Proof (If). Let us assume that there exist non-unique f and g of (1.1) or that $m(s(t'))$ is an even function for the scaling of time $t'(t)$ for which $r(t')$ is an even function by Corollary 4.2. Since $m(s(t'))$ is an even function and $\hat{r}(t') = -t'$ on $(-\tau/2, \tau/2)$,

$$m(s(t')) = m(s(-t')) = m(s(\hat{r}(t'))) . \tag{4.4}$$

Since $s(\hat{r}(t')) = s(\hat{s}(\hat{r}(t')))$ by definition of $\hat{s}(t)$,

$$m(s(\hat{r}(t')) = m(s(\hat{s}(\hat{r}(t'))) = m(s(\phi(t'))) . \tag{4.5}$$

Therefore, (4.4) and (4.5) imply that $m(s(t'))$ has the same value for t' and $\phi(t')$. By applying the same argument for $\phi(t')$ instead of t', we can show that $m(s(t'))$ has the same value for the following set:

$$\{t', \phi(t'), \phi^2(t'), ..., \phi^n(t'), ...\} .$$

By scaling back to the original time scale, $m(s(t))$ has the same value for

$$\{t, \phi(t), \phi^2(t), ..., \phi^n(t), ...\} \tag{4.6}$$

Since $\phi^n(t) \neq t$ for almost every t and for all $n \in N$, (4.6) is an infinite set for almost every t. Therefore, if $\phi^n(t) \neq t$, the set of (4.6) has at least one limit point, where $m(s(t))$ is a locally recurrent function. If we define L as a set of points where $m(s(t))$ is locally recurrent, $m(s(L))$ is of measure zero since $m(s(t))$ has finite derivative (43). Furthermore, if we define K as a set of points such that $\phi^n(t) = t$ for some $n \in N$, $m(s(K))$ is of measure zero since K is of measure zero. Since the range of $m(s(t))$ is the same with $m(s(L)) \cup m(s(K))$, the range of $m(s(t))$ is also of measure zero or $m(s(t))$ is a constant function (zero function since $m(0) = 0$). Therefore, $\phi^n(t) \neq t$ for almost every t and for all $n \in N$ implies that a non-trivial function m cannot satisfy (4.1) and (4.3).

(Only if). If the measure of fixed points is not zero or $\mu\left\{t \middle| \phi^n(t) = t\right\} \neq 0$, and assuming that $n \in N$ is the minimal value for which the measure of the set is nonzero, we can find a closed interval $A_1 = [\alpha, \beta] \subset \left\{t \middle| \phi^n(t) = t\right\}$ since $\phi^n(t)$ is smooth except at a finite number of points. We now show that this implies the existence of m and n as in (4.1). Since $\phi^n(A_1) = A_1$,

$$(4.7)\ A_1 \xrightarrow{\hat{r}} B_1 \xrightarrow{\hat{s}} A_2 \xrightarrow{\hat{r}} B_2 .... \xrightarrow{\hat{s}} A_{n-1} \xrightarrow{\hat{r}} B_{n-1} \xrightarrow{\hat{s}_i} A_1$$

We can always make $r(t)$ and $s(t)$ monotone over A_i by reducing the size of A_1 (see Figure 2-5). Similarly, we can always reduce the size of A_1 to ensure that there is no intersection between the images of $r(t)$ over A_i and A_j unless i=j. Similarly, we can also ensure that the images of $s(t)$ over A_i and A_j do not intersect unless i=j. We now show that over these regions A_i, we can find $m(s(t))$ and $n(r(t))$ satisfying (4.1) or $m(s(t))$=$n(r(t))$. Choose any nonzero smooth function $n(r(t))$ over A_1 such that $\frac{d^k n(r(t))}{dt^k} = 0$ for all k at the boundary of A_1 (Figure 2-5). This function can be extended over A_1^C as below:

$$n(r(t)) = \begin{cases} 0 & t \notin A_i \, and \, t \notin B_i \\ n(r(\phi^{-(i-1)}(t))) & t \in A_i \;\; for \; i = 2, 3, \ldots, n-1 \\ n(r(\phi^{-(i-1)}(\hat{r}(t)))) & t \in B_i \;\; for \; i = 1, 2, \ldots, n-1 \end{cases} \tag{4.8}$$

$m(s(t))$ can also be chosen to match $n(r(t))$:

$$m(s(t)) = \begin{cases} 0 & t \notin A_i \, and \, t \notin B_i \\ n(r(t)) & t \in A_i \;\; for \; i = 1, 2, \ldots, n-1 \\ n(r(\hat{s}(t))) & t \in B_i \;\; for \; i = 1, 2, \ldots, n-1 \end{cases} \tag{4.9}$$

Thus $m(s(t))=n(r(t))$ and f and g are not unique by Theorem 4.1. □

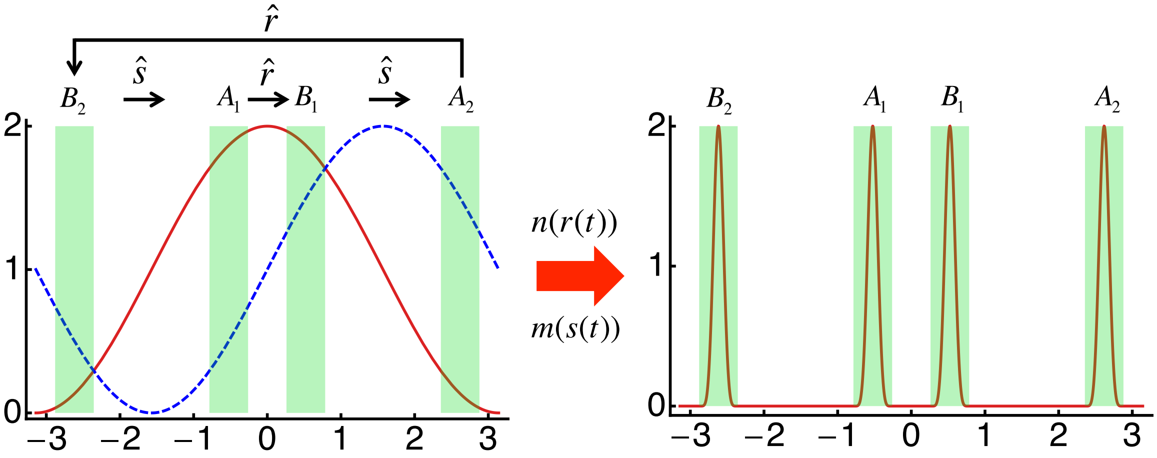

Figure 2-5. Description of the construction of *n*(*r*(*t*)) and *m*(*s*(*t*)) such that *n*(*r*(*t*))=*m*(*s*(*t*)).

Theorem 4.3 and Theorem 3.1 indicate that nonuniqueness rarely occurs since the equality of (3.2) must hold over a non-measure zero set, $\left\{t \middle| \phi^n(t) = t\right\}$. Moreover, Theorem 4.3 provides a way to test whether *f* and *g* of (1.1) are unique. If there exists a non-measure zero set where $\phi^n(t) = t$ for some $n \in N$, *f* and *g* will not be unique if they exist (Figure 2-1). If the measure of all fixed points is zero, and *f* and *g* of (1.1) exist, *f* and *g* will be unique (Figure 2-1).

2.5 Sufficient conditions for existence and uniqueness of (1.2) and (1.3).

Here, we show that existence and uniqueness can be achieved in the broader class of timecourses by considering another form of ODE models (1.2). Our previous study found that for smooth timecourses $r(t)$ and $s(t)$, (1.2) could be constructed if $dr/dt = 0 \Rightarrow d^2r/dt^2 \neq 0$ (17). That is, for this class of functions $r(t)$, f and g of form (1.2) exist. Here, we show that f and g of form (1.2) are also unique. To show uniqueness, we need a different proof for the existence of (1.2) from the original proof (17), which is described in Theorem 5.2.

LEMMA 5.1. *Given smooth τ-periodic even timecourse* $a(t)$ *and odd timecourse* $b(t)$, *unique smooth functions p and q exist such that*[1]

$$q(\cos(2\pi t/\tau)) = a(t), \tag{5.1}$$

$$dp(\cos(2\pi t/\tau))/dt = b(t). \tag{5.2}$$

THEOREM 5.2. *Given smooth τ-periodic timecourses* $r(t)$ *and* $s(t)$, *unique smooth functions* f *and* g *of (1.2) exist* $dr/dt = 0 \Rightarrow d^2r/dt^2 \neq 0$.

Proof. Without loss of generality, let us assume that $r(t)$ has a maximum at t=0. A vertical shift and scaling of $r(t)$ can make its range [-1,1]. Then, by scaling time we can make $r(t') = \cos(2\pi t'/\tau)$. This scale is smooth because both dt/dt' and dt'/dt are well defined:

$$\frac{dt}{dt'} = \frac{dr/dt'}{dr/dt} = \frac{-(2\pi/\tau)sin(2\pi t'/\tau)}{dr/dt}. \tag{5.3}$$

---

[1] This follows from arguments presented in [3].

If $dr/dt = 0$, then $\sin(2\pi t'/\tau) = 0$ and $d^2r/dt^2 \neq 0$. Therefore, (5.3) is well defined by l'Hopital's rule. In the same way, dt'/dt is also well defined. Furthermore, $dt/dt' \neq 0$ and $dt'/dt \neq 0$ imply

$$dt/dt' > 0 \text{ and } dt'/dt > 0 . \tag{5.4}$$

Decomposition of $s(t')$ into its odd and even parts such that

$$s(t') = s(t')_{odd} + s(t')_{even} \tag{5.5}$$

allows the form

$$s(t') = dp(r(t'))/dt' + q(r(t')) \tag{5.6}$$

because we can find smooth functions q and p such that $s(t')_{even} = q(r(t'))$ and $s(t')_{odd} = dp(r(t'))/dt'$ by Lemma 5.1. Now by scaling back to the original time, we can get

$$s(t) = dp(r(t))/dt' + q(r(t)) \tag{5.7}$$

But we need $dr(t)/dt$ instead of $dr(t)/dt'$. For this, let us consider the ratio of $dr(t')/dt'$ and $(dr(t')/dt)_{odd}$.

$$\frac{dr/dt'}{(dr/dt)_{odd}} = \frac{2dr(t')/dt'}{dr(t')/dt - dr(-t')/dt} = \frac{2}{(dr(t')/dt)/(dr(t')/dt') - (dr(-t')/dt)/(dr(t')/dt')} .$$

Since $dr(t')/dt'$ is an odd function,

(5.8)
$$\frac{dr/dt'}{(dr/dt)_{odd}}=\frac{2}{dt'(t')/dt+dt'(-t')/dt}.$$

The denominator of (5.8) is never zero due to (5.4b). Therefore, (5.8) is well defined and smooth. Furthermore, (5.8) is an even function because it is the ratio of two odd functions. Therefore, with Lemma 5.1, we can find smooth function f_a such that

(5.9)
$$\frac{dr/dt'}{(dr/dt)_{odd}}=f_a(r).$$

We can also find a smooth function f_b such that

(5.10)
$$\frac{dr(t')}{dt}_{even}=f_b(r(t')),$$

(5.11)
$$\frac{dr}{dt'}=f_a(r)\frac{dr}{dt}_{odd}=f_a(r)(\frac{dr}{dt}-\frac{dr}{dt}_{even})=f_a(r)(\frac{dr}{dt}-f_b(r)).$$

From this,

(5.12)
$$\begin{aligned}s(t)&=\frac{dp(r(t))}{dt'}+q(r(t))=\frac{dp}{dr}\frac{dr}{dt'}+q(r)=\frac{dp}{dr}f_a(r)(\frac{dr}{dt}-f_b(r))+q(r)\\&=\frac{dp}{dr}f_a(r)\frac{dr}{dt}-\frac{dp}{dr}f_a(r)f_b(r)+q(r)=\frac{df(r)}{dr}\frac{dr}{dt}-g(r)=df(r)/dt-g(r)\end{aligned},$$

where $df(r)/dr=(dp/dr)f_a(r)$ and $g(r)=f_a(r)f_b(r)(dp/dr)-q(r)$.

Now, let us show the uniqueness of f and g. Let $s(t)=df_1(r)/dt-g_1(r)=df_2(r)/dt-g_2(r)$

$$\begin{aligned}&\frac{df_1}{dt}-g_1(r)=\frac{df_2}{dt}-g_2(r)\\&\frac{df_1}{dr}\frac{dr}{dt}-g_1(r)=\frac{df_2}{dr}\frac{dr}{dt}-g_2(r)\\&\frac{df_1}{dr}(\frac{dr}{dt'}\frac{1}{f_a(r)}+f_b(r))-g_1(r)=\frac{df_2}{dr}(\frac{dr}{dt'}\frac{1}{f_a(r)}+f_b(r))-g_2(r)\end{aligned}\quad . \tag{5.13}$$

Note that since (5.9) is nonzero, $1/f_a(r)$ is well defined. With the time scale t', $r(t')$ is an even function and $dr(t')/dt'$ is an odd function. Let us take the odd part of (5.13):

$$\frac{df_1}{dr}\frac{dr}{dt'}\frac{1}{f_a(r)}=\frac{df_2}{dr}\frac{dr}{dt'}\frac{1}{f_a(r)}\ . \tag{5.14}$$

Equation (5.14) implies $df_1/dt'=df_2/dt'$, which means $df_1/dt=df_2/dt$. Then, $g_1(r)=g_2(r)$ follows. □

Unfortunately, it is difficult to interpret the biological meaning of *f* and *g* of (1.2). Now, we propose a way to convert (1.2) into a more common form of the model so that *f* and *g* of (1.2) can be interpreted as production and degradation rates.

THEOREM 5.3. *Given smooth τ-periodic timecourses* $r(t)$ *and* $s(t)$, *smooth functions* f and g *of (1.3) exist uniquely if* $dr/dt=0\Rightarrow d^2r/dt^2\neq 0$, $ds/dt=0\Rightarrow d^2s/dt^2\neq 0$, *and*

$$\phi(t)=\hat{s}(\hat{r}(t))\neq t \text{ for all } t. \tag{5.15}$$

Proof. Let us show that dp/dr of (5.6) is well defined and not zero for all *t*. From (5.5) and (5.6),

$$s(t')=s(t')_{odd}+s(t')_{even}=dp(r(t'))/dt'+q(r(t'))=(dp/dr)(dr/dt')+q(r(t'))\ , \tag{5.16}$$

$$(5.17) \qquad \frac{dp}{dr} = \frac{s(t')_{odd}}{dr/dt'} = \frac{s(t')_{odd}}{(dr/dt)(dt/dt')}.$$

Since $dr/dt \neq 0$ except for extrema ($t' = 0$ and $-\tau/2$ on $[-\tau/2, \tau/2)$) and $dt/dt' \neq 0$ from (5.4), dp/dr is well defined for $t' \neq 0$ and $t' \neq -\tau/2$. If $s(t')_{odd}$ has zero except for $t' = 0$ and $t' = -\tau/2$, then $s(t') = s(t')_{even}$ *or* $\phi(t') = \hat{s}(\hat{r}(t')) = t$ because $r(t')$ is an even function, which contradicts (5.15). Therefore, $s(t')_{odd}$ is not zero except for $t' = 0$ and $t' = -\tau/2$ on $[-\tau/2, \tau/2)$. Therefore, $dp/dr \neq 0$ except for $t' = 0$ and $t' = -\tau/2$. Furthermore, for $t' = 0$ and $-\tau/2$,

$$(5.18) \quad \frac{dp}{dr}_{t'=0,-\tau/2} = \frac{s_{odd}(t')}{dr(t')/dt'} = \frac{(ds_{odd}(t')/dt')}{(dr^2(t')/dt'^2)} = \frac{(ds_{odd}(t')/dt')}{(dr^2(t')/dt^2)(dt/dt')^2} = \frac{(ds(t')/dt')}{(dr^2(t')/dt^2)(dt/dt')^2}$$

The second equality comes from l'Hopital's rule and the fourth equality comes from $ds_{even}(t')/dt' = 0$ at $t' = 0$ and $-\tau/2$. Since $dt/dt' \neq 0$ from (5.4) and $dr^2/dt^2 \neq 0$ at $t' = 0$ and $-\tau/2$, dp/dr is well defined. Furthermore, $ds(t')/dt' \neq 0$ at $t' = 0$ and $-\tau/2$ because $s(t')$ does not have an extremum at $t' = 0$ and $-\tau/2$ by (5.15). This implies that $dp/dr \neq 0$ at $t' = 0$ and $-\tau/2$. Therefore, dp/dr is well defined and nonzero for all t' or *t*.

From (5.8) and (5.9), $f_a(r)$ is well defined and not zero for all *t*. Therefore, (5.12) can be modified to

$$\begin{aligned} s(t) &= \frac{dp}{dr} f_a(r) \frac{dr}{dt} - \frac{dp}{dr} f_a(r) f_b(r) + q(r) = \frac{dp}{dr} f_a(r) \frac{dr}{dt} - h(r) \\ \frac{dr}{dt} &= f(r)s(t) - g(r) \end{aligned}$$

, where $f(r) = 1/(f_a(r)dp/dr)$ and $g(r) = -h(r)/(f_a(r)dp/dr)$. □

Note that (1.3) is a canonical type of model with a production rate and degradation rate. The difference between (1.3) and (1.1) is that the production rate depends on both $r(t)$ and $s(t)$.

2.6 Conclusion

Our results show how mathematical models could be constructed given two oscillating timecourses, $r(t)$ and $s(t)$ from a biochemical system. Models of the form (1.1) have perhaps the greatest biological intuition, but also lack existence and uniqueness. Models of form (1.2) can be broadly constructed, and are also unique, but their biological interpretation is limited. Models of form (1.3) contain properties in between models of forms (1.1) and (1.2). Interestingly, most results were obtained by studying the fixed points of an iterating map $\phi^n(t)$. Future work should study these iterative maps to more easily determine their fixed points. Additionally, our assumption about complete knowledge of the timecourse data is unrealistic. Given the noisy nature of all biological data, statistical methods should be incorporated with our methods to estimate f and g or rule them out. We hope our results will encourage consideration of well-posedness in the construction of models of biological timekeeping.

Chapter 3 A Mechanism for Robust Circadian Timekeeping and Chronic Pharmacological Manipulation of Circadian Rhythms

3.1 Introduction

Circadian rhythms are endogenous self-sustained oscillations with a period of about 24hrs that are seen in diverse physiological and metabolic processes, such as sleep/wake behavior, heart pressure, body temperature and hormone secretion (44). These rhythms are regulated by the circadian clocks, intrinsic time-tracking systems with which organisms can anticipate environmental changes and adapt to these changes such as daily rhythms of light and temperature (45, 46). With this intrinsic time measuring device, organisms can control their physiology in an active rather than a passive manner (46). For instance, for seasonal day length changes, animals change their sleep/wake cycles; flies change their hatching timing, and plants change their organ positions (47). The importance of circadian clocks for organizing the physiology of organisms can be seen from the profound influence of disrupted circadian clocks on health. The disrupted circadian rhythms of human involving irregular daily life, has been known to increase the risk of severe diseases, such as depression, insomnia, jet lag, coronary heart disease, neurodegenerative disorders, and cancer (24).

When circadian clocks were first discovered, three basic properties were identified (48). 1) Rhythms need to be autonomous. 2) Rhythms need to be capable of adjusting in response to external signals. 3) Rhythms need to persist over a wide range of temperatures. More recently, the biochemical mechanisms of circadian timekeeping have been identified (49). In particular, interlocked transcription-translation feedback loops (TTFLs) have been discovered as the basic mechanism of rhythm generation in many organisms (2). With this discovery, recent experimentation has identified another property of circadian rhythms in higher organisms. Circadian rhythms persist with a 24-hour period even in the presence of large changes in the expression of the components of these TTFLs (49, 50). While mechanisms for rhythm generation with a flexible period have been identified (3, 51, 52), mechanisms for this robustness of period to gene dosage remain unexplained, even by mathematical models (49, 50).

Two interlocked negative feedback loops have been identified in the TTFL networks generating circadian rhythms in higher organisms (Figure 3-1) (53-56). A "core" negative feedback loop consists of repressors (PERIOD and TIMELESS in *Drosophila* or PERIOD1-3 and CRYPTOCHROME1-2 in mammals), which *inactivate* activators (CYCLE and CLOCK in *Drosophila* and BMAL1-2 and CLOCK in mammals) of their own transcription. An additional negative feedback loop controls the expression of the activators, which *inactivate* their own transcription through *Vrille* (*Drosophila)* or the *Rev-erbs* genes (Mammals) (53, 57). While other feedback loops have also been identified, these two negative feedback loops seem to predominate for the regulation of circadian rhythms (53-56, 58, 59).

Near 24-hour oscillations persist even when the components of the TTFLs of the circadian clock are over or under expressed. Heterozygous mutations of clock genes never abolish rhythmicity, and their period phenotypes are either indistinguishable from the wild-type phenotypes or are much smaller than mutations that affect post-translational modifications (18, 60, 61). Abolishing rhythmicity through single gene knockout is surprisingly difficult (18, 23). Moreover, the mammalian circadian clock is also resistant to global changes in transcription rates (50). These results all suggest that gene dosage may not be important for circadian timekeeping in higher organisms.

Gene dosage, however, is not *completely* unimportant for timekeeping. Knockdown of clock genes causes increased expression in similar components (paralog compensation), which may help restore gene dosage and indicates that gene dosage needs to be tightly regulated (18). Population rhythmicity in mouse embryonic fibroblasts shows much lower amplitude than in liver (62). The ratio of repressors to activators is significantly lower in fibroblasts than that found in liver (62, 63). A 1-1 stoichiometric binding occurs between the activators and repressors driving rhythms in *Drosophila* (64), although not in *Neurospora* (65, 66).

In this chapter, we propose a mechanistic explanation for the robustness to gene dosage in the circadian clock of higher organisms through mathematical modeling. We develop the most detailed mathematical model of the mammalian circadian clock available, which should be useful in many future studies. Our model reproduces a surprising amount of experimental data on the mammalian circadian clock including the time courses and relative concentrations of key transcripts and proteins, the effects of mutations of key clock genes, and the effects of changes in gene dosage. With this model, we show that proper stoichiometric balance between activators (BMAL-CLOCK/NPAS2) and repressors (PER1-2/CRY1-2) is key to sustained oscillations. Furthermore, we find that an additional slow negative feedback loop, in which activators indirectly *inactivate* themselves, improves the regulation of the stoichiometric balance and sustains oscillations with a nearly constant period over a large change in gene expression level. Tight binding between activators and repressors is also predicted to be crucial for rhythm generation. These mechanisms are also validated by mathematical analysis of a simplified mathematical model of the mammalian circadian clock, and simulations of a previously published *Drosophila* model. We here propose a novel design for biological oscillators where maintaining period is crucial: a core negative feedback loop with repression by protein sequestration, with an additional negative feedback loop, which controls a relatively stable activator.

Interestingly, circadian clocks also have flexibility regarding phase entrainment. That is, this endogenous timekeeping system can be synchronized to the earth's 24-hour periodic environment through external cues, known as *zeitgebers* (e.g. light/dark (LD) cycle and temperature cycle) (48, 67). To maintain clock-environment synchrony, *zeitgebers* induce changes in the concentrations of the molecular components of the clock to levels consistent with the appropriate stage in the 24-hour cycle. Misalignments of circadian timing with the external environment can cause significant physiological problems, such as jet lag, depression, insomnia, coronary heart disease, neurodegenerative disorders, and cancer (24). In particular, mood disorders and bipolar disorders appear to be tightly related to disrupted circadian rhythms (68-71). To treat the misalignment of circadian clocks with the external environment, pharmacological manipulation of circadian clocks has received much attention (72-75). Previous studies have shown that acute dosing of PF-670462 (CK1δ/ε inhibitor) can delay circadian behavior, as well as reestablish a circadian rhythm in *Vipr2-/-* mice that are arrhythmic under dark-dark (DD) cycle or light-light (LL) cycle (76-78). To extend this work to real life situations that proceed under LD cycles with seasonal variation, we need to study the effect of CK1δ/ε inhibition on circadian rhythms under different LD cycles.

In this chapter, we study how light stimuli and CK1δ/ε inhibition affect mammalian circadian timekeeping with a combination of experiments and simulations using a mathematical model of intracellular mammalian circadian clocks (79). We find that the opposing actions of pharmacological delay and light can yield a constant stable delay of circadian behavior when CK1δ/ε is inhibited chronically under LD cycles. The occurrence and magnitude of a stable phase delay depends on the dosing amount, dosing timing, intrinsic period and day lengths. This work provides a way to determine a dosing strategy of chronic CK1δ/ε inhibition to treat the misalignment of circadian clocks by modulating the phase of circadian rhythms.

3.2 Mathematical modeling of the mammalian circadian clock

3.2.1 Description of the detailed model of mammalian circadian clock

We developed a new mathematical model of the intracellular mammalian circadian clock. This model contains key genes, mRNAs and proteins (PER1, PER2, CRY1, CRY2, BMAL1/2, NPAS2, CLOCK, CKIε/δ, GSK3β, Rev-erbα/β) that have been found to be central to mammalian circadian timekeeping (Figure 3-1A). While greatly expanded, the model is largely based on our previous model, which has made surprising predictions about mammalian timekeeping that have been subsequently verified experimentally (8, 23, 28, 80). The modification and extension of the detailed model from the original model (28) are listed.

(1) *Detailed modeling of additional feedback loops*: The new model includes secondary feedback loops, which regulate the transcription of genes with a RORE in their promoters, including *Bmals* (*Bmal1* and *Bmal2*) and *Npas2*. The RORE is repressed by binding of REV-ERBs (REV-ERBα and REV-ERBβ) (55, 57). Binding to the RORE is modeled with the same formalism used for E-box binding in the original model. While Bmals and Npas2 mRNA are produced proportional to the activity of RORE, Clock mRNA is assumed to be produced at a constant rate, matching experimental data (44). After transcription, Bmals, Clock and Npas2 mRNA are exported to the cytoplasm and then translated. BMALs can bind with CLOCK or NPAS2, which promote phosphorylation of the complex. The phosphorylated dimer can enter the nucleus, activate transcription of promoters with an E-box and is less stable than the unphosphorylated dimer (81).

(2) *Updated mechanisms of BMALs-CLOCK/NPAS2 repression*: Matching recent findings, we updated the mechanisms by which the repressors (PER/CRY) inhibit the activators (BMALs-CLOCK/NPAS2) (82-85). CRY1, 2 bind with BMALs-CLOCK/NPAS2 and make the dimer transcriptionally inactive as in the original model. Furthermore, CRY1, 2 binding stabilize the dimer (82, 83, 85). With higher affinity, PER1, 2 also bind with BMALs-CLOCK/NPAS2 and interfere with the binding of the dimer with E-box (84, 85).

(3) *Accounting for the heterogeneity of different genes with E-boxes*: The *Per1/2*, *Cry1/2*, and *Rev-erbs* genes have E-boxes on their promoters and their transcription occurs proportional to the activity of the E-box. Experimental studies found that the behavior of E-boxes on these genes is different. For example, when the activators (BMAL1-CLOCK) are overexpressed, expression of *Per*1, 2/*Cry*1, 2 shows little change while that of *Rev-erbs* significantly increases (62), which implies that the activators are saturated on the E-

boxes of *Per/Cry* genes, but not *Rev-erbs*. Furthermore, the time profile of Cry2 in SCN is almost flat unlike the other mRNAs (44). Therefore, we introduced the three different types of E-boxes for *Per1/Per2/Cry1*, *Cry2* and *Rev-erbs*.

(4) *Inclusion of the kinase GSK3β*: The new model includes another important kinase GSK3β for post-translational modification of the circadian clock as well as CKIε/δ. GSK3β phosphorylates PER2 and promotes its binding with CRY and nucleus translocation (63, 86-88). GSK3β also phosphorylates the REV-ERBs and stabilizes them (89). Because GSK3β is expressed constitutively, we assume that its concentration is constant in our model (88). Although the GSK3β concentration is constant, its activity shows a circadian rhythm with a peak around ZT12 matching data from SCN (88). For this reason, we modeled the activity of GSK3β with a phase similar to Cry1 mRNA because the Cry1 mRNA time profile has a peak around ZT12. We allow CKIε/δ and GSK3β to enter the nucleus only when they bind with their substrates (63).

(5) *Precise description of the effect of light on the circadian clocks*: We included a previous model of the effect of light on the circadian clocks (90), which quantified the human circadian pacemaker response to the light successfully. In this model, the light increases on the transcription rate of Per1-2 decreases as more light is presented. This matches experiment data (91). In addition, we include a higher increase in Per2 transcription by light than the increase in Per1 transcription to match experimental data (92). That is, the amplitude of *per1* and *per2* gene expression are higher about 16% and 30%, respectively, under 12:12 LD cycle with 100 lux than 12:12 DD cycle. Because light is known to increase the transcription rate of Per1/2 regardless of the E-box state (93, 94), we assumed that the light effect was independent of the E-box state as occurred in the original Forger and Peskin model.

(6) *Processes not explicitly modeled*: First, we do not distinguish between BMAL1 and BMAL2, REV-ERBα and REV-ERBβ, CKIε and CKIδ, or CLOCK and NPAS2 because specific functional differences between these proteins or homologs have not been found. Second, we do not model the D-box, which is one of the clock-controlled elements (44).

Third, we removed the Rorc from the model because the existence of the Rorc did not change the model behavior due to its constant mRNA level (55). Fourth, we did not model the dimerization of the REV-ERBs. Finally, we did not model the phosphorylation of GSK3β on the CRY2 and BMAL1, which affects their degradation rate because the modest change of the amount of those proteins did not affect the model's behavior (95, 96).

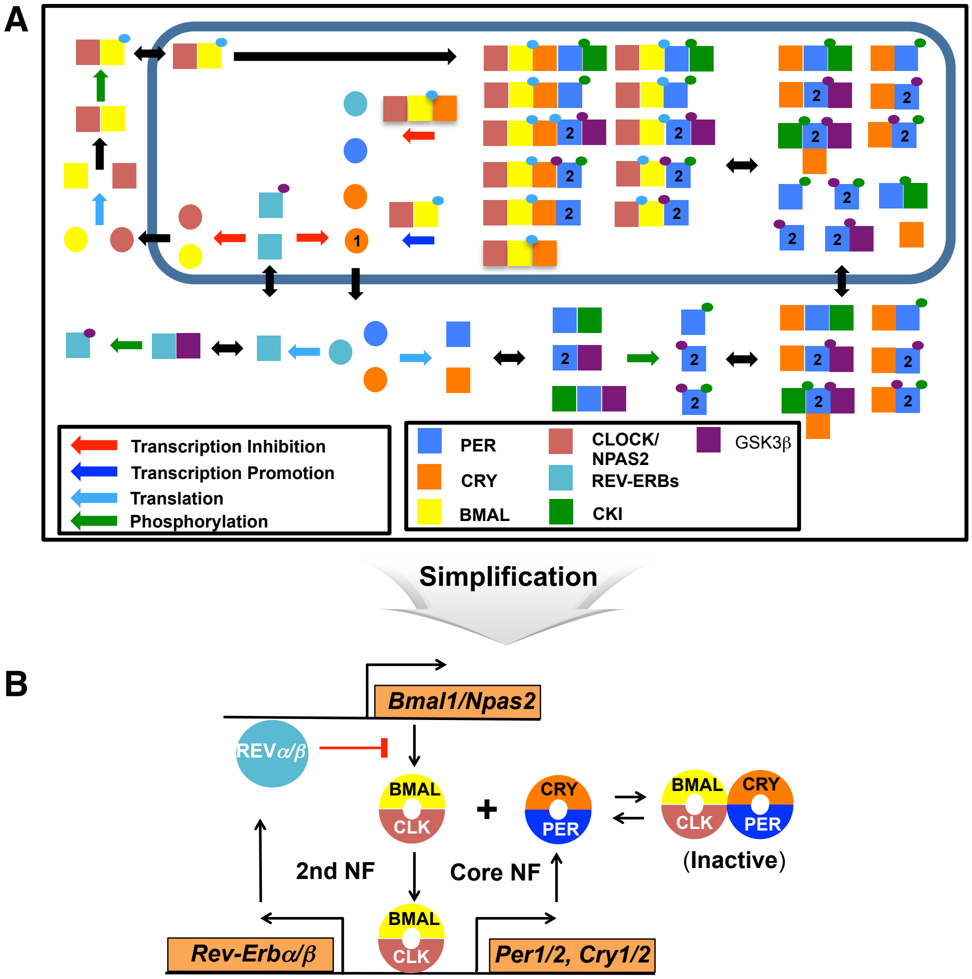

Figure 3-1. Schematic of the detailed mammalian circadian clock model.
(A) Only some of the relevant species are shown. Circles refer to transcripts and squares are proteins, possibly in complex. Small circles refer to phosphorylation states that are color coded by the kinases that perform the phosphorylation. (B) The detailed model consists of a core negative feedback loop and an additional negative feedback loop (the NNF structure). The repressors (PER1-2 and CRY1-2) inactivate the activators (BMALs and CLOCK/NPAS2) of their own transcription expression through the core negative feedback loop. The activators inactivate their own transcription expression by inducing the Rev-erbs through the secondary negative feedback loop.

3.2.2 Variables and equations of the detailed model

The monomer proteins considered in our model are PER1/2, CRY1/2, BMALs, CLOCK/NPAS2, REV-ERBs, CKI, and GSK3β. Although only 10 monomers are considered in the model, they can produce many complexes depending on the state of binding, phosphorylation and subcellular locations. To describe these all complexes, 181 variables are needed (Table A-1 and Table A-2): 159 variables are for protein complexes, 12 variables are for mRNAs, 8 variables are indicator of the promoter activity, and 2 variables are for light effect and GSK3β activity. The model variables are listed in Table A-1 and Table A-2. To simply describe the approximately two hundred complexes included in our model, which can result from bindings of PER1/2, CRY1/2, BMALs-CLOCK/NPAS2, and kinase, we use the following shorthand x[j][k][l][m][n] (23) (Table A-2). The variable j, k, l and n represents the binding state of PER, CRY, kinase, and phosphorylated BMALs-CLOCK/NPAS2, respectively. The variable m represents the subcellular location. For example, x[4][0][0][0][0] represents phosphorylated PER2 by CKI in the cytoplasm. x[3][1][1][1][1] represents the PER2-CRY1-CKI-BMALs-CLOCK/NPAS2^P complex in the nucleus, where ^{P} indicates phosphorylation. Some of these variables do not exist in our model due to the restrictions of the reaction. For instance, x[0][1][1][0][0] does not exist, because CRY binding with CK1 is not allowed if PER1 or PER2 are not bound in our model. In this case, the variable's concentration is always zero. The reactions between these variables are described by ODE systems using explicit mass kinetics as in the original model (28). The model equations are provided in the Appendix A.

3.2.3 Parameter estimation of the detailed model

While the original Forger-Peskin model used 36 parameters, the new model has the 75 parameters due to the extensions and modifications of the model. Despite the increased number of parameters, we could get tighter restriction on the range of parameters with newly published data (listed below). Over these ranges, parameters are estimated by fitting to more various types of data: timecourses of gene expressions and proteins, abundance of proteins, and mutation phenotypes.

(1) We choose 14 parameters (degradation rate of mRNAs and proteins) matching published experimental data. These parameter values were allowed to vary up to 50% from the experimentally determined values to account for experimental error and cellular heterogeneity (see Table A-3)
(2) PER1's phosphorylation rate is set lower than that of PER2 (63). Light induced-Per1 transcription is set lower than light induced-Per2 transcription (92).
(3) The dissociation constant between BMALs-CLOCK and CRY is set greater than that between BMALs-CLOCK and PER (84).
(4) The ratio between cytoplasm and nucleus volume are limited to between 1 and 3.5 (97).
(5) The other parameters are also restricted into a biologically reasonable range (see Table A-3).

Within these restrictions, a simulated annealing method (SA, a global stochastic parameter searcher) (98) was used to estimate the parameters in two steps. First, we found parameters that provides a good fit with mRNA and protein time profiles measured in mouse suprachiasmatic nuclei (SCN) (44, 99) and relative abundance of clock proteins measured in mouse liver (63) and fibroblast (61, 62) (Figure 3-2). In this fitting, we used a similar cost function to that used in estimating the parameters of the original model (Forger & Peskin, 2003).

$$\sqrt{\sum_{j=1}^{10}\sum_{i=1}^{n_j} w_{ij}\frac{(s_{ij}-e_{ij})^2}{n_j}+\sum_k (pm_k-p_k)^2}$$

Here, j runs through 6 mRNAs and 4 proteins. n_j is the number of data points (12 for mRNA and 13 for protein). s_{ij} and e_{ij} are simulated timecourses and experimentally measured timecourses, respectively. s_{ij} are normalized, matching experimental data (see

Figure 3-2). $w_{ij} = 5$ when $e_{ij} = 1$ and $w_{ij} = 1$ otherwise, so that the cost function has more weight at the peak time than other times. pm_k and p_k are maximum value of protein abundance, respectively. pm_k and p_k are normalized, so that the maximum abundance of the CRY1 protein is 1.

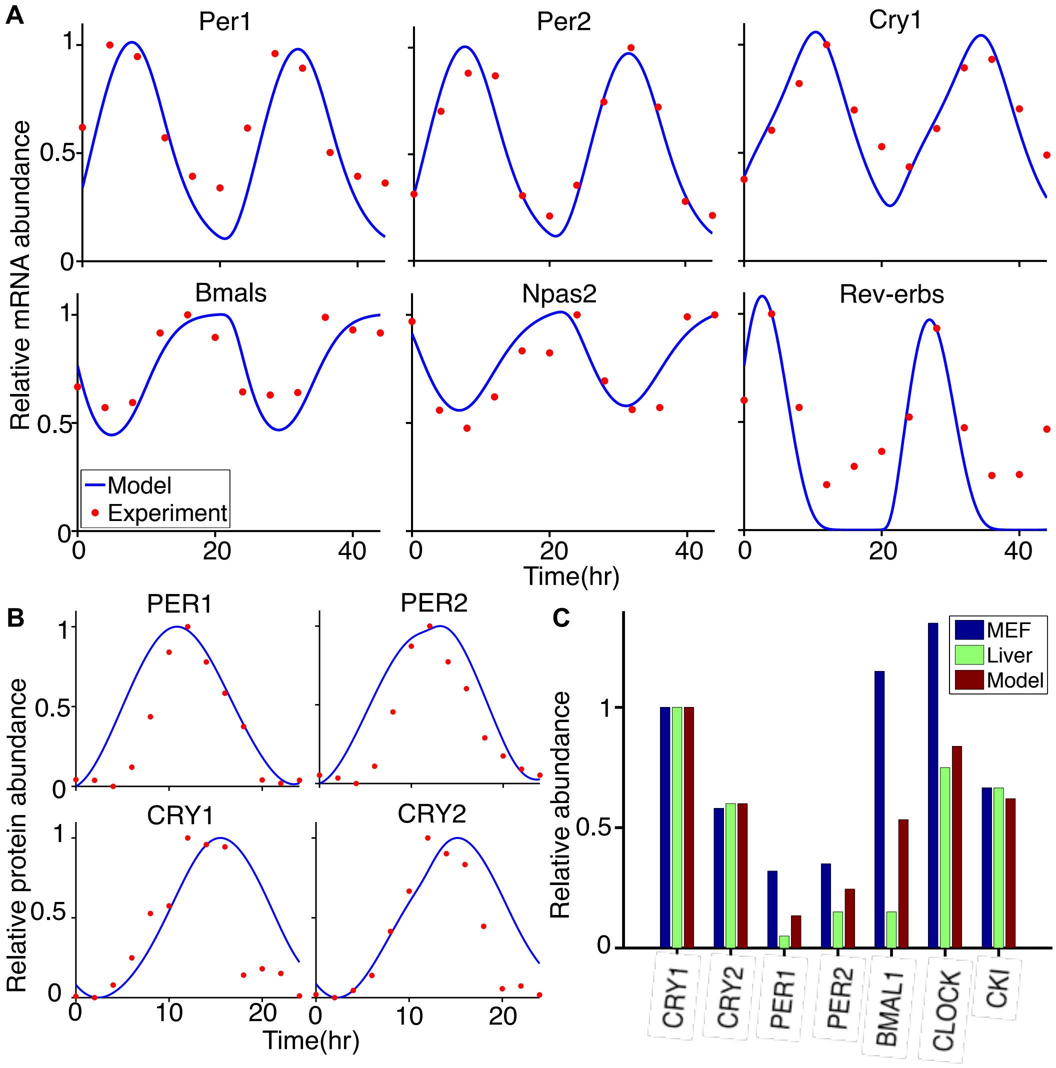

Figure 3-2. Validation of the detailed model.
(A) Predicted mRNAs timecourses in SCN (44). Timecourses were normalized so that the peak value is 1, matching experimental data. (B) Predicted protein timecourses in SCN (99). As had been done previously, we normalize the protein timecourses so that the maximum is 1 and the minimum is 0. (C) Model comparison of the relative abundance of proteins in liver and fibroblast (61-63). All of the values were normalized so that the maximum abundance of the CRY1 protein is 1. For the CKIε/δ, CKIε maximal expression is approximately 22.5% of the maximum abundance of CRY1 in the liver (63) and CKIδ is two times more abundant than CKIε in the fibroblast (61). From this, we assumed that total CKIε/δ would be approximately 66.5% of the maximum value of CRY1 in mice liver and fibroblast.

Table 3-1. Comparison of model predictions with experimental data and previous model predictions on the phenotypes of circadian mutations

Mutated Gene	SCN	Animal	New Model	Relogio (2011)	Mirsky (2009)	Leloup (2003)	Forger (2003)
Cry1$^{-/-}$	Short	Short	-1	Long	AR	Short	WT
Cry2$^{-/-}$	Long	Long	+1.6	Long	Long	Short	Long
Per1$^{-/-}$			WT	AR	AR	Short	Long
Per1$^{\mathrm{ldc}}$	WT	Short/AR					
Per2$^{-/-}$			AR	AR	AR	Short	Short
Per2$^{\mathrm{ldc}}$		Short/AR					
Bmal1$^{-/-}$	SR		AR	AR	AR	AR	AR
Bmal1$^{-/+}$	WT*		+0.1	AR	Na	AR	Long
Clock$^{-/-}$	WT	Short	-0.2	Long	AR	AR	AR
Clock$^{\Delta 19/\Delta 19}$	AR*	Long	AR	Long	Na	na	na
Clock$^{\Delta 19/+}$	Long*		+1.1	Long	Na	na	na
Npas2$^{-/-}$	WT	Short	WT	na	Na	na	na
Rev-erbα$^{-/-}$		Short	-0.2	AR	Short	na	WT
CK1ε$^{tau/tau}$	Short	Short	-3	na	Na	Short	Short

Here we indicate whether the phenotype predicted by our model, or seen in experimental data is wild-type (WT), stochastically rhythmic (SR), arrhythmic (AR) or shows a change in period in hours. Experimental data can be found in (18) as well as references cited therein, except those marked with * which can be found in (100) and ** which can be found in (23). Red represents different phenotype prediction from the new model. na represents not available. For the Leloup-Goldbeter model, first parameter set of the model is used.

After the first round of SA, we found several parameter sets qualitatively matching with experimental data on phenotypes of mutations of mice (WT, short, long and AR) (Table 3-1). Then we used these parameter sets as initial parameter sets for another round of SA to get the final parameter set, which shows a quantitatively good fit with knockout mutation phenotype as well as time profiles (Table A-3). The cost function used for the second round is followed.

$$\sqrt{\sum_{j=1}^{10}\sum_{i=1}^{n_j} w_{ij}\frac{(s_{ij}-e_{ij})^2}{n_j}+\sum_k (pm_k-p_k)^2}+\sqrt{\sum_l (mp_l/m_l-1)^2+\sum_n (ma_n)^2}$$

mp_l and m_l are simulated period and experimentally measured period of rhythmic phenotypes of mutations, respectively. ma_n are simulated relative amplitude of arrhythmic phenotypes of mutation (e.g. Per2$^{-/-}$ or Bmal1$^{-/-}$).

3.2.4 Accurate prediction of various mutation phenotypes.

With the estimated parameters, our model accurately predicts the phenotype of known mutations of genes in the central circadian clock (SCN) (18, 23, 100), which other models do not predict (see Table 3-1) (28, 29, 101, 102). Interestingly, our model shows opposite phenotypes for *Cry1*$^{-/-}$ and *Cry2*$^{-/-}$ matching experimental data (103). There are two differences between CRY1 and CRY2 in our model. First, *Cry1* transcription is delayed through repression by Rev-erbα and Rev-erbβ (55, 57, 104). Additionally, *Cry1* mRNA is more stable than *Cry2* mRNA and CRY1 protein is more stable than CRY2 protein (84, 105, 106). Since a longer half-life causes rhythms to be delayed, and delayed rhythms cause a longer period (17, 104), removing CRY1 shortens the period and removing CRY2 lengthens the period. The opposite phenotypes of *Clock*$^{-/-}$ (null mutation) and *Clock*$^{\Delta 19/+}$ (dominant negative mutation) are also correctly simulated in the model for the first time (107-109). Moreover, our model also predicts the mutant phenotypes of isolated SCN neurons, which are different from the SCN slices (103). We note that SCN slices have significantly higher gene expression of *per1* and *per2* through CREB/CRE pathway than isolated SCN neurons (110). Interestingly, when we reduced *per1* and *per2* expression about 60% in our model, our model was able to accurately reproduce the phenotypes of isolated SCN neurons (Table 3-2).

Table 3-2. Comparison of modified model predictions with experimental data of single SCN neurons on the phenotypes of circadian mutations

Gene	dSCN	Model
Cry1$^{-/-}$	AR	AR
Cry2$^{-/-}$	Long	+2.3
Per1$^{-/-}$		AR
Per1$^{\mathrm{ldc}}$	AR	
Bmal1$^{-/-}$	AR*	AR

Here we indicate whether the phenotype predicted by our model, or seen in experimental data is arrhythmic (AR) or shows a change in period in hours. Experimental data can be found in (103), except those marked with * which can be found in (23).

3.3 A mechanism for robust circadian timekeeping

3.3.1 Proper stoichiometric balance between activators and repressors is crucial to sustained rhythms

Since our mathematical model can accurately predict the phenotype of known mutations of the mammalian circadian clock, we next looked for a mechanism that could explain why some phenotypes were rhythmic, while others were not. We found that stoichiometry plays a key role in determining which mutations showed rhythmic phenotypes. Here we define stoichiometry as the average ratio between the concentrations of repressors (all forms of PER and CRY in the nucleus) to that of activators (all forms of BMAL-CLOCK/NPAS2 in the nucleus) over a period. Moreover, we specifically refer to repressors and activators of E/E'-boxes when discussing stoichiometry. We found that mutations that caused the stoichiometry to be too high or too low, yielded arrhythmic phenotypes (Figure 3-3A). So long as the mutations allowed the stoichiometry to be around a 1-1 ratio, relatively high amplitude oscillations were seen. Thus, we predict that stoichiometry provides a unifying principle to determine the rhythmicity of mutations of the mammalian circadian clock. To further test this principle, we constitutively expressed either the Per2 gene (the dominant repressor gene) or the Bmal and Clock genes (the dominant activator genes) at different levels. Interestingly, within a range centered near a 1-1 stoichiometry, the model shows sustained oscillations with high amplitude (Figure 3-3B). However, if the stoichiometry was too high or too low, rhythms are dampened or completely absent (Figure 3-3B). This matches a recent experimental study showing that the amplitude and sustainability of population rhythms increase when the level of PER-CRY is increased closer to that of BMAL1-CLOCK in mouse fibroblasts (62).

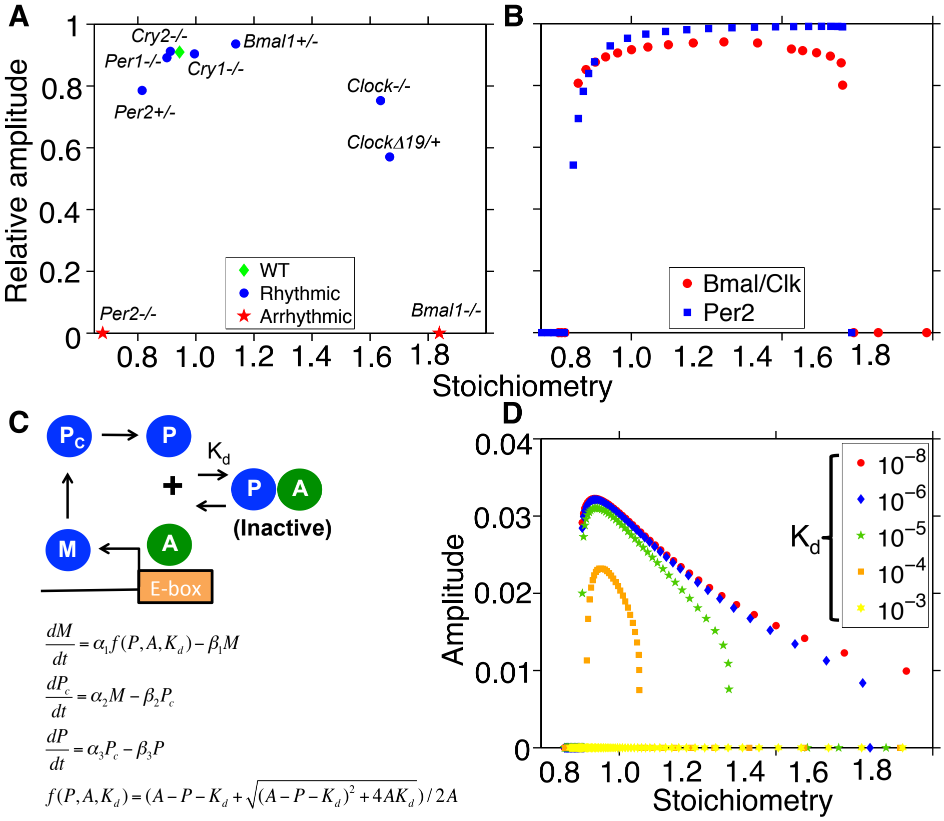

Figure 3-3. Proper stoichiometry between activators and repressors is the key to sustained oscillations.

(A) Our detailed mathematical model accurately predicts the phenotype of the known mutations in circadian genes (Table 3-1). We plot the stoichiometry predicted by our model in these mutants with the relative amplitude of Per1 mRNA rhythms (or Per2 mRNA when considering the *Per1*$^{-/-}$). These results indicate that the phenotype of the mutants can be predicted by their effects on stoichiometry. (B) The stoichiometry between repressors and activators is changed by constitutively expressing either the Per2 gene or the Bmals and Clock genes at different levels. Note that the model is rhythmic only when the stoichiometry is near 1-1. (C) Schematic of a simplified model based on the Goodwin oscillator. Instead of a Hill-type equation, the sequestration of the activator (A) by the repressor (P) is used to describe repression of the gene. (D) Oscillations are seen around a 1-1 stoichiometry as the level of activator is changed. The range of the stoichiometry widens as the dissociation constant (K_d) decreases or the binding between the activator and the repressor tightens.

We defined the stoichiometry as the average ratio between the total concentrations of repressors to that of activators over a period. However, recent work has shown that CRY1 has stronger repressor activity than CRY2. The underlying biochemical mechanisms for this result have not been fully identified (111). If the difference is due to a different post-translational mechanism (e.g. binding between PER and CRY, which could affect the repressor concentration in the nucleus), the current definition of stoichiometry can be kept. Otherwise, a more sophisticated definition of stoichiometry may be needed (e.g. one that gives more weight to concentration of CRY1 than that of CRY2).

3.3.2 How stoichiometry generates rhythms

To test the role of stoichiometry in sustaining oscillations, we developed a simple model by modifying the well-studied Goodwin model (30) to include an activator (A), which becomes inactive when bound by a repressor (P) (Figure 3-3C). Transcription is proportional to the fraction of free activator that is not bound by the repressor, f (P, A, K_d) (112), matching experimental data from the mammalian circadian clock (Figure 3-4) (113). mRNA (M) is translated to a repressor protein (P_c). The protein enters the nucleus (P) and binds and inhibits the activator (A). This generates a single negative feedback loop (SNF) since the activator is constitutively expressed. The model is similar to a previously published mathematical model (114); however, we allow for both association and dissociation of the activator and repressor (through a defined K_d), which turns out to be crucial for understanding the effects of stoichiometry. By nondimensionalization and setting the clearance rates of all species to be equal (to increase the chance of oscillations, see (17)), only two parameters remain: the activator concentration (A) and the dissociation constant (K_d) (See Appendix B).

When we changed the activator concentration, which changed the stoichiometry (average ratio between the level of repressor (P) to the level of activator (A)), sustained oscillations were only seen at around a 1-1 stoichiometry similar to our detailed model (Figure 3-3D). As the other parameter (K_d) decreased (indicating tight binding), the range of stoichiometry that permitted oscillation increased (Figure 3-3D). Interestingly, if the binding was too weak, the rhythms did not occur. The tight binding between activators and repressors is also found in the detailed model, and in the mammalian circadian clock (63, 113, 115). This indicates that the sustained rhythms require tight binding as well as balanced stoichiometry in the circadian clock.

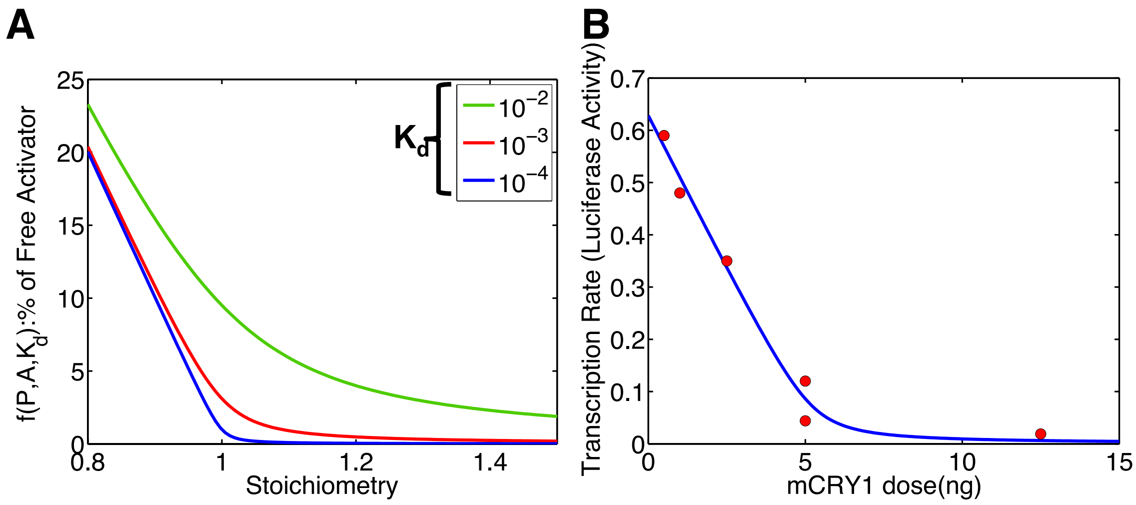

Figure 3-4. The transcription rate control by protein sequestration of the simple model matches experimental data.
(A) The fraction of the free activator, *f*(P, A, K$_d$), with various dissociation constants, K$_d$. As dissociation constant between the activator (A) and the repressor (P) decreases, the fraction of free activator decreases or transcription rate decreases. Here, A=0.0659. (B) The effects of mCRY1 expression on CLOCK:BMAL1 activated transcription. Data are taken from Figure 2 and Supplementary Figure 2 of (113). Our model can easily match this data.

Many previous studies have argued that ultrasensitive responses (e.g. a large change in transcription rate for a small change in repressor or activator concentration) can cause oscillations in feedback loops (2, 17, 116, 117). A previous study showed that an ultrasensitive response can be generated by tight binding of activators and repressors in a synthetic system (112). Taken together, this provides a potential mechanism of rhythm generation. That is, when the total concentration of repressor is higher than that of activators, the repressor sequesters and buffers activator and inhibits transcription completely (117). As the repressor is depleted, the excess free activators are no longer sequestered by repressors and are free to turn on the transcription. At this threshold, transcription of repressor shows an ultrasensitive response to the concentration of repressor or activator. Ultrasensitive responses amplify rhythms and prevent rhythms from dampening (17). In both our simple and our detailed model, we found ultrasensitive responses around a 1-1 stoichiometry (Figure 3-5A). When the stoichiometry was not around 1-1, an ultrasensitive response was not seen, and both models did not show sustained rhythms.

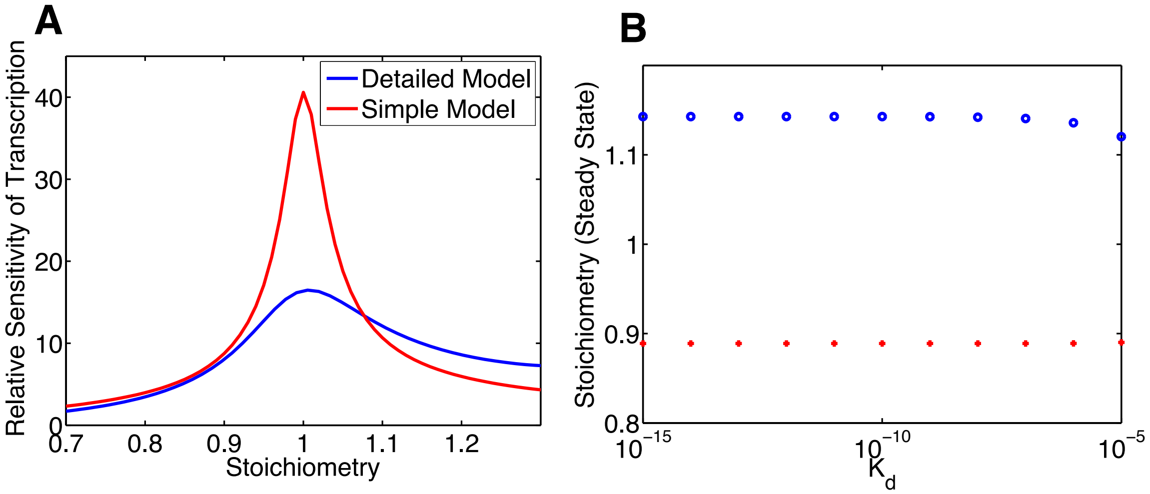

Figure 3-5. 1-1 stoichiometry generates an ultrasensitive response.
(A) The relative sensitivity of transcription rate of repressors is the highest at 1-1 stoichiometry in both the detailed and the simple model. From the solutions of model, we calculated

$$\mathrm{Re}\mathit{lative\ Sensitivity} = \frac{d(\%\ \mathit{of\ Free\ Activators})}{d(\mathit{Stoichiometry})}\frac{\mathit{Stoichiometry}}{\%\ \mathit{of\ Free\ Activators}}$$

(See Figure 3-6B for the parameters used). (B) The upper and lower bound of steady state of stoichiometry where the simple model oscillates. See Appendix B for details.

Over the course of a day, as levels of repressor and activator change, the stoichiometry and also sensitivity change as well. We found that the 1-1 average stoichiometry is required to generate the ultrasensitive response which causes rhythms through mathematical analysis, confirming our simulation results (Figure 3-3D). That is, via both local and global stability analysis, we derived an approximate range of the stoichiometries (<S>) that permit oscillations

$$\frac{8}{9} < \langle S \rangle < \frac{2}{7\sqrt{7\sqrt{K_d / 2}}}$$

(See Appendix B). In agreement with our simulations shown in Figure 3-3D, this mathematical analysis also suggests that: 1) Oscillations are seen around a 1-1 stoichiometry; 2) the stoichiometry needs to be greater than 8/9 for sustained rhythmicity; 3) as the binding between activators and repressors becomes tighter, the upper bound on stoichiometry increases; 4) if the binding is too weak (e.g. $K_d=10^{-3}$), sustained oscillations do not occur.

3.3.3 An additional negative feedback loop improves the regulation of stoichiometric balance

If stoichiometry is key to sustained oscillation, are there mechanisms within circadian clocks that keep the stoichiometry of components balanced? Does the additional negative feedback loop of the NNF structure, found in circadian clocks, help balance stoichiometry? To test this structure, we added an additional negative feedback loop into our simple model (Figure 3-6A). Previously, other studies suggested that an additional positive, rather than negative, feedback loop could sustain intracellular clocks (3, 51, 52, 118). We tested these structures by including an additional protein R (Rev-ERBs or RORs in the mammalian circadian clocks) that is transcribed in a similar way to P. R then represses (as in the Rev-erbs) or promotes (as in the Rors) the production of A in the negative-negative feedback loop (NNF) or the positive-negative feedback loop (PNF) structure, respectively (Figure 3-6A).

We studied how the SNF, NNF, and PNF structures effectively maintain the stoichiometric balance when model parameters (e.g. transcription rate) are changed. With both simulation and steady state analysis, we found that the NNF structure is best at keeping stoichiometry balanced while the PNF structure is worst at keeping stoichiometry balanced, regardless which parameters are perturbed (see Appendix B, and Figure 3-6B-C). Moreover, our detailed model, which also follows the NNF structure, also carefully balanced the stoichiometry by controlling the expression of repressors and activators. Knockdown of the repressor *Cry1* leads to higher expression of the repressors, which are controlled by E-boxes, and lower expression of the activators, which are controlled by a ROREs (Figure 3-7A). Opposite effects are seen when the activator CLOCK is removed (Figure 3-7A). This active control of repressors and/or activators via the NNF structure regulates the stoichiometric balance tightly (Figure 3-7B) and matches experimental data on gene dosage (18). Moreover, the detailed model (with the NNF structure) also correctly predicts the change of clock gene expression after the removal of the additional negative feedback loop (*Rev-erbα,β-/-*) (Figure 3-7C) (55, 58, 59). In particular, knockout of the *Rev-erbα,β* decreases PER expression, but increase CRY1 expression. For our nominal set of parameters, oscillations are still possible when this additional negative feedback is removed. However, for other sets of parameters, where stoichiometry is not as well balanced, removal of this additional negative feedback stops rhythmicity (See below). This could explain the phenotype of the *Rev-erbα,β-/-*, which show some indications of rhythmicity. Our model predicts that rhythm generation remains in cell types that have a near balanced stoichiometry, and a lack of rhythms in cell types without a balanced stoichiometry.

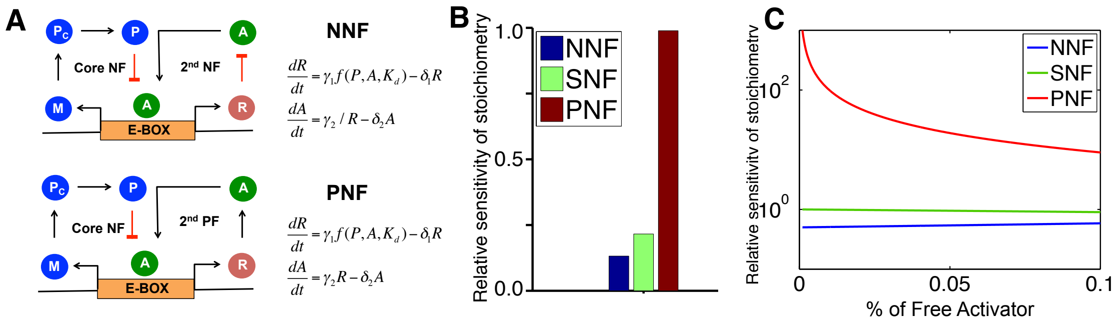

Figure 3-6. The NNF structure maintains stoichiometry in balance by active compensation of both repressors and activators.
(A) A negative or positive feedback controlling the activator is added to the original negative feedback controlling the repressor. (B) The relative sensitivity (% change in mean level of stoichiometry per % change in transcription rate of repressor) in the simple models with SNF, NNF, and PNF structure were measured over a range of the transcription rates of repressor Then, we calculated the average of relative sensitivity over the range of parameters. On average, the relative sensitivity of the NNF model is about 2 fold less sensitive that of the SNF model, but that of the PNF model is about 4 fold more sensitive than that of the SNF model. (Here we assumed δ=0.2. When this assumption was relaxed, the result is similar. See Appendix B and Figure 3-6C). (C) Relative sensitivity of the steady state of % of free activator for the general parameters of the simple models with different structures (see Appendix B for the details).

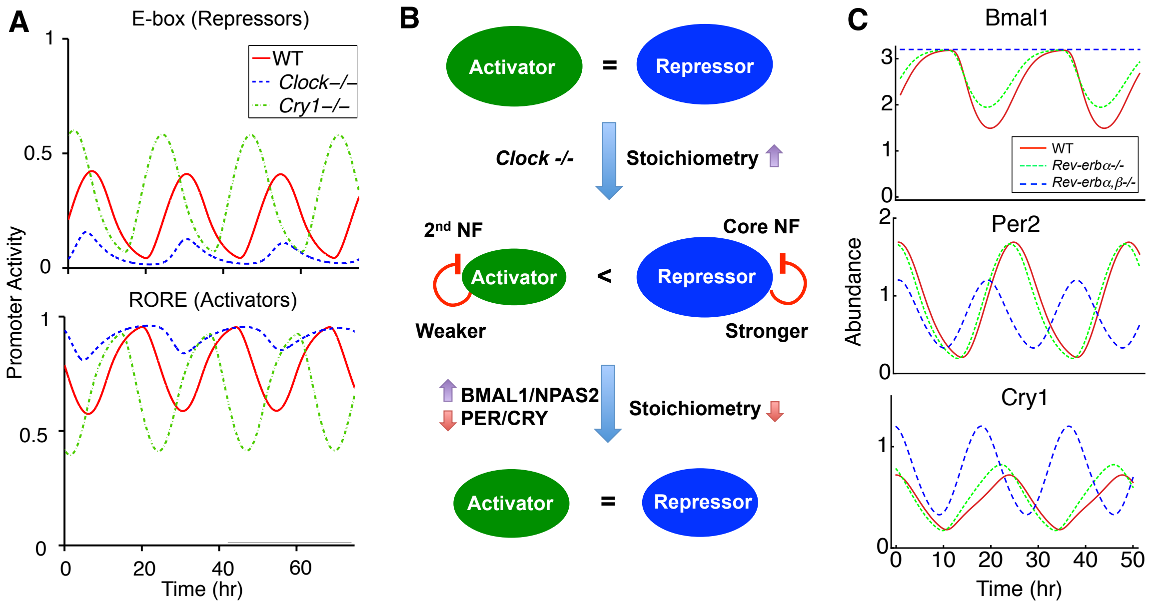

Figure 3-7 The explanation of how the NNF structure maintains the stoichiometric balance. (A) The detailed model matches data from Gene Dose Network Analysis experiments (18). After the knockout of a repressor gene (here, *Cry1*), the activity of the repressor promoters, controlled by an E-box, increases. This increases the expression of Rev-Erbs and reduces the activity of the activator promoter, controlled by a RORE. An opposite phenotype is seen when an activator (here, *Clock*) is knocked out. (B) The schematic explanation how the NNF structure maintains the stoichiometric balance. *Clock-/-* increases the stoichiometry (repressors/activators) because the activator decreases. The increased stoichiometry strengthens the core negative feedback and reduces the expression of the repressors and Rev-erbs. This weakens the additional negative feedback loop and increases the expression of other activators. The reduced expression of the repressors and increased expression of the activators decrease the increased stoichiometry to 1-1. (C) The detailed model matches data from *Rev-erbs-/-* (55, 58, 59). *Rev-erbα-/-* (50% reduction of transcription rate of the *Rev-erbs* due to the presence of Rev-erbβ) slightly shortens the period and has little effect on the expression level of *Per2, Cry1 and Bmal1*. Double knockout of the *Rev-erbα* and *Rev-erb*β (100% reduction of transcription rate of the *Rev-erbs*) increases the expression level of *Bmal1* and *Cry1*, but decreases that of *Per2*. All the values were normalized by the average of *Per2* expression level in WT.

3.3.4 A slow additional negative feedback loop improves the robustness

Our central hypothesis is that, as stoichiometry is more tightly regulated, oscillations will occur over a wider range of parameters. To confirm this, we varied the transcription rate of the activator (or activator concentration in the SNF) and the transcription rate of the repressor to determine which sets of parameters yielded oscillations. While the SNF, NNF and PNF structures have almost the same behavior with their nominal parameters (mean stoichiometry, amplitude and period, see Figure 3-8A), the NNF structure oscillated over the widest range of parameters and the PNF oscillated over the narrowest range of parameters in the simple model (Figure 3-9A and Figure 3-10A). Interestingly, as the activator becomes more stable (i.e. the additional negative feedback becomes slower), the NNF structure allows sustained oscillations over a wider range of parameters (Figure 3-10D). Indeed, the clearance rate of the activators is significantly slower than other circadian clock components (Table 3-3) (81).

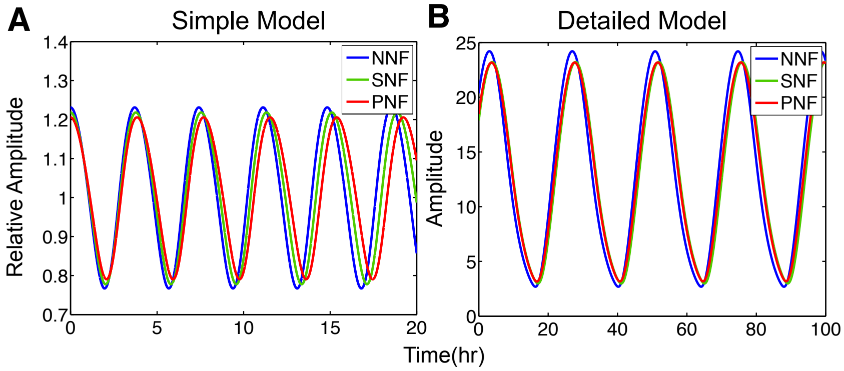

Figure 3-8. The timecourses of the three feedback loop structures (NNF, SNF and PNF). (A) The repressor (P) time profiles of simple models of the three structures. The amplitude is normalized by its average value. Here, we assumed $K_d = 10^{-5}$ and $\delta = 0.2$. γ in the NNF model and the PNF model were selected as 0.0043 and 0.0395, which made the NNF model and the PNF model have the same average activator concentration as in the SNF model (A=0.0659). With these parameters models have a similar stoichiometry, amplitude and period. (B) The Per2 mRNA time profile of detailed mammalian circadian clock models with three types of structures. In the SNF model, the level of the oscillating activators (Bmals and Npas2) is fixed at the average level in the original model (NNF). Transcription of Bmals and Npas2 are activated with E-box activation in the PNF model while they are repressed with E-box activation through REV-ERBs in the original model (NNF).

We also checked the role of the NNF structure in our detailed mammalian clock model. We modified the NNF structure of the detailed model to that of a SNF by fixing the activator (BMAL, CLOCK and NPAS2) concentration to the average value found in their WT simulations. We also constructed the PNF structure by converting the repressor (REV-ERBs) to an activator (e.g. the RORs) in the NNF structure. This did not significantly change the rhythms in the core feedback loop (Figure 3-8B), matching previous studies that showed that the loss or change in rhythms in the activators had little effect on the circadian rhythms (55). It is tempting to conclude that the additional feedback loops controlling activators are not important in the circadian clocks. However, when we changed the transcription rate of the repressor (*Per*) and activator (*Bmal*, *Clock* and *Npas2*), the original model (with a NNF structure) had the widest range of parameters where oscillations occur while the PNF structure had the narrowest range of parameters (Figure 3-9B). Interestingly, experiments have shown that REV-ERBs play a more dominant role than the RORs indicating that our proposed mechanism may play an important role in *in vivo* timekeeping (55). Thus, the choice of the additional feedback greatly affected the range of parameters where oscillations are seen.

We also examined the role of the additional negative feedback loop in a mathematical model of the *Drosophila* circadian clock (119). The original study that developed the model concluded that the NNF and SNF structures were equally likely to show oscillations. However, their study only changed transcription rates by 20%. With a larger perturbation of parameters, we found that the additional negative feedback loop significantly extends the range of parameters that yield oscillations (Figure 3-9C).

Table 3-3. Activators have a longer half-life than repressors.

	Mice Fibroblasts			***Drosophila* S2 cells**
Repressors	PER	PER^{P}	CRY	dPER
Half-Life (hr)	13	1.4	3.1-5.2	1.5
Activators	BMAL1	CLOCK	BMAL1-CLK	dCLOCK
Half-Life (hr)	47	13	3	6

The endogenous activators (BMAL1/CLOCK/BMAL1-CLOCK/clock) have longer half-life than the endogenous repressors ($\text{PER}/\text{PER}^{\text{P}}$/CRY/dPER) in mice fibroblasts and *Drosophila* S2 cells. This implies that feedback loops for the activators are slower than those of the repressors in the circadian clocks because the degradation rates of the components of the feedback loops are the key step that determines the time scale of a feedback loop. These data come from the following experimental studies: PER: Unphosphorylated PER1, 2 (61), PER^{P}: Phosphorylated PER1, 2 (120), CRY: CRY1, 2 (84, 106, 120), BMAL1: CLOCK unbinding BMAL1 (81), CLOCK: BMAL1 unbinding (81) CLOCK (81), BMAL1-CLOCK: dimer BMAL1-CLOCK (81), dPER: PER in *Drosophila* S2 cells (121), and clock: CLOCK in *Drosophila* S2 cells (122).

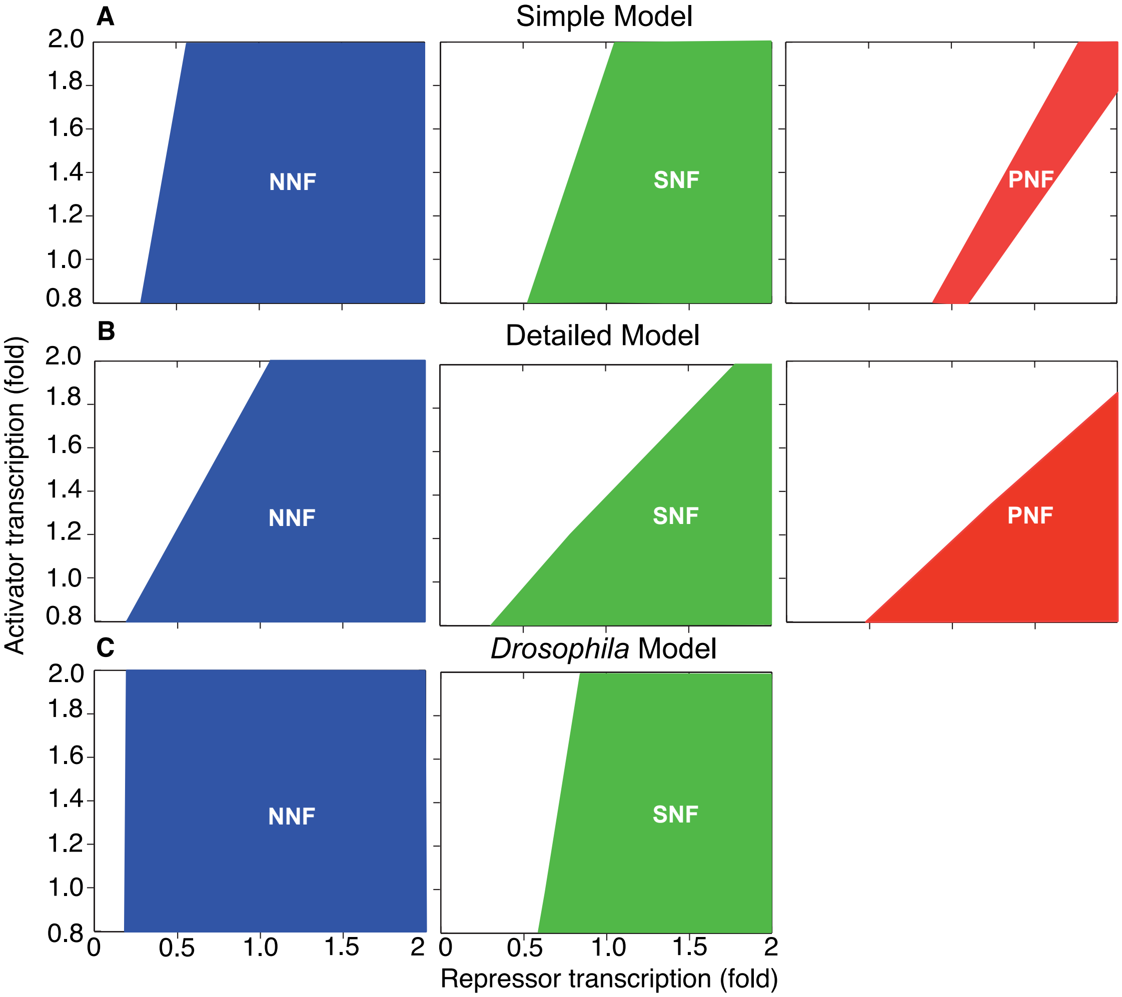

Figure 3-9. The NNF structure oscillates over the widest range of parameters.
(A) The transcription rate of the repressor and the activator are changed from their initial value, and the range of parameters where the rhythms persist is shown. Here, dissociation constant, K_d $=10^{-5}$ and clearance rate of activator, $\delta = 0.2$. When K_d is varied, the NNF model still has the widest range of parameters (Figure 3-10A). When δ increases, the range of parameters which generate the sustained rhythms decreases (Figure 3-10B). (B) repeats the tests with the detailed mammalian model and (C) uses a *Drosophila* model. Details about these plots, as well as our methods for generating them are described in Figure 3-8A-B. The bifurcation lines, which indicate where oscillations in the system are lost, were calculated with XPP-AUTO.

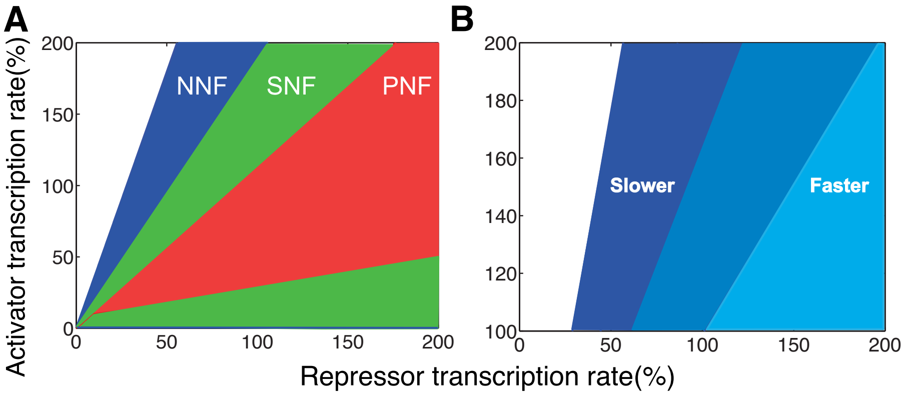

Figure 3-10 A slower additional feedback loop increases the range of parameters for which the system oscillates in NNF.
(A) The NNF structure has the widest range of parameters where the model oscillates regardless the dissociation constant. Here, K_d is decreased to 10^{-15} from 10^{-5} in Figure 3-9A. The range of parameters where the system oscillates is shown when the transcription rate of the repressor and activator were changed from their initial value (100%). As the dissociation constant decreases, the ranges of parameters, where the system oscillates, increase in all three structures. Here we assumed δ=0.2 (B) A slower additional feedback loop (i.e. more stable activator) increases the range of parameters for which the system oscillates in NNF. Here, δ is changed from 0.2 to 3. γ is also changed from 0.0043 to 0.0645 to keep the same expression levels of the activator. Other parameters are the same with those in Figure 3-9A.

3.3.5 A network design for cellular clocks with a fixed period.

The PNF structure can create a robust biological oscillator that has a tunable period when the additional positive feedback loop is fast (i.e. the activator degrades quickly) (3, 51, 52) (Figure 3-11A). Consistent with these findings, our simple model with the PNF structure has a tunable period for changes in gene expression levels (Figure 3-11C). However, the simple model with the NNF structure has a nearly constant period in the presence of large changes in gene expression levels (Figure 3-11B and D). Furthermore, this NNF structure becomes more robust as the additional negative feedback loop slows (i.e. the activator degrades more slowly) (Figure 3-10B) in contrast to the fast positive feedback of the tunable clocks (3, 51, 52). Consequently, our results propose two different designs for robust biological oscillators. The NNF structure (Figure 3-11B) is suitable for biological clocks in which the maintenance of a fixed period is crucial (e.g. circadian clocks). The PNF structure (Figure 3-11A) is suitable for the biological oscillators that need to tune their period (e.g. cell cycle or pacemaker in the Sino-atrial node) (3). This is also supported by mathematical analysis of the simple model (For more details, see Appendix B).

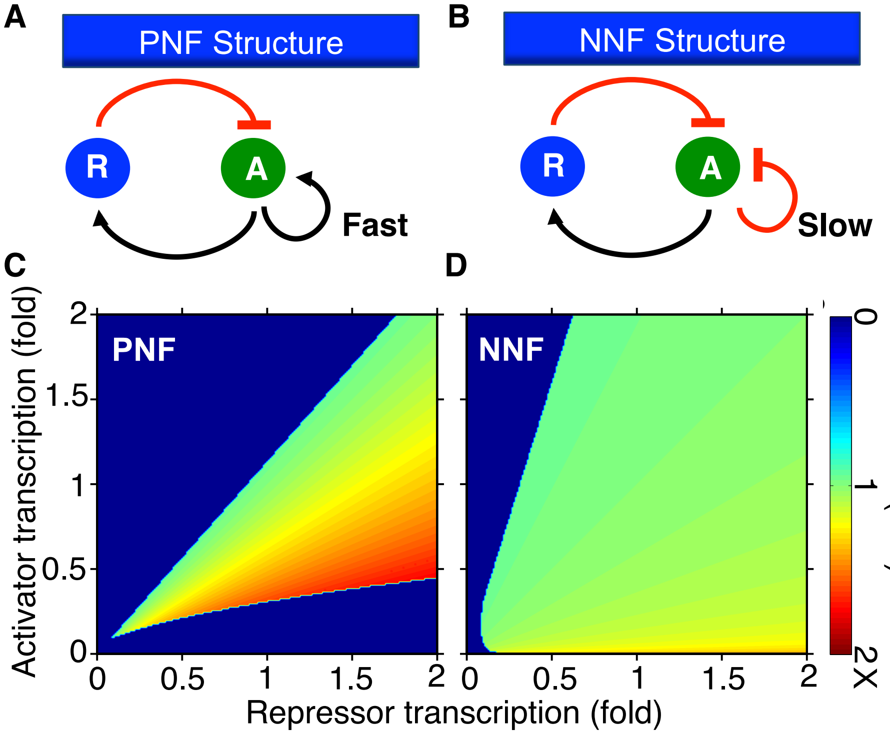

Figure 3-11. A design suitable for the cellular clocks with a fixed period.
(A) A single negative feedback loop with an additional fast positive feedback loop, with which activator (A) activates itself and degrades quickly. This structure has been identified in various biological oscillators like the cell cycle and pacemaker in the Sino-atrial node (3). (B) A single negative feedback loop with an additional slow negative feedback loop, with which activator (A) represses itself and degrades slowly. Circadian clocks in mammals or *Drosophila* have been shown to have this structure (Table 3-3) (53-55). (C and D) The period of the NNF is nearly constant for the perturbations in transcription rates while the period of the PNF changes about two-fold. Parameters used are as in Figure 3-10A. The period is plotted as a color where green refers to the period with the unperturbed parameters.

3.4 A systems pharmacology model of the mammalian circadian clock

3.4.1 Model description

We have investigated the mechanisms for a robust circadian timekeeping. Another interesting property of circadian clocks is entrainability to external signals, known as *zeitgebers* (e.g. light/dark (LD) cycle and temperature cycle) (48, 67). The *zeitgebers* synchronize circadian clock and environmental cycle by changing the level of clock components. If these external signals cannot reach the circadian timekeeping system, misalignments of circadian timing with the external environment occur, which can cause significant physiological problems including mood disorders (68-71). To treat the misalignment of circadian clocks with the external environment, pharmacological manipulation of the phase of circadian rhythms has been explored (72-75). In particular, PF-670462, an inhibitor for CK1δ/ε, one of the key kinases controlling the phase of circadian rhythms, can delay the phase of circadian rhythms. To study the effect of PF-670462 on circadian rhythms under LD cycle with seasonal variation, we incorporated PF-670462 into our mathematical model of intracellular mammalian circadian clocks (2).

In the new model, PF-670462 binds CK1δ/ε and inhibits the phosphorylation of CK1δ/ε (Figure 3-12). The inhibition of phosphorylation reduced the degradation rate of PER1/2, nucleus translocation of PER1/2 and binding rate of PER1/2 and CRY1/2 in the model. We considered the concentration of PF-670462 in four compartments: in plasma, brain tissue, cytoplasm and nucleus (Figure 3-12 and Table 3-4). To describe the import into and export out of these four compartments, 6 parameters were added. Because PF-670462 is absorbed to plasma very fast (<0.5h) (Figure 3-13A), we assumed that dosing is directly applied to the plasma compartment for simplicity. The addition of a new compartment (e.g. skin) describing drug administration did not change the behavior of model (data not shown). We also considered a clearance rate for free CK1δ/ε in plasma. The binding and unbinding rates of PF-670462 to CK1δ/ε are also considered. Since CK1δ/ε can freely exit the nucleus of the cell in the original model (2), we allowed for the rate of nuclear export of CK1δ/ε to be different when it is bound to PF-670462. Finally, we needed to choose an initial concentration of free PF-670462 in plasma when a 32 mg/kg dose is administrated (higher or lower doses can be determined by appropriately scaling this value). In total, this adds 11 parameters to the model while other parameters of the original model were left unchanged (Table 3-5). Via a simulated annealing method (123), the values of these new parameters were estimated by fitting to experimental data: timecourse of PF-670462 in plasma and brain, phase response curve (PRC) to PF-670462 and chronic dosing data of PF-670462.

Table 3-4. The variables used in the mathematical model to describe dynamics of CK1 inhibitor (PF-674062) in Figure 3-12.

Name	Symbol
The free plasma concentration of CK1 inhibitor	Inh_p
The free brain concentration of CK1 inhibitor	Inh_b
The free cytoplasm concentration of CK1 inhibitor	Inh_c
The free nucleus concentration of CK1 inhibitor	Inh_n
The concentration of CK1 complex unbound to CK1 inhibitor in cytoplasm	$CK1_c$
The concentration of CK1 complex bound to CK1 inhibitor in cytoplasm	$Inh{:}CK1_c$
The concentration of CK1 complex unbound to CK1 inhibitor in nucleus	$CK1_n$
The concentration of CK1 complex bound to CK1 inhibitor in nucleus	$Inh{:}CK1_n$

Table 3-5. Parameters of the mathematical model that describe dynamics of CK1 inhibitor (PF-670462).

Parameter Description	Symbol	Value
Initial free plasma concentration of CK1 inhibitor (32 mg/kg)	prodi	2562.61 nM
Transfer rate from plasma to brain for CK1 inhibitor	nlpin	6.33/hr
Transfer rate from brain to plasma for CK1 inhibitor	nepin	15.35/hr
Transfer rate from brain to cell for CK1 inhibitor	nlbin	0.486/hr
Transfer rate from cell to brain for CK1 inhibitor	nebin	19.2/hr
Nuclear localization rate constant for CK1 inhibitor	nlin	0.533/hr
Nuclear export rate constant for CK1 inhibitor	nein	0.192/hr
Nuclear export rate constant for CK1 and CK1 inhibitor complex	lnei	0.047/hr
Nuclear export rate constant for CK1	lne*	0.595/hr
Binding rate constant for CK1 inhibitor to CK1	inbin	0.421/nM hr
Unbinding rate constant for CK1 inhibitor to CK1	inubin	3.38/hr
Clearance rate constant for free CK1 inhibitor in plasma	uinp	1.653/hr
Ratio of cytoplasmic to nucleus compartment volume	Nf*	3.351

Presented value of prodi represents the initial free plasma concentration of CK1 inhibitor corresponding to 32 mg/kg dosing. The value of prodi is scaled according to the amount of dosing. For the *in vitro* simulations, presented value of prodi represents the initial free CK1 inhibitor concentration in medium after 5.2 μM dose, which is scaled according to the amount of dosing. * indicates the parameters of the original model, which are used to describe dynamics of CK1 inhibitor (Figure 3-12B).

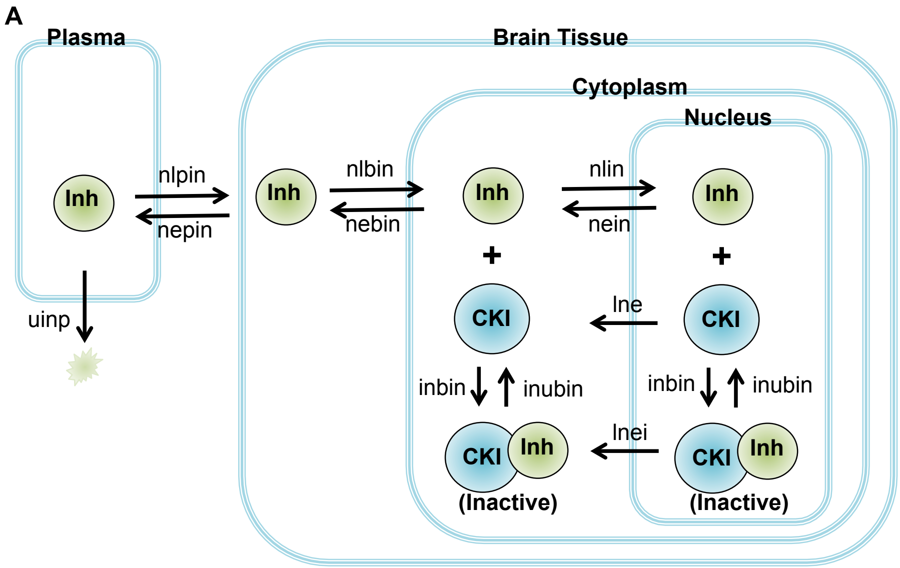

B

$$\frac{d[Inh_p]}{dt} = -nlpin[Inh_p] + nepin[Inh_b] - uinp[Inh_p]$$

$$\frac{d[Inh_b]}{dt} = nlpin[Inh_p] - nepin[Inh_b] - nlbin[Inh_b] + nebin[Inh_c]$$

$$\frac{d[Inh_c]}{dt} = nlbin[Inh_b] - nebin[Inh_c] - nlin[Inh_c] + nein[nInh] - inbin[Inh_c][CK1_c] + inubin[Inh : CK1_c]$$

$$\frac{d[CK1_c]}{dt} = -inbin[Inh_c][CK1_c] + inubin[Inh : CK1_c] + lne[CK1_n]$$

$$\frac{d[Inh : CK1_c]}{dt} = inbin[Inh_c][CK1_c] - inubin[Inh : CK1_c] + lnei[Inh : CK1_n]$$

$$\frac{d[Inh_n]}{dt} = nlin[Inh_c] - nein[Inh_n] - inbin \times Nf[Inh_n][CK1_n] + inubin[Inh : CK1_n]$$

$$\frac{d[CK1_n]}{dt} = -inbin \times Nf[Inh_n][CK1_n] + inubin[Inh : CK1_n] - lne[CK1_n]$$

$$\frac{d[Inh : CK1_n]}{dt} = inbin[Inh_n][CK1_n] - inubin[Inh : CK1_n] - lnei[Inh : CK1_n]$$

Figure 3-12. A simplified model diagram and equations describing the dynamics of the CK1 inhibitor (PF-670462).

(A) The concentration of CK1 inhibitor is considered in four possible locations: in plasma, brain tissue as well as the cytoplasm and nucleus of a neuron. Because PF-670462 is absorbed to plasma very fast (<0.5h) Figure 3-13A), we assumed that dosing is directly applied to the plasma compartment for the simplicity of the model. While only free inhibitor is considered in plasma and brain tissue, binding between inhibitor and its target CK1 is considered in cells. Since CK1 can freely exit the nucleus of the cell in the original model, potentially taking the inhibitor with it, we allow for the rate of nuclear export of CK1 to be different when bound to CK1 inhibitor. (B) Ordinary differential equations that describes the dynamics of the CK1 inhibitor. These equations were added to the original model systems (Kim and Forger, 2012). The parameters and variables are described in Table 3-4 and Table 3-5. Inh_p ,Inh_b , Inh_c , and Inh_n represent concentration of free CK1 inhibitor in plasma, brain, cytoplasm and nucleus. $CK1_c$ and $CK1_n$ represent concentration of CK1 complex unbound to CK1 inhibitor in cytoplasm and nucleus, respectively. $Inh:CK1_c$ and $Inh:CK1_n$ represent concentration of CK1 complex bound to CK1 inhibitor in cytoplasm and nucleus, respectively. Note that Nf indicates the ratio of nuclear to cytoplasmic compartment volume, which was used in the original model (Kim and Forger, 2012). Here, all concentrations are defined with respect a reference volume (cytoplasmic volume) according to the convention of intracellular circadian clock modeling (28, 79, 101, 124).

3.4.2 Model validation

The estimated parameters reflect the PK and PD of PF-670462 accurately. Our parameters are fitted to the disposition profiles of PF-670462 free drug concentration in plasma and brain tissue following a single 32 mg/kg subcutaneous (s.c.) dose (Figure 3-13A). Furthermore, interestingly, the model correctly predicts CK1δ/ε occupancy, the fraction of bound CK1δ/ε by PF-670462 (Figure 3-13B), suggesting accurate prediction of the binding affinity between PF-670462 and CK1δ/ε.

Next, we compared simulations of our model with previous *in vitro* experimental studies that measured the effect of PF-670462 on clock gene expression (78). Our model successfully predicts dose dependent period changes of clock gene expression in SCN (Figure 3-13C). Matching previously published data (78), the model also predicts that period prolongation by CK1δ/ε inhibition is mainly due to the prolongation of the interval between peaks of Per2 and Bmal1 (Figure 3-13D).

Finally, we compared the phase shifts of behavior produced by light and CK1δ/ε inhibition in the model and in the experiments. For this, we explored PRCs, which are measured by giving a stimulus (e.g. light) to circadian rhythms at different times and measuring the effect on the phase of rhythms (125, 126). Previous studies have shown that PRCs of circadian rhythms to light pulses have both advance and delay regions (90, 127, 128), but the PRC to dosing of PF-670462 shows only delays (76). That is, light stimuli can advance or delay circadian rhythms depending on the timing of stimuli, but a dose of PF-670462 always delays the phase, regardless of dosing timing. Our mathematical model successfully reproduced these two PRCs (Figure 3-13E) and was also able to reproduce both a constant stable delay induced by LD chronic dosing and a cumulative increasing delay induced by DD chronic dosing at ZT11 (Figure 3-13F and Figure 3-14).

To test the reliability of estimated parameters, we also simulated PRCs to dosing of PF-670462 in the presence of parameter perturbations. Even with the significant perturbations of parameters, the model successfully produced PRCs that show only delays (Figure 3-15). These simulations indicate that the model can accurately and robustly reproduce behavioral data in response to CK1δ/ε inhibition in a LD cycle.

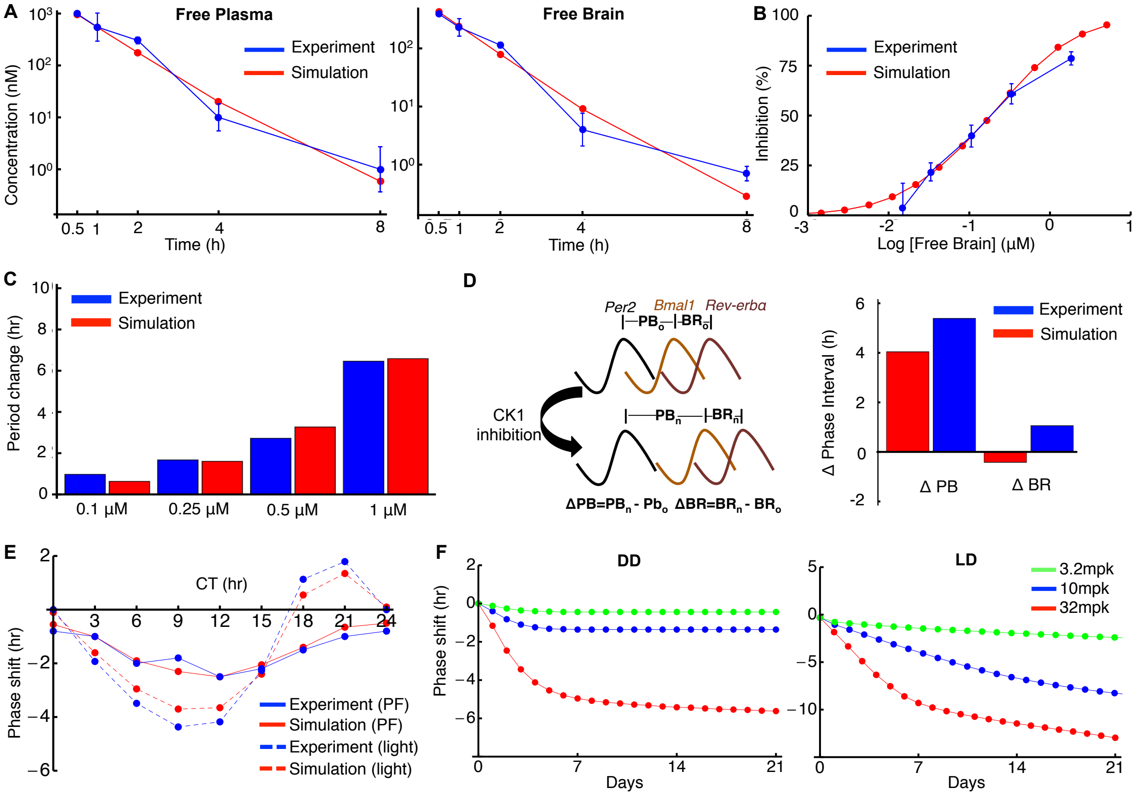

Figure 3-13. Comparison between simulations and experimental data: PK/PD of PF-670462 (A and B), clock gene expression phase change (C and D), and behavioral phase changes (E and F).

(A) Experimentally measured disposition profiles of free PF-670462 in plasma and brain tissue after a single 32 mg/kg s.c. dose were compared with simulations. The units of concentrations of simulations are scaled to match experimental data. (B) The model correctly predicts CK1 occupancies corresponding to concentrations of free brain PF-670462. (C) The model predicts dose-dependent prolongation of circadian period, matching a previous experimental study of SCN slice (78). (D) The model predicts that PF-670462 induced prolongation of period in Figure 3-13C is mainly due to the lengthened internal phase relationship between the Per2 peak and the Bmal1 peak (ΔPB), matching the experimental data of the previous study (78). PB_0 and PB_n represent the difference of peak timing of *Per2* and *Bmal1* mRNA without and with 1μM dosing of PF-670462, respectively. ΔPB is the difference between PB_n and PB_0. (E) The model successfully reproduces PRCs to a 12-hour, 100 lux light pulse (128) and a 50 mg/kg dose of PF-670462 (76). (F) Simulations of 32 mg/kg chronic dosing of PF-670462 at ZT11 induces a constant stable delay under 12:12 LD, but not under DD, matching our experimental data (Figure 3-14). The experimental data of Figure 3-13A, E and F were used in estimation of parameters.

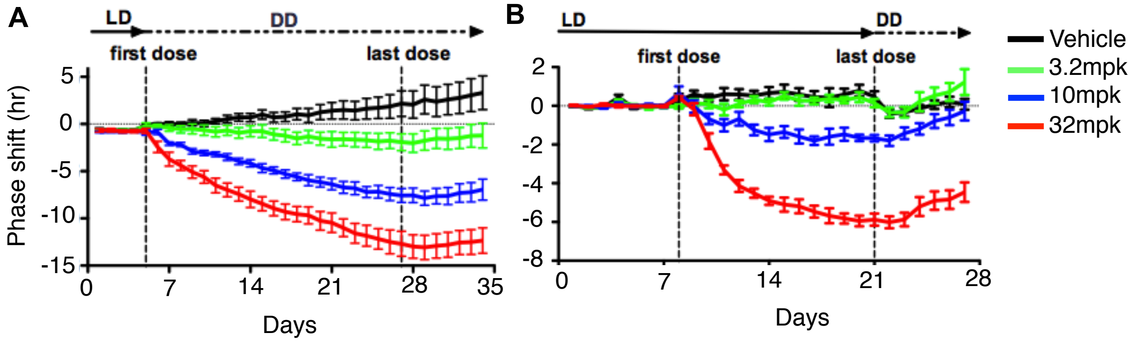

Figure 3-14. Chronic dosing of PF-670462 induces a constant stable delay under LD, but not under DD.

Mice were maintained in 12:12 LD and circadian measures followed for 7d prior to dosing. In each experiment, mice were either shifted into DD or kept in LD, and daily treated with vehicle or PF-670462 (3.2, 10, 32 mg/kg) at CT11 (ZT11), red dash indicates days of dosing. After the last dose, mice in LD were shifted into DD and all groups followed for an additional 7d. Daily phase angle was measured as the start of the circadian signal relative to that defined by the 7d prior to dosing. DD chronic dosing induces continually accumulating delays regardless of dosing amount (A), but LD chronic dosing induced the constant stable phase delays (B).

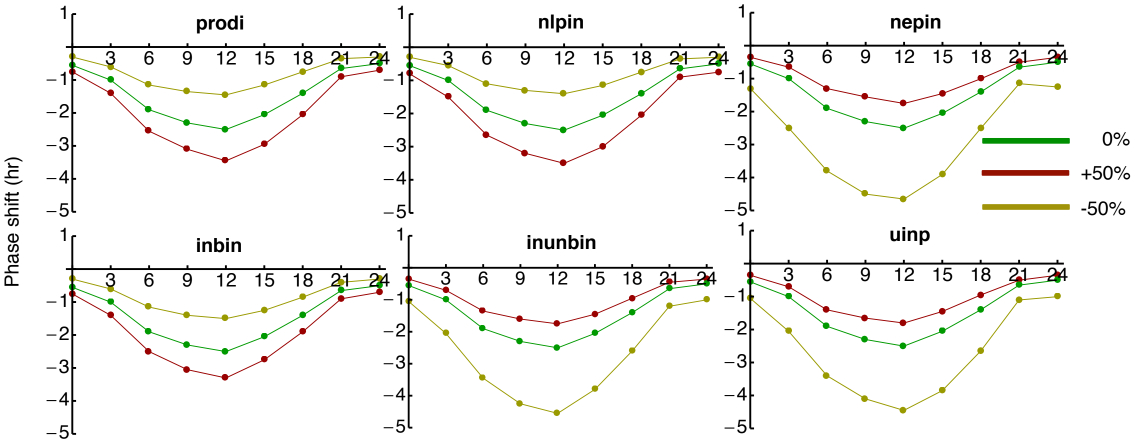

Figure 3-15. The variations of PRC to PF-670462 in the presence of parameter perturbations.

11 new parameters are added to describe the dynamics of PF-670462 in the mathematical model (Table 3-5). We tested how increasing or decreasing these parameters by 50% changed the PRC to PF-670462. After changing each parameter, PRCs to the dosing of 50 mg/kg PF-670462 were simulated. Even with the significant perturbations, the model successfully generates the all delay PRC, which is an important characteristic of PF-670462. Representative PRCs with changes in six parameters are shown

3.5 Modeling chronic manipulation of circadian rhythms via PF-670462

3.5.1 Chronic dosing with different dosing timing

Our mathematical model was successfully able to reproduce experimental data on the effects of a light pulse or CK1δ/ε inhibition on circadian rhythms (Figure 3-13). With our mathematical model, we simulated daily PF-670462 treatment under various conditions. First, we investigated whether LD chronic dosing with 32 mg/kg of PF-670462 can induce a constant stable phase delay regardless of dosing timing. Based on our experiments showing that LD chronic dosing at ZT11 caused a constant stable phase delay (Figure 3-14B) (76), one might assume that LD chronic dosing at other times might also lead to constant stable phase delays. However, the model surprisingly predicted that this was not the case. In fact, our model predicts that stable entrainment does not occur, i.e. no stable relationship between the LD cycle and circadian phase is achieved, when the inhibitor is applied during the early night (Figure 3-16A). This contrasts with late night dosing which is predicted to produce minimal phase shifts. The model also predicts that stable entrainment can occur during daytime dosing, however the magnitude of the phase delay is predicted to vary greatly depending on the dosing timing (Figure 3-16A). Thus, we predict that dosing timing must be very carefully controlled to achieve a desired phase delay.

Since the timing of exact daily dosing is predicted to have a great effect on the ability of the circadian clock to entrain to an LD cycle, we next wondered if the accuracy of the dosing timing was also an important factor. To explore this, we simulated 32 mg/kg chronic dosing that varies somewhat but centers around either ZT2, 5, 8 or 11 under a 12:12 LD cycle (see the legend of Figure 3-16B for details). While entrainment could still be seen in the presence of variations in dosing timing, the phase of the circadian clock was, as expected, less controlled particularly near ZT11 (Figure 3-16B). In fact, the variability in dosing timing often prevented entrainment from occurring at ZT11 (Figure 3-16B). These results indicate that LD chronic dosing in the morning or early afternoon is more likely to induce a stable and robust phase delay in the presence of a less controlled dosing schedule.

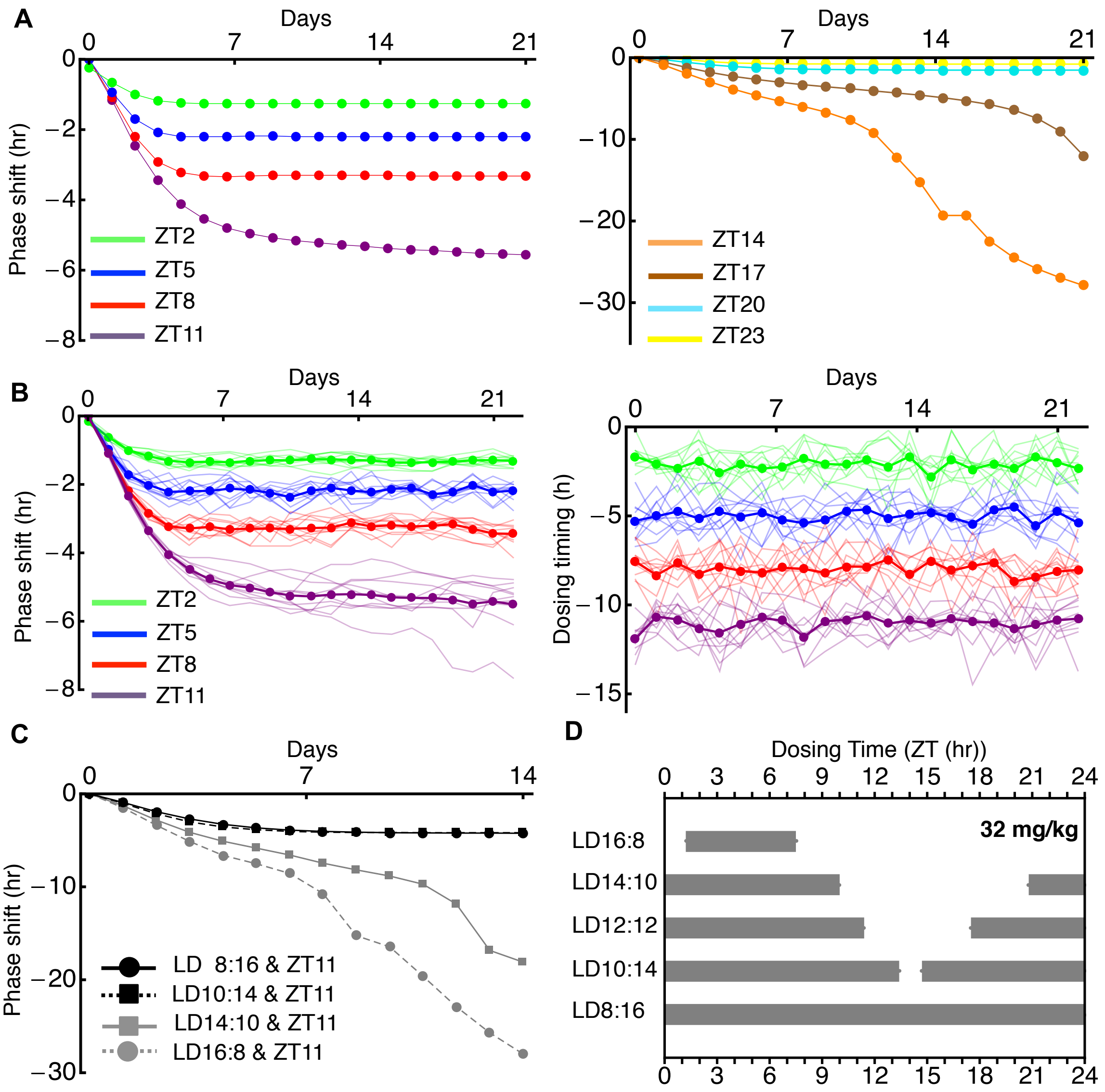

Figure 3-16. Simulations of chronic dosing under various conditions: Different dosing timings (A), less controlled dosing timings (B), and different day lengths (C).
(A) 32 mg/kg chronic dosing under 12:12 LD with different dosing timings were simulated. The model predicts that the chronic dosing in the morning, but not at early night induces a constant stable phase delay. (B) The same simulations of Figure 3-16A for day dosing were performed in the presence of perturbations in dosing timing (left panel). Here, the dotted lines represent the average of 10 individual simulations (thin lines). Dosing timings were perturbed daily by choosing dosing timing from normal distribution with mean of a original dosing timing and standard deviation of 1hr. The perturbations of dosing timings are illustrated in the right panel: thin lines are perturbed dosing timings and dotted lines are the average dosing timing of 10 individual simulations. (C) 32 mg/kg chronic dosing at ZT11 under various day lengths were simulated. The model predicts that the chronic dosing under short days, but not long days induces a constant stable delay. (D) The simulated ranges of dosing timings that induce a stable entrainment for 3 weeks dosing (32 mg/kg) are represented as gray bars under various day length conditions.

3.5.2 Chronic dosing under different day lengths

The effect of the seasonal change of day length on chronic dosing was explored. Since light opposes the phase delays induced by chronic dosing and produces the stable entrainment (Figure 3-14B and Figure 3-16A), we initially expected that increasing the amount of available light (e.g. to a 16:8 LD cycle) would allow for entrainment over a wider range of dosing times. However, our simulations showed the opposite results: As the light duration lengthens, entrainment is less likely to occur, and was lost for ZT11 dosing (Figure 3-16C). The ranges of dosing timings that induces the stable entrainment become narrower as day length increases (Figure 3-16D). These results indicate that dosing schedules should be adjusted according to short and long day lengths, corresponding to winter and summer, to ensure stable entrainment.

3.5.3 Chronic dosing with different intrinsic periods of circadian rhythms

The effect of different intrinsic period on chronic dosing was also investigated. If free-running period is longer than 24h, the phase would be delayed every day, and this difference in period must be made up by phase shifts from light and the inhibitor to achieve entrainment. Due to the additional delays induced by longer free-running period, stable entrainment is less likely to occur as the free-running period becomes longer, which matches simulations of the model (Figure 3-17).

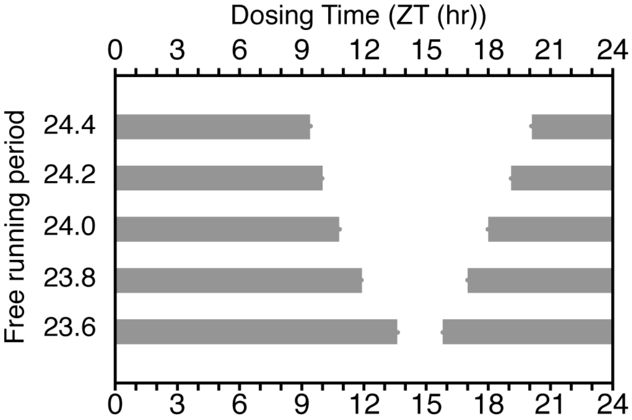

Figure 3-17. The stable entrainment is less likely to occur when free-running period is long. The ranges of dosing timing that induce a stable entrainment for 3weeks dosing (32 mg/kg) are represented as gray bars. The time scale of the model was adjusted to simulate different free running period.

3.6 Discussion

3.6.1 Summary

In this chapter, we have investigated two important properties of circadian clocks by developing and analyzing mathematical models of circadian clocks: "How does circadian clocks maintain 24-rhythms over a wide range of conditions?" and "How can the phase of circadian clocks be manipulated pharmacologically under a LD cycle?"

Regarding the first question, our work identifies several key mechanisms that allow 24-hour rhythms in the circadian clocks of higher organisms: 1) Proper stoichiometric balance between the activators and the repressors, 2) tight binding between activators and repressors, 3) the NNF structure, and 4) longer half-life of activators than repressors. These mechanisms synergistically generate rhythms with periods robust to gene dosages (Figure 3-11D). The range of the stoichiometry where the rhythms occur widens as binding between activators and repressors tightens (Figure 3-3D). Moreover, the NNF structure regulates the expression of activators as well as repressors to balance stoichiometry (Figure 3-6B and Figure 3-7A). For instance, the increased stoichiometry (elevated repressor concentrations) strengthens the repression in the core negative feedback loop and reduces the expression of the repressors (e.g. Pers and Crys) and Rev-erbs. The decreased expression of Rev-erbs weakens the additional negative feedback and increases the expression of activators (Bmal1 and Npas2), which lowers the stoichiometry (Figure 3-7B). When this is done on a slower timescale, so that the basics of the 24-hour timekeeping are unaffected, the robustness of the rhythms is enhanced (Figure 3-10B).

Regarding the second question, we found that chronic dosing of PF-670462 under LD cycle can induce a constant stable behavior shift, which depends on dosing amount, dosing timing, intrinsic period and day lengths. The model predicts that the stable entrainment due to the chronic CK1 inhibition under LD is less likely to occur when PF-670462 is dosed at early night and when day length becomes longer (Figure 3-16A and

C). Furthermore, simulations predict that stable entrainment is less likely to occur as free-running period becomes longer (Figure 3-17).

3.6.2 Relation to previous experimental data

Many experimental observations could be interpreted as mechanisms by which the mammalian circadian clock balances stoichiometry. When the repressor (CRY) is overexpressed or the repressor (PER) is removed, the activator (BMAL1) concentration is found to increase or decrease, respectively (129, 130). When a repressor's expression is reduced, the expression of other repressors is increased and the expression of activators is decreased (18). Knockdown of activators yields opposite effects (18). Both our detailed and simplified NNF models confirm these results (Figure 3-6B and Figure 3-7A-B). Additionally, the rhythms of the mammalian circadian clock persist even after the transcription of all clock genes are reduced significantly (50). In agreement with this data, both the detailed and the simple model oscillate after significant reduction of the transcription rates of both activators and repressors because their stoichiometry is maintained (Figure 3-9). Our study also suggests an underlying mechanism (ultrasensitive response) for a previous experimental observation showing that the robustness of circadian rhythms is enhanced by making the level of PER-CRY closer to that of CLOCK-BMAL1 in mouse fibroblasts (Appendix B and Figure 3-5A) (62).

Experimental data also support the role of the slow additional negative feedback loop in regulating circadian timekeeping in higher organisms. The timecourse of the activator (BMAL1 in mammal or CLK in *Drosophila*) seems to be controlled mainly by the additional negative feedback loop (Rev-Erbs or Vrille) (53-55). The elimination of additional positive feedback has little effect on circadian clocks in contrast to other cellular clocks based on the PNF structure (3, 54, 55, 116). Furthermore, a key step, the clearance rate of the activators, which governs the timescale of the additional feedback loop, is significantly slower than other circadian clock components (Table 3-3) (81). Removing the slow additional negative feedback loops in the mammalian clock (*Rev-erb*$\alpha^{-/-}$) yields timekeeping where the period is not as well-maintained (57). Moreover, recent studies have confirmed a pivotal role for the additional negative feedback loop for regulating the circadian rhythms via double knockout of *Rev-erbα* and *Rev-erbβ* (58, 59). Thus, our proposed mechanism of robust circadian timekeeping matches known data on the mammalian circadian clock. Further comparison with known experimental data is shown in Figure 3-18.

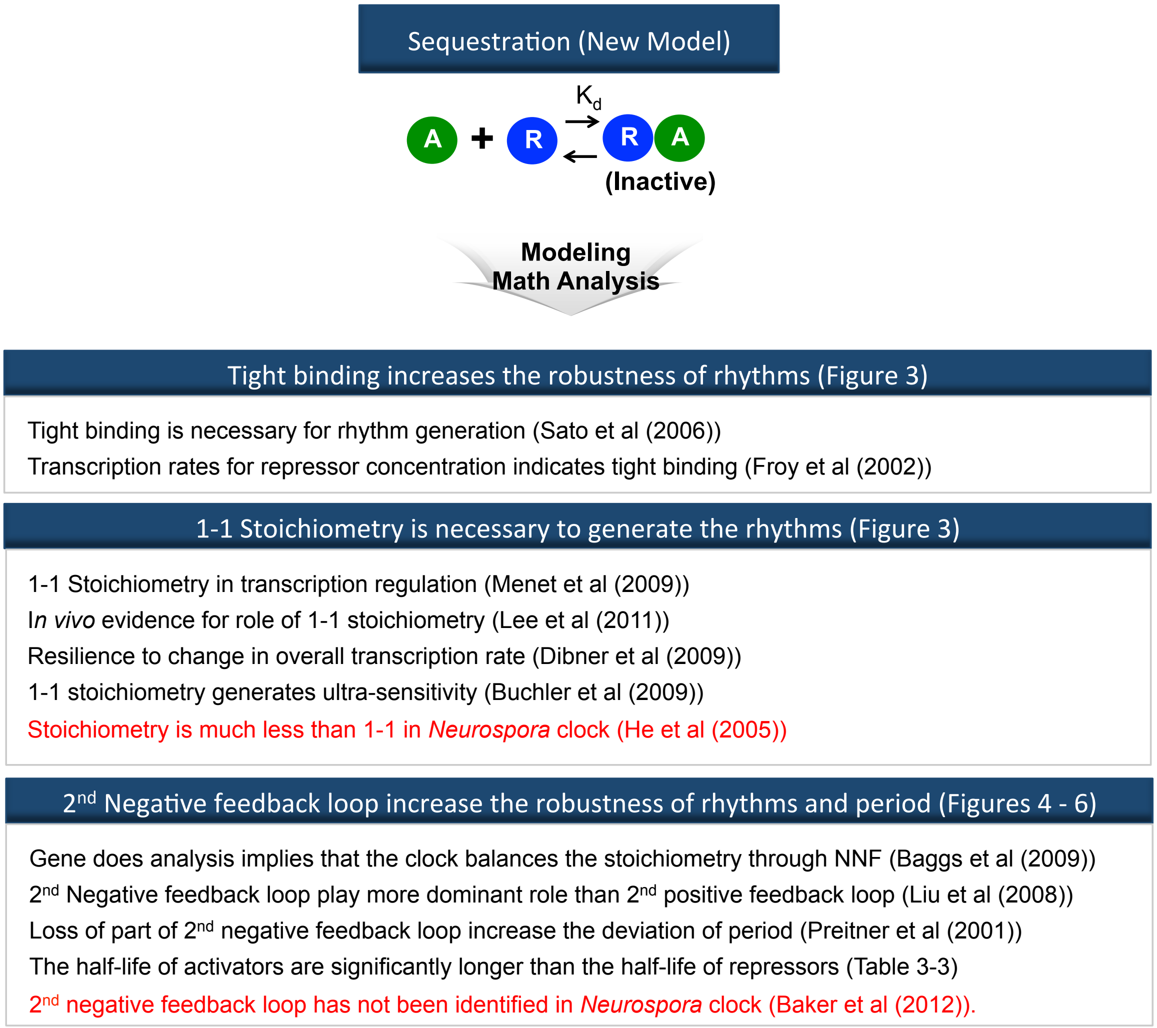

Tight binding increases the robustness of rhythms (Figure 3)

Tight binding is necessary for rhythm generation (Sato et al (2006))
Transcription rates for repressor concentration indicates tight binding (Froy et al (2002))

1-1 Stoichiometry is necessary to generate the rhythms (Figure 3)

1-1 Stoichiometry in transcription regulation (Menet et al (2009))
In vivo evidence for role of 1-1 stoichiometry (Lee et al (2011))
Resilience to change in overall transcription rate (Dibner et al (2009))
1-1 stoichiometry generates ultra-sensitivity (Buchler et al (2009))
Stoichiometry is much less than 1-1 in *Neurospora* clock (He et al (2005))

2nd Negative feedback loop increase the robustness of rhythms and period (Figures 4 - 6)

Gene does analysis implies that the clock balances the stoichiometry through NNF (Baggs et al (2009))
2nd Negative feedback loop play more dominant role than 2nd positive feedback loop (Liu et al (2008))
Loss of part of 2nd negative feedback loop increase the deviation of period (Preitner et al (2001))
The half-life of activators are significantly longer than the half-life of repressors (Table 3-3)
2nd negative feedback loop has not been identified in *Neurospora* clock (Baker et al (2012)).

Figure 3-18. Comparison of the predictions of the new model and experimental data. The predictions of the new model based on the protein sequestration match experimental data of circadian clocks of higher organisms, but not *Neurospora* circadian clocks.

3.6.3 Relation to previous modeling work

Our study is the first circadian modeling study that shows the importance of a balanced stoichiometry in rhythm generation. Our results for the SNF structure match a previous model based on the protein sequestration (114) which focuses on other mechanisms, e.g. slow RNA dynamics, that do not play a role in circadian clocks. We have identified a basic mechanism of tight binding and protein sequestration for generating high sensitivity, similar to what has been proposed in the cell cycle and synthetic studies (112), as the key rhythm generating mechanism in our model. Previous circadian clock models do not use this mechanism, and a careful justification, based on experimental data from higher organisms, of the mechanisms for generating high sensitivity and, consequently, oscillations, in these models has yet to be performed (100). In fact, several of these mechanisms have been called into question (28).

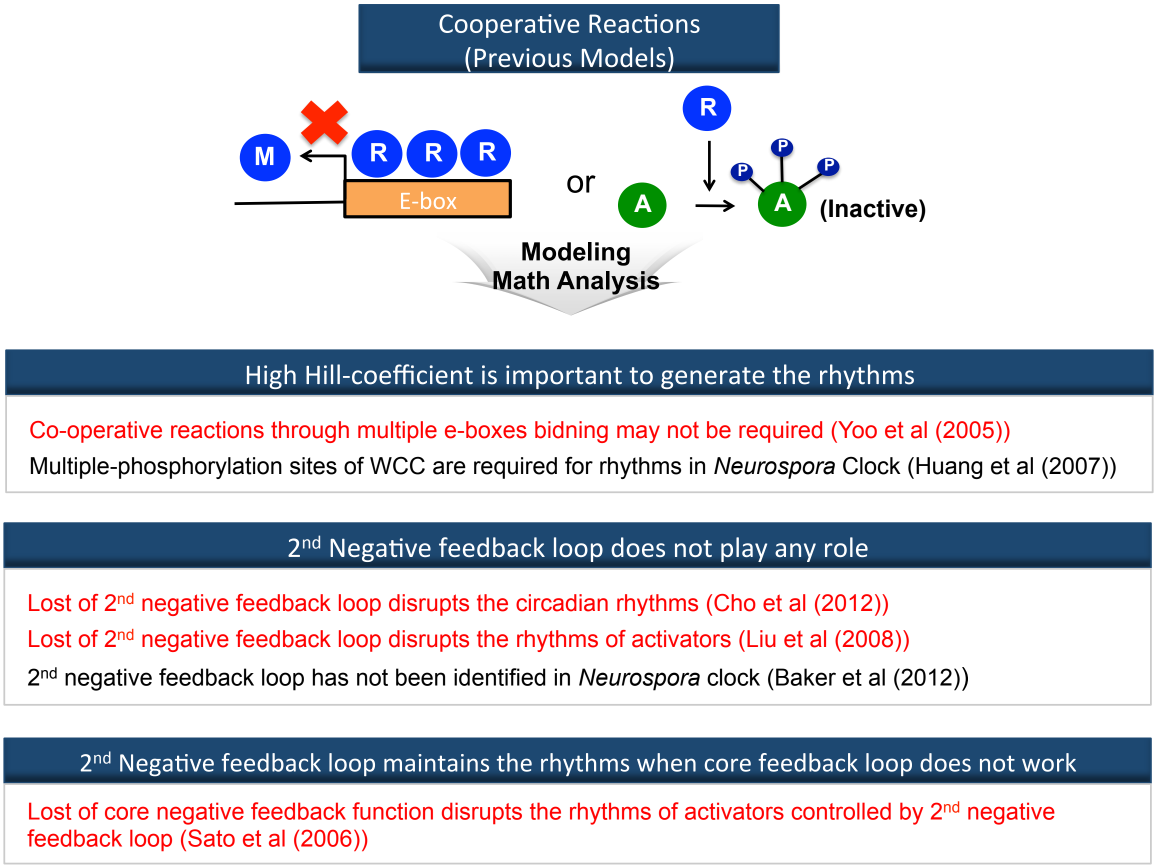

High Hill-coefficient is important to generate the rhythms

Co-operative reactions through multiple e-boxes bidning may not be required (Yoo et al (2005))

Multiple-phosphorylation sites of WCC are required for rhythms in *Neurospora* Clock (Huang et al (2007))

2nd Negative feedback loop does not play any role

Lost of 2nd negative feedback loop disrupts the circadian rhythms (Cho et al (2012))

Lost of 2nd negative feedback loop disrupts the rhythms of activators (Liu et al (2008))

2nd negative feedback loop has not been identified in *Neurospora* clock (Baker et al (2012))

2nd Negative feedback loop maintains the rhythms when core feedback loop does not work

Lost of core negative feedback function disrupts the rhythms of activators controlled by 2nd negative feedback loop (Sato et al (2006))

Figure 3-19. Comparison of the predictions of the previous models and experimental data. The predictions of the previous models based on the cooperative reactions (e.g. cooperative binding or phosphorylation on multiple sites) match experimental data of *Neurospora* circadian clocks, but not higher organisms circadian clocks (31, 102, 131, 132).

Previous models have used different mechanisms for rhythm generation (e.g. high-Hill coefficients) and have proposed different roles for the additional negative feedback loop. They have proposed that the additional negative feedback loop is capable of independent oscillations, even when the core negative feedback loop was removed (102, 132). However, despite much experimental study, no oscillations have yet been found from this additional feedback loop in isolation (115) and the known phenotypes of knockout of genes in this additional feedback loop had not been correctly predicted (57, 102). Moreover, other previous studies argued that the additional negative feedback loop is not important (131), which does not match with recent experimental data on the mammalian circadian clock (58, 59). We claim that the additional negative feedback loop is not an independent oscillator, nor ancillary, but acts to regulate stoichiometry.

Interestingly, the predictions of previous modeling studies (31, 131) match experimental data from the *Neurospora* circadian clock, in which a 1-1 stoichiometry is not important and the additional negative feedback loop seems to not play an important role (133). Our predictions match experimental data from circadian clocks in higher organisms (Figure 3-18 and Figure 3-19).

3.6.4 Proposed experiments based on model predictions

Our most important prediction may be the following: when the stoichiometry between activators and repressors is within a fixed range, oscillations are sustained, and outside this range oscillations are damped (Figure 3-3). This can be tested by measuring the relative concentration of activators and repressors in many tissues and in the presence of several possible mutations which lead to damped or sustained rhythms. This has been done in WT fibroblasts and liver (62, 63), but has not been done in other tissues or mutants. Moreover, we note that these previous experiments were done in population cell assays, whereas single cell measurements may be needed to determine whether damped oscillations are the result of damped rhythms in single cell, or greater population desynchrony (134, 135).

The behavior of isolated SCN neurons is similar to fibroblasts in that mutations of circadian genes can easily lead to arrhythmicity (103). We note that intercellular coupling in the SCN not only synchronizes SCN neurons, but also increases transcription of *per1* and *per2 (110),* which may balance stoichiometry and help sustain rhythms when repressors are effectively removed (Table 3-1 and 3-2). Thus, we predict that increasing transcription of *per1* and/or *per2* could enhance rhythmicity in isolated SCN neurons similar to what is seen in fibroblasts (63). Moreover, our model predicts that cells with low stoichiometry (e.g. isolated SCN neurons) shows larger phase-shifts in response to light than cells with 1-1 stoichiometry (e.g. SCN slices) (data not shown). It would be interesting future work to see whether different cell types have different PRCs depending on their stoichiometry.

We also predict that tight binding between activators and repressors is required for rhythmicity (Figure 3-3D). Several studies have identified binding sites for PER and CRY on BMAL1 and CLOCK (85, 115, 136). Point mutations in binding sites can generate different binding affinities between PER-CRY and BMAL1-CLOCK. Comparing the experimentally measured binding affinities of these mutants, with the resultant rhythms, or lack thereof, would directly test this prediction.

Loss of the additional negative feedback loop (e.g. in the Rev-erbs-/-, constitutive expression of Rev-erbs or constitutive expression of BMAL) is predicted to cause the intracellular circadian clock to oscillate over a much narrower range of conditions (Figure 3-9). It would be interesting to test whether these cells would have less temperature compensation or would lose rhythms more easily when other genes are knocked out (e.g. *Cry2*$^{-/-}$*, Per1*$^{-/-}$). Moreover, we predict that in the Rev-erbs$^{-/-}$, rhythms persist in cell types with a balanced stoichiometry, but not in poorly balanced cells (Figure 3-9). It would be interesting future work to investigate whether SCN and peripheral clocks have different phenotypes of Rev-erbs$^{-/-}$ depending on their stoichiometry. We also predict that Rev-erbs$^{-/-}$ cells show a wider period distribution than WT (Figure 3-11).

Our modeling and analysis also predicts that relatively stable activators (e.g. BMAL1 and CLOCK) in the additional negative feedback loop allow rhythmicity over a wide range of conditions (Figure 3-10B). These activators can be destabilized with point mutations (95). Simply destabilizing the activators might lead to lower activator concentrations and unbalance stoichiometry, which is also predicted to reduce rhythmicity. However, we predict a loss of rhythmicity when these activators are destabilized, even when the overall activator concentrations are controlled for.

Perhaps the most direct way to test our model is to build the clock described in our simple NNF model using the tools of synthetic biology. Other synthetic clocks have been built, and the design we propose is not more complex than what has been previously built (3, 51, 52). Validation could first be done in an analog electric circuit, even though this might be much less convincing. Building a synthetic clock would be of particular importance since it would be the first synthetic clock predicted to have a tightly regulated period.

3.6.5 Future work

Further work should explore the role of the NNF structure in the presence of molecular noise (137, 138). Here, we studied the role of an additional negative feedback loop controlling the activators of the circadian clocks of higher organisms. Future work could consider the functions of the additional negative feedback loops in other organisms. In particular, the plant circadian clock has a different feedback loop structure than the mammalian or *Drosophila* circadian clocks (139). It would be interesting to see if our ideas carry over to other organisms and other cellular clocks. Furthermore, other types of feedback loops in the circadian clocks of higher organisms could be explored. Here, we found that balancing stoichiometry properly might be a universal principle of biological timekeeping. This finding not only is in agreement with experiment data from the circadian clocks in higher organisms, but even in agreement with the circadian clock in cyanobacteria as well (140). It would be interesting to test the role of stoichiometry in other cellular clocks, such as developmental clocks.

Our work has also shown that chronic dosing of PF-670462 under LD can induce a constant stable behavior shift in dose dependent manner (Figure 3-14) (78, 141). The effect suggests that LD chronic dosing can be used to treat circadian rhythm sleep disorders, in particular advanced sleep phase disorder (ASPD) which is characterized by a several hour earlier sleep schedule than what is desired. Currently, treatment of ASPD involves timed exposure to bright light in the evening (chronotherapy) or dosing of melatonin in the morning, each of which have their own limitations due to the lengthy process and sedating effect, respectively (73, 142-144). These issues may be addressed by the LD chronic dosing of PF-670462 (Figure 3-14). Although there are side effect concerns since CK1δ/ε are key regulators of diverse cellular growth and survival processes (145), a recent study showed that PF-670462 has only a modest effect on cell proliferation (146). With an accurate and detailed mathematical model of mammalian circadian clock (79), we studied how dosing amount, dosing timing and day length affect the chronic dosing induced phase delay (Figure 3-16). This will lead to the reliable use of the LD chronic dosing of PF-670462 to modulate the phase of circadian rhythms in real life. Many studies have shown that bipolar disorders and mood disorders are associated with disrupted circadian rhythms (68-70, 147). Specifically, phase misalignment is frequently present in mood disorders and rhythm amplitude is often reduced (71, 147, 148). This suggests that the chronic dosing of PF-670462 under a LD cycle could be a potential way to treat mood disorders on the basis of modulating the phase stably and increasing the amplitude of circadian rhythms. Indeed, recent studies showed that the chronic inhibition of CK1δ/ε rescues pathological behaviors in animal models of mania and alcoholism (149, 150). Future work should test whether chronic dosing can treat these and other models of mood disorders (151-155).

Chapter 4 Mechanisms that Enhance Sustainability of p53 Pulses

4.1 Introduction

Cancer is a group of various diseases caused by failure in regulating tissue growth, in which, the proliferating cells without control form tumors and invade other parts of the body (156, 157). The failure of regulation of cell growth is usually caused by malfunction of oncogenes or tumor suppressor genes, which promote growth or inhibit cell division, respectively (47, 158). p53 protein is one of the most important tumor suppressors, which regulates key functions to prevent tumorigenesis in response to cellular stress (e.g. DNA damage and genomic instability), such as DNA repair, cell cycle arrest and apoptosis (25). That is, if DNA is damaged, p53 stops cell cycle and repairs DNA damage. If DNA damage is too severe to repair, p53 initiates apoptosis, programed cell death, to eliminate damaged cells from the organism (159). Since p53 protein plays pivotal roles in preventing tumorigenesis, mutant of p53 protein has been linked to more than half of all human cancers (160).

Recent studies have found that depending on the type of stresses, p53 protein exhibits different dynamical behaviors. While p53 protein levels are low in the absence of stress, transient DNA double-strand breaks (DSBs) that occur during a normal cell-cycle lead to spontaneous pulses of p53 (161). A single pulse of p53 can also be triggered by UV irradiation (162). The most dynamic behavior of p53 is induced by severe DNA damage. When severe DSBs are caused by γ-irradiation or radiomimetic drugs, cells generate a series of p53 pulses (26, 163-165). Interestingly, these different dynamical behaviors appear to be highly correlated with appropriate responses of p53 to different types of stresses (6, 161, 162).

The γ-triggered p53 pulses have three notable features: 1) the pulse amplitudes are independent of γ-irradiation strength, 2) the pulses are sustained so long as DSBs persist (i.e. undamped pulses) and 3) while the period of the pulses is tightly regulated, the amplitude is highly variable. The molecular mechanisms underlying these unique features of p53 pulses have been explored both experimentally and theoretically. Among many feedback loops regulating p53 (166), a negative feedback loop between p53 protein and E3 ubiquitin ligase Mdm2 is considered to be a core mechanism that generates p53 oscillations (167-172). Recently, mathematical modeling and subsequent experiments have found an additional feedback loop between upstream kinase ATM and p53 through WIP1, which is also required to sustain p53 pulses with amplitudes that are independent of γ-irradiation strength (163, 173). In addition to the molecular mechanisms underlying p53 pulses, the relationship between the dynamics of p53 and its output functions, such as DNA repair or cell cycle arrest have also been widely studied both theoretically and experimentally (6, 161, 174-178). In light of the considerable theoretical and experimental focus on dynamics of p53 pulses and the role of these pulses, it is somewhat surprising that very little attention has been paid to how cells robustly sustain p53 pulses, even in the presence of perturbation (e.g. intrinsic noise or genetic perturbation) (170, 178). Given the importance of sustaining p53 pulses for cell fates in response to severe DNA damage (6, 161), it is of considerable interest to understand how cells can sustain p53 pulses over a wide range of conditions.

In other biological oscillatory systems, mechanisms that sustain robust rhythms in the presence of perturbations have been widely studied. Importantly, it has been shown that adding additional positive or negative feedback loops to a core negative feedback loop can often contribute to maintaining rhythms over a wide range of environmental conditions (2, 3, 79). For instance, an additional positive feedback is essential for high amplitude rhythms of active mitosis promoting factor (MPF) in the presence of intrinsic noise (3, 7). An additional negative feedback loop also allows molecular circadian rhythms to persist in the presence of genetic perturbations (79). Together with additional *intracellular* feedback loops, *intercellular* feedback loops through coupling among neighboring cells also often contribute to generating robust rhythms. For instance, while the circadian rhythms of clock gene expression in single cells are easily disrupted by intrinsic noise or genetic mutations, circadian rhythms in coupled cells can persist robustly even in the presence of significant genetic perturbations (23, 103). Cellular coupling can also tightly regulate the periods and the amplitudes of c-AMP rhythms in *Dictyostelium* (179) and membrane potential spikes in neurons (180, 181). The coupling has been investigated as a mean to reduce the effects of noise on rhythms, but more recent studies have found that coupling and noise often synergistically enhance rhythms in calcium systems and circadian clocks (23, 182).

The identification of mechanisms that enhance robustness of rhythms in various biological oscillatory systems has lead to the question of whether similar mechanisms that enhance robust γ-triggered p53 pulses exist. Indeed, several positive feedback loops acting on p53 through PTEN, dapk1, c-Ha-Ras and DDR1 have been identified (183-186). However, these feedback loops do not appear to be essential for sustaining p53 pulses (1). A recent study identified a novel positive feedback loop between p53 and Rorα, which may enhance the sustainability of p53 pulses (187). In this positive feedback loop, p53 promotes gene expression of Rorα in response to DNA damage, and increased RORα protein stabilizes p53. Together with additional feedback loops acting on p53, a recent study found radiation induced bystander effect (RIBE) (188), which may be a potential mechanism that couples p53 pulses of neighboring cells. RIBE refers to DNA damage of *un-irradiated* cells induced by the molecular signals produced by their neighboring *irradiated* cells. Among various molecular signals involving RIBE, Cytochrome-c (cyt-c) can act as an excitatory signal for p53 pulses in neighboring cells (27). More specifically, p53 activation induced by DNA damage stimulates the mitochondrial release of cyt-c, which activates p53 in *un-irradiated* neighboring cells. However, whether cyt-c can couple p53 pulses in *irradiated* cells has yet to be investigated.

In this chapter, we develop a new mathematical model of p53 pulses to explore molecular mechanisms that enhance sustainability of p53 pulses in the presence of DNA damage. Our new model is able to reproduce many key experimental observations that discern characteristics of p53 pulses. By simulating this model both deterministically and stochastically, we find that a positive feedback loop between p53 and Rorα plays a pivotal role in sustaining p53 pulses over a wide range of conditions. Moreover, we find that noise can often prevent p53 pulses from dampening even after mutations of key molecular species that generate p53 pulses. Interestingly, we also found that p53 pulses in DNA-damaged cells have characteristics similar to Type II resonator neurons, which are prone to synchronize their spikes through excitatory couplings. Similar to Type II neurons, even a weak coupling via cyt-c can synchronize p53 pulses of cells and significantly increase the chance that p53 pulses will be sustained in response to DNA damage.

4.2 A Mathematical model of p53 pulse regulatory system

4.2.1 Model description

To explore mechanisms that enhance sustainability of p53 pulses, we have developed a new mathematical model that describes the dynamics of p53 pulses. Our model is based on the delay-differential equation (DDE) model of Batchelor et al. 2008, which made important contributions to understanding the mechanisms underlying p53 pulse generation (6, 161-163). In particular, their model found that DNA damage induced activation of ATM, an upstream signaling kinase for p53 phosphorylation, and that deactivation of ATM by p53 via WIP1 triggers a series of p53 pulses (163). Batchelor's model tracks the temporal changes of five molecular species: $p53_{inactive}$, $p53_{active}$, Mdm2, Wip1 and ATM-P (Figure 4-1A). The interactions among these five species can be described by three negative feedback loops:

1) ATM-P induced $p53_{active}$ promotes production of Mdm2 and Mdm2 induces ubiquitination of p53,
2) ATM-P induced $p53_{active}$ promotes production of Wip1 and Wip1 mediates dephosphorylation and inactivation of $p53_{active}$, and
3) ATM-P induced $p53_{active}$ promotes the production of Wip1 and Wip1 dephosphorylates and inactivates ATM-P (162, 163).

In addition to these negative feedback loops, Mdm2 phosphorylation by ATM-P inactivates and destabilizes Mdm2.

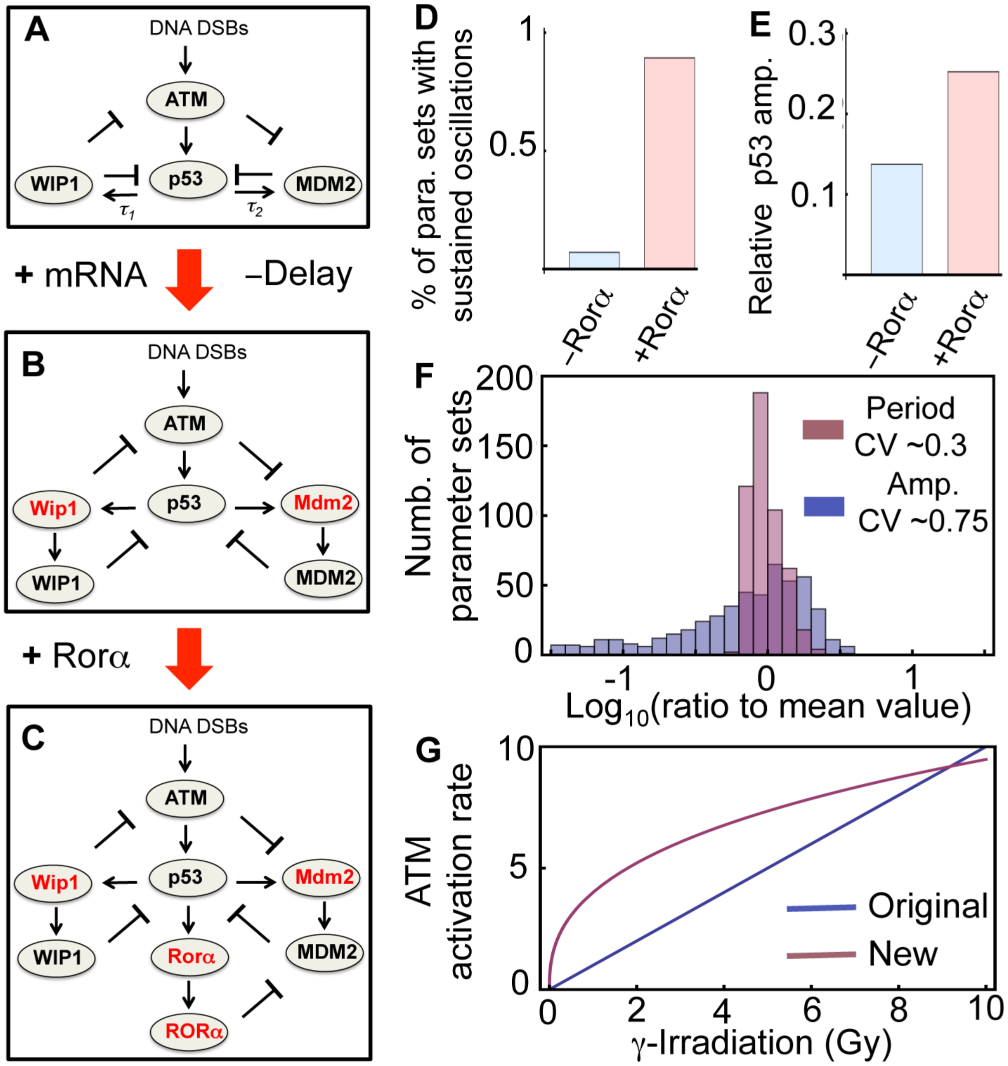

Figure 4-1. The new model of p53 pulse regulatory system.
(A) A schematic diagram of Batchelor's DDE model (163). (B) Extension of Batchelor's model that includes intermediate steps instead of explicit time delays. (C) Our full model including an additional positive feedback loop between p53 and Rorα as well as intermediate steps (see Appendix C for a detailed model description). (D-E). Comparison between the model without Rorα (Figure 4-1B) and with Rorα (Figure 4-1C) indicating the probability of p53 rhythm occurrence (D) and average relative amplitude of p53 (E). For models without and with Rorα, newly added parameters were randomly chosen until 500 parameter sets were found that generate sustained pulses of p53 in response to 10Gy irradiation. For 500 parameter sets, mean relative amplitude of p53 pulses were measured in the two different models. (F). The distributions of periods and amplitudes of our new model (Figure 4-1C) with the 500 parameter sets. (G). In the Batchelor's model, the activation rate of ATM is proportional to the strength of γ-irradiation (163), but in the new model, the activation rate of ATM saturates for the strong γ-irradiation.

We begin developing our new model by first converting the DDEs used in Batchelor's model into ordinary differential equations (ODEs). Our rationale for this modification is that DDEs often generate rhythms in systems whose structures are not likely to produce rhythms naturally (2, 189). We, therefore, want to ensure that the p53 pulses in our model are not explicit delay-induced instabilities, which often occur in nonlinear feedback systems. Another reason for converting to ODEs is that it is more difficult to perform stochastic simulations of DDEs than ODEs because methods to introduce stochasticity into the explicit time delays in DDEs have not been fully developed (190). Two explicit time delays, 0.7 hours and 1.25 hours for $p53_{\text{active}}$-dependent production of Mdm2 and Wip1, respectfully were used in Batchelor's model. We removed these explicit delays and introduced intermediate steps (mRNAs) required for the production of MDM2 protein and WIP1 protein (Figure 4-1B). The two new ODEs that describe dynamics of Mdm2 and Wip1 mRNA are given below.

$$\frac{d[Mdm2]}{dt} = \beta_{mm}[p53_{active}] + \beta_{mi} - \alpha_{mm}[Mdm2]$$
$$\frac{d[Wip1]}{dt} = \beta_{im}[p53_{active}] - \alpha_{im}[Wip1]$$

To test whether the newly introduced intermediate steps without the explicit time delays are sufficient to generate sustained p53 pulses after 10 Gray (Gy) irradiation, new parameters associated with the equations for the mRNA of Mdm2 and Wip1 were randomly searched until 500 parameters yielding oscillations were found (Table C-4). Here, we defined sustained pulses as undamped oscillations. However, the probability of rhythm occurrence was very low (<0.1%) (Figure 4-1D). Considering robustness as a design principle of biological systems whose essential functions are nearly independent of varying biochemical parameters (191-193), the low chance of rhythm occurrence implies that the current ODE model with intermediate steps for protein production might lack one or more essential components for generating rhythms.

One potential issue with the current ODE model is that it consists of only negative feedback loops. It is well known that an additional positive feedback loop often enhances the robustness of rhythms in other biological oscillatory systems (2, 3, 170). Indeed, a recent study identified a positive feedback loop between Rorα and p53, in which after γ-irradiation, $p53_{active}$ induces the expression of Rorα and increased RORα protein inhibits the Mdm2 dependent degradation of p53 (187, 194). We added this positive feedback loop into the model (Figure 4-1C), which added two ODEs to describe dynamics of Rorα mRNA and Rorα protein.

$$\frac{d[Ror\alpha]}{dt} = \beta_{rm}[p53_{active}] + \beta_{rmi} - \alpha_{rm}[Ror\alpha]$$
$$\frac{d[ROR\alpha]}{dt} = \beta_{r}[Ror\alpha] - \alpha_{r}[ROR\alpha]$$

Moreover, since the MDM2-dependent degradation rate for p53 is inhibited by Rorα, the MDM2-dependent degradation rate of p53 is modeled as follows:

$$\alpha_{mpi}[Mdm2][p53_{inactive}] \longrightarrow \alpha_{mpi}[Mdm2][p53_{inactive}]\frac{T_{rr}}{T_{rr}+[Ror\alpha]}$$
$$\alpha_{mpa}[Mdm2][p53_{active}] \longrightarrow \alpha_{mpa}[Mdm2][p53_{active}]\frac{T_{rr}}{T_{rr}+[Ror\alpha]}$$

With this new model with the positive feedback loop (Figure 4-1C), we randomly searched the new parameters associated with this positive feedback loop as well as those for the mRNA of Mdm2 and Wip1 again (Table C-4). Surprisingly, the addition of this positive feedback loop significantly increased the chance of rhythm occurrence (>10 fold) (Figure 4-1D). Another benefit of adding the positive feedback loop is that it increases the average amplitude of sustained p53 pulses generated with the 500 parameter sets (Figure 4-1E). We also analyzed the distributions of periods and amplitudes of pulses induced by these 500 parameter sets (Figure 4-1F). With the additional positive feedback loop, the new ODE model was able to capture a distinct characteristic of p53 pulses: a large variation in amplitude, but little variation in periods (26). Since recent studies have shown that the sustainability of p53 pulses is essential for the repair of DNA damage, our study further indicates that the positive feedback loop between p53 and Rorα can play an important role in the appropriate response of p53 to DNA damage (6). Indeed, Rorα$^{-/-}$ cells failed to regulate apoptosis in response to DNA damage (187).

Finally, previous experimental studies found a nonlinear relationship between the amount of DNA damage and the activation rate of ATM (195, 196). We therefore changed the mechanisms for ATM activation induced by DSBs in Bachelor's model, where ATM activation is linearly proportional to the extent of DNA damage (163). In the new model, ATM activation becomes more sensitive to small amounts of DNA damage and becomes saturated for large amounts of DNA damage (Figure 4-1G) as described below, in which the production rate of active ATM is more sensitive to a weak γ-irradiation (IR) and saturates for strong IR:

$$IR \longrightarrow \beta_s \frac{IR^{N_g}}{T_g + IR^{N_g}}$$

We found that this modification is critical to simulating the correct responses of p53 systems, such as period distributions in response to different strengths of γ-irradiation (see below). The complete system of ODEs is described below (see Table C-1 for the description of parameters):

$$\frac{d[p53_{inactive}]}{dt} = \beta_p - \beta_{sp}[p53_{inactive}]\frac{[ATM]^{n_s}}{[ATM]^{n_s} + T_S^{n_s}} - \alpha_{pi}[p53_{inactive}] - \alpha_{mpi}[Mdm2][p53_{inactive}]\frac{T_{rr}}{T_{rr} + [ROR\alpha]} + \alpha_{ipa}[WIP1][p53_{active}]$$

$$\frac{d[p53_{active}]}{dt} = \beta_{sp}[p53_{inactive}]\frac{[ATM]^{n_s}}{[ATM]^{n_s} + T_S^{n_s}} - \alpha_{mpa}[Mdm2][p53_{active}]\frac{T_{rr}}{T_{rr} + [ROR\alpha]} - \alpha_{ipa}[WIP1][p53_{active}]$$

$$\frac{d[Mdm2]}{dt} = \beta_{mm}[p53_{active}] + \beta_{mi} - \alpha_{mm}[Mdm2]$$

$$\frac{d[MDM2]}{dt} = \beta_m[Mdm2] - \alpha_{sm}[ATM][MDM2] - \alpha_m[MDM2]$$

$$\frac{d[Wip1]}{dt} = \beta_{im}[p53_{active}] - \alpha_{im}[Wip1]$$

$$\frac{d[WIP1]}{dt} = \beta_i[Wip1] - \alpha_i[WIP1]$$

$$\frac{d[ATM]}{dt} = \beta_s \frac{IR^{n_g}}{T_g + IR^{n_g}} - \alpha_{is}\frac{[WIP1]^{n_i}}{[WIP1]^{n_i} + T_i^{n_i}}[ATM] - \alpha_s[ATM]$$

$$\frac{d[Ror\alpha]}{dt} = \beta_{rm}[p53_{active}] + \beta_{rmi} - \alpha_{rm}[Ror\alpha]$$

$$\frac{d[ROR\alpha]}{dt} = \beta_r[Ror\alpha] - \alpha_r[ROR\alpha]$$

4.2.2 Model validation

Our extensions and modifications of Batchelor's model added 14 parameters to the list of parameters in their model. We selected new parameters that were able to reproduce many important experimental findings, including the mean and variation of the period and amplitude of p53 pulses with various strengths of the irradiation dose and mutation phenotypes (Table C-1). Other parameter values were maintained from the original model, which were carefully selected based on experimental data (163). We also analyzed the sensitivity of all parameters (Table C-1 and Figure 4-3), which indicates that all species in the model play important role in regulating p53 pulses. With the new parameter set, our model was able to generate sustained pulses of p53 in response to 5Gy irradiation (Figure 4-2A). To compare simulations of the new model with experimental data, stochastic simulations were also performed with Gillespie's algorithm to reflect molecular fluctuations in experimental data (197). Gillespie's algorithm has been widely used to study the effect of molecular noise on the dynamics of biochemical and genetic systems (137, 167, 198). The lists of reactions together with the probability for their occurrence are described in Table C-2. Hill equations and Michaelis-Menten equations of the deterministic model were also used in the stochastic simulation by assuming fast time scales for the elementary reactions underlying these equations (199, 200). This stochastic model also generated sustained p53 pulses after 5Gy irradiation (Figure 4-2B).

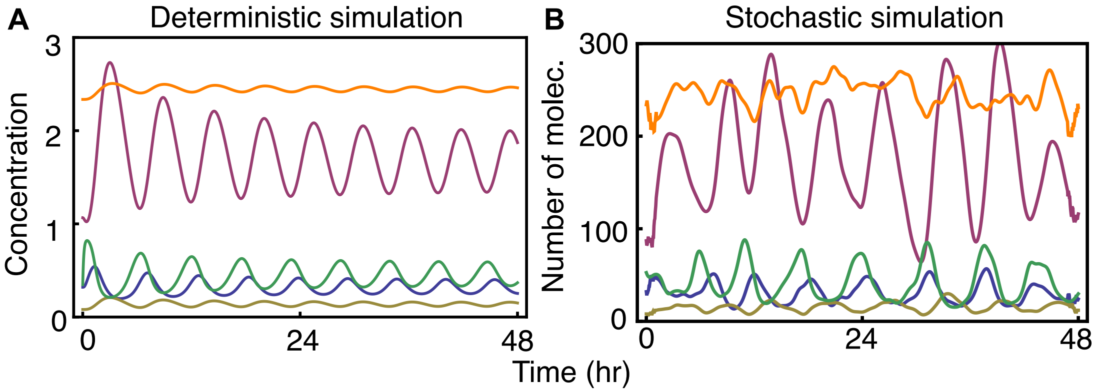

Figure 4-2. Deterministic and stochastic simulation of the new model after 5Gy irradiation. (A). Deterministic Simulation. (B). Stochastic simulation with Gillespie algorithm. Total p53 (Blue), active ATM (Green), WIP1 (Yellow), MDM2 (Brown), and RORα (Orange).

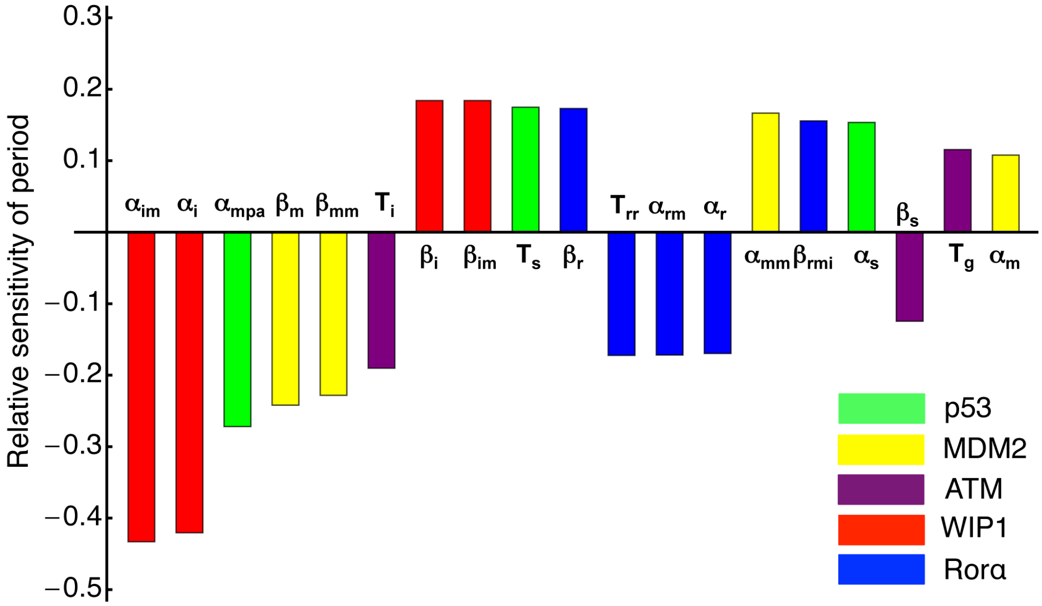

Figure 4-3. Parameters with relative sensitivity higher than 0.1.
If there exists a dominant feedback loop in the biological oscillatory system, most parameters with high sensitivities are related to the core feedback loop (79, 201). However, in our p53 model, parameters with sensitivity higher than 0.1 are associated with all species, indicating that all species and feedback loops in the model play important roles in regulating p53 pulses. Furthermore, the period of p53 pulses shows the most sensitive response to the perturbations of degradation rates of Wip1 mRNA and protein, which propose interesting future experiments.

First, with Gillespie's algorithm, we simulated the period distributions of MDM2 oscillations in 500 cells after 0.3, 5, and 10 Gy irradiations. To consider the heterogeneity among cells (202), the original parameters of the model were randomly perturbed by multiplying e^X $(X \sim N(0, 0.2))$. The simulations showed that the distributions of periods become narrower as γ-irradiation strength increases, which is consistent with experimental data (Figure 4-4A and B) (26). With low strength γ-irradiation (0.3 Gy), MDM2 rhythms showed a wide range of periods (e.g. 9hr and 6hr) (Figure 4-4C). Moreover, as the strength of γ-irradiation becomes stronger, the fraction of cells oscillating with period 4-7 hours increases, matching experimental data (Figure 4-4D) (26).

Next, among oscillating cells, we measured the average amplitude, peak width of p53 and time delay between the peaks of p53 and Mdm2 for first five peaks of pulses (Figure 4-5A-C). All of these values were well matched with experimental data (26). Moreover, the model simulated a significantly larger variation in the peak amplitudes than those in the peak width of p53 or delay between peak timing of p53 and Mdm2 (Figure 4-5D-F), as shown in previous experiments (26). Taken together, the new model can successfully reproduce key features of p53 pulses induced by γ-irradiation.

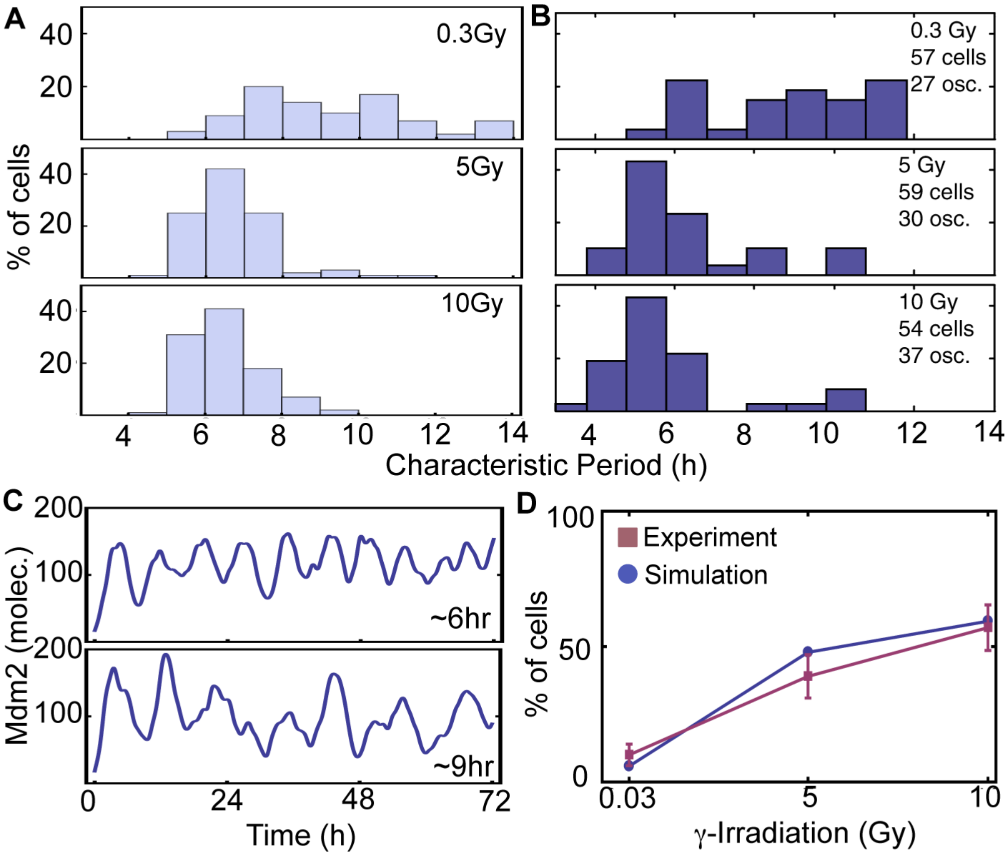

Figure 4-4. Period distributions of cells in response to different strengths of γ-irradiation. (A) Simulated histograms of the characteristic period of Mdm2 in 100 cells over the first 72h after irradiation in response to different strengths of irradiation. To determine whether stochastically simulated time courses of p53 or Mdm2 are oscillating, we used autocorrelation method, which is used to detect pitch in speech. The stochastically simulated time courses are sampled every 0.05 hr and then sampled signals are smoothed through Gaussian smoothing. The autocorrelation of signals are then calculated and if the autocorrelation value is higher than 0.2, we concluded that the time courses are oscillating. Moreover, the detected pitch period is used as the period of time courses. (B) Experimentally measured histograms of the characteristic period of Mdm2-YFP signals in MCF-7 cells exposed to different strengths of γ-irradiation (Figure. 3 in (26)). Reprinted by permission from Macmillan Publishers Ltd: Molecular Systems Biology 2006 (doi: 10.1038/msb4100068). (C) Examples of simulated Mdm2 oscillations with short (~6hr) and long (~9hr) periods after 0.3Gy irradiation. (D) Fractions of cells (out of the total number of cells) with a characteristic period of 4–7 h in response to different strengths of irradiation match experimental data (26).

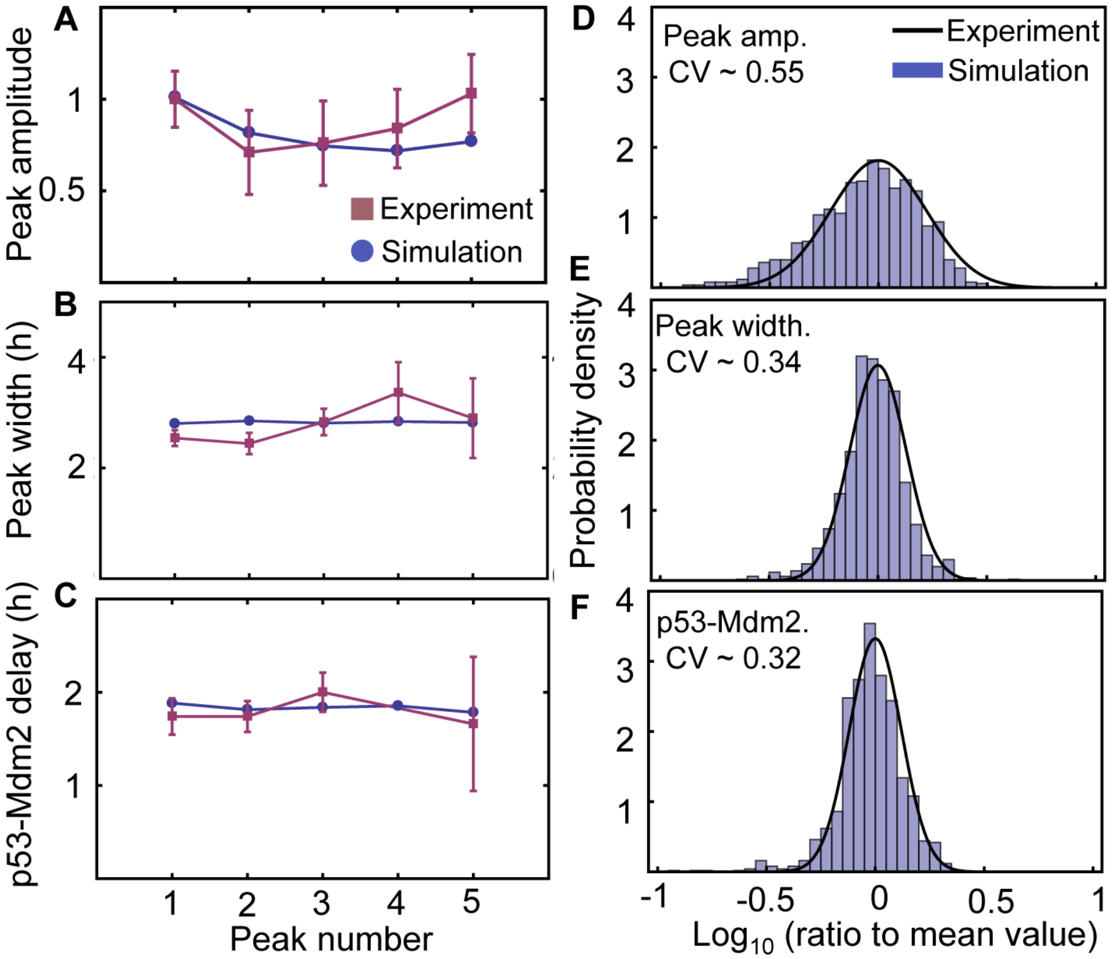

Figure 4-5. Average amplitude, width, and time delay of oscillation peaks and their variance. (A–C) Stochastically simulated average values of first five p53 pulse peaks in 200 cells exposed to 5 Gy irradiation match experimental data (Fig. 4 in (26)). (A) Average amplitude. (B) Average peak width (full width with half-amplitude). (C) Average time delay between the p53 peak and the subsequent Mdm2 peak. (D–F) Simulated distributions of the individual peak amplitudes, peak widths, and time delays between the p53 peaks and Mdm2 peaks divided by its mean value match those measured experimentally (Figure 4 in (26)). In particular, while amplitude shows a large variation, but peak width and peak delay show small variations. Experimental data is reproduced by permission from Macmillan Publishers Ltd: Molecular Systems Biology 2006 (doi: 10.1038/msb4100068).

4.3 Mechanisms that enhance the sustainability of p53 pulses

4.3.1 Noise can enhance the sustainability of p53 pulses in mutated cells

To quantify the role of each molecular species in the model, we simulated various types of mutations. Given 10Gy irradiation, the model with Wip1 knockout generates a single peak followed by a high steady state of p53 instead of sustained pulses of p53, matching a previous experimental study (Figure 4-6A) (163). It is known that SNP309 (polymorphism of mdm2 promoter) increases expression of Mdm2 mRNA about 10 times and induces the low stable state of p53 instead of oscillations after γ-irradiation (203, 204). We tested this in our model by increasing the transcription rate of Mdm2 by a factor of 10 and found that this causes the same behavior that was observed experimentally (Figure 4-6B). Finally, the model predicts that Rorα is also essential to generate sustained pulses of p53 in the presence of 10 Gy γ-irradiation (Figure 4-6C).

While deterministic simulations predict that sustained p53 pulses will not occur with these three types of mutations, stochastic simulations predict that the sustained pulses often occur even with these mutations (Figure 4-6D-F). In particular, the model showed clear oscillations of p53 in Rorα$^{-/-}$ cells. Interestingly, previous studies also showed that noise could often induce rhythms in other biological oscillatory systems, such as the circadian clock, by moving the system away from its natural steady state (23). To see how often noise can induce the sustained pulses with these mutations, we conducted a simulation of 200 cells with Gillespie algorithm. Here, we again assumed heterogeneity among cells as we did previously. Cells with any one of three mutations showed a lower chance of rhythm occurrence than WT cells (Figure 4-6G). In particular, Wip1$^{-/-}$ cells had the lowest probability of sustaining pulses. Moreover, the amplitudes of pulses were also significantly reduced with these mutations (Figure 4-6H). Interestingly, a previous experimental study also showed that only small portion of cells can generate sustained p53 pulses with low amplitudes after treatment of Wip1 siRNA (163). Our simulations indicate that while these mutated cells were unable to generate sustained pulses of p53 after γ-irradiation at the cell population level (deterministic simulation), noise can often induce sustained rhythms at the single cell level (stochastic simulation).

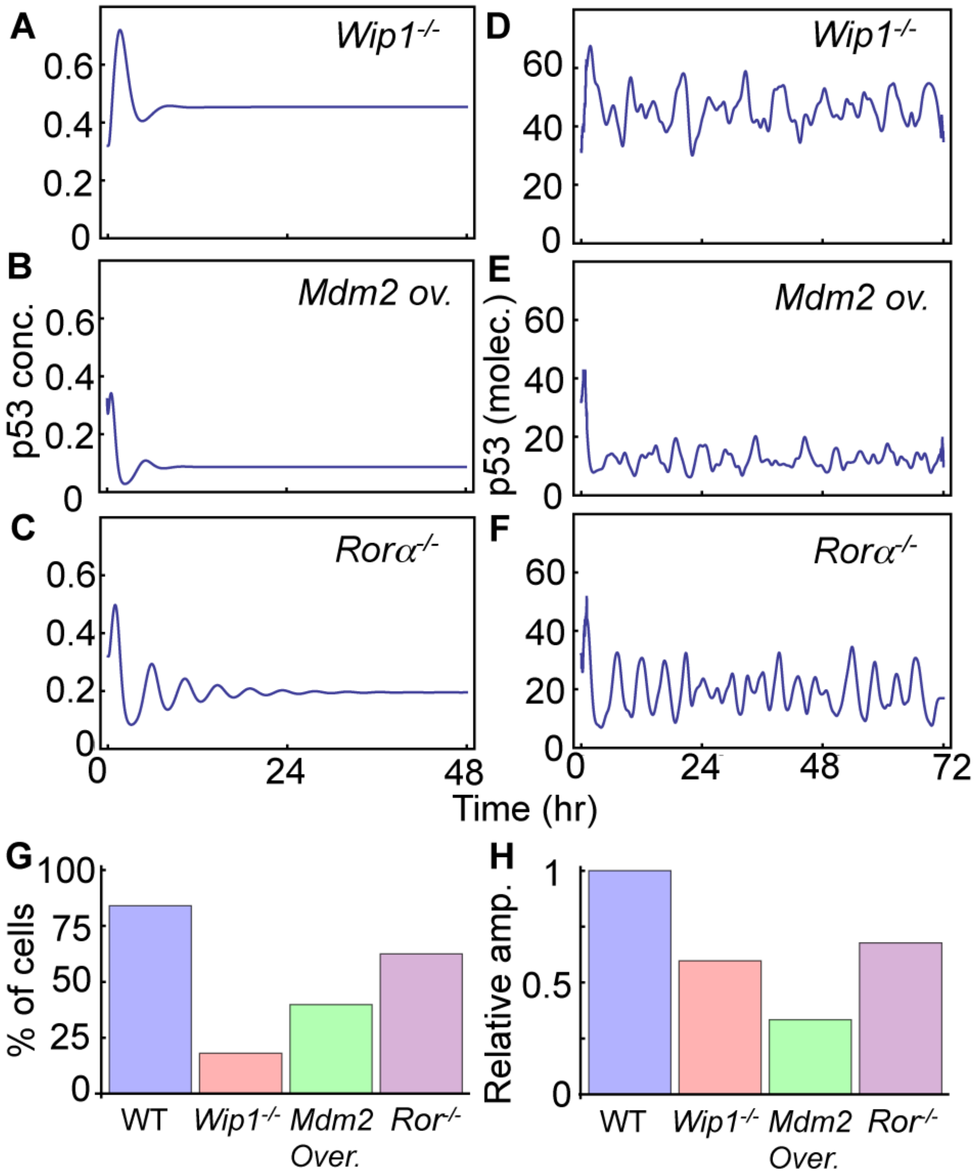

Figure 4-6. Simulations of knockout or overexpression mutations.
(A-C) Deterministic simulations of *Wip1*$^{-/-}$, *Mdm2* overexpression (10 fold), and *Rorα*$^{-/-}$ showed dampened p53 pulses after 10Gy irradiation. (D-F) Stochasticity or intrinsic noise was often able to induce sustained p53 pulses even with these mutations after 10Gy irradiation. (G) Probability of sustained p53 pulse occurrence with noise for 500 cells in response to 10Gy irradiation. (H) Mean relative amplitude of p53 pulses of oscillating cells among 500 cells (normalized to average relative amplitudes in WT cells).

4.3.2 Common characteristics between the p53 model and Type II neurons

We noticed that the p53 regulatory system in cells behaves like an excitatory system similar to neurons. That is, while p53 levels remain at a steady state in the absence of

DNA damage, transient DNA damage can induce spontaneous pulses of p53 (161). Moreover, severe DNA damage induced by γ-irradiation yields a series of p53 pulses with a small variation in period, but a large variation in amplitude (Figure 4-5D-E) (26). Interestingly, these are also common features of type II neurons, which are also known as resonator neurons due to their preferred frequency of spiking (205). When an external current greater than a certain threshold is applied, type II neurons begin generating spikes with a narrow range of frequencies, regardless of the strength of the external stimuli, while other types of neurons (e.g. type I neurons) yield spikes with a wide range of frequencies depending on the strength of the external currents (205-207).

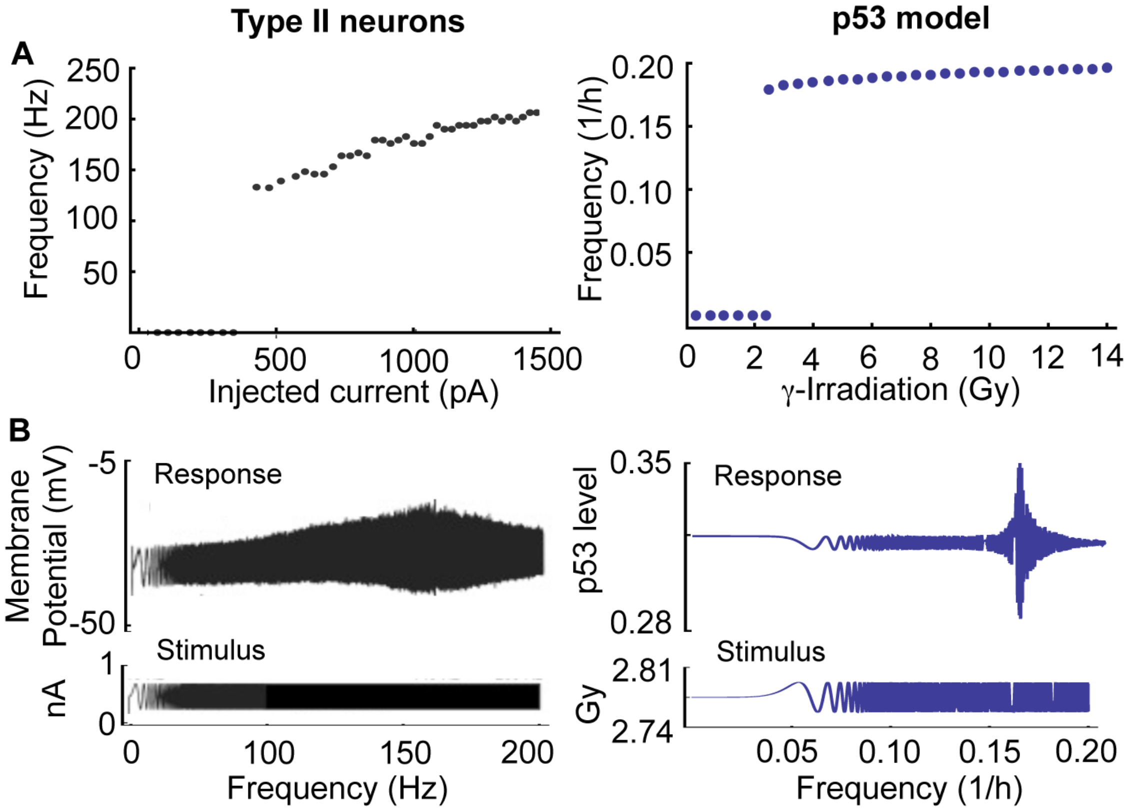

Figure 4-7. p53 pulses in the model and spikes of type II neurons show similar responses to the external stimuli with different strengths (A) and with varying frequencies (B).
(A) Both oscillating spikes in type II neurons and sustained p53 pulses of model have a non-zero lower bound for frequencies and a narrow range of frequencies in response to different strengths of constant external stimuli. (B) Both membrane potential in type II neurons and p53 in the model respond sensitively to oscillating stimuli with a specific frequency. The figures of type II neurons are reproduced with Figures 7.3 and 7.17 in (208) by permission from The MIT Press

We further explored whether pulses of p53 in cells and spikes of type II neurons have more common features in response to external stimuli. Given external constant currents with different strengths, type II neurons have a non-zero lower bound for frequency and a narrow range of frequency variation (Figure 4-7A) (205, 207). Similarly, p53 pulses also have a non-zero lower bound for their frequency and a narrow range of frequency variation for different strengths of γ-irradiation in the model (Figure 4-7A). When an oscillating current, as opposed to a constant current, with varying frequency and low amplitude is injected, type II neurons also show an interesting response. They respond sensitively to the injected current with a specific frequency (205, 207) (Figure 4-7B). We tested whether p53 pulses would respond in a similar way to low amplitude γ-irradiation with varying frequency, $2.78 + 0.02 Sin(0.1\pi t^{1.15})$ Gy. Surprisingly, p53 levels showed a sensitive response to irradiation with a specific frequency (~0.16/hr) similar to type II neurons (Figure 4-7B). Mathematically type II neurons are characterized by a Hopf bifurcation when the level of external current is varied. Indeed, our p53 model also shows a supercritical Hopf bifurcation when the strength of γ-irradiation is changed.

4.3.3 A potential coupling mechanism of p53 pulses among neighboring cells

We have shown that both p53 pulses in DNA-damaged cells and spikes of type II neurons have the characteristics of resonators. This raises the question of why DNA-damaged cells act as resonators or, in other words, what is the benefit of behaving as a resonator when p53 pulses are generated. One of the distinct characteristics of resonator neurons is that they can synchronize rhythms in purely excitatory networks, while integrator neurons cannot synchronize their rhythms (209). This feature of the resonator neuron leads to the hypothesis that like resonator neurons, DNA-damaged cells are designed to synchronize p53 pulses.

Before exploring this hypothesis, we first examined whether there exists a coupling signal among cells similar to excitatory neurotransmitters among neurons. Interestingly, recent studies have found that neighboring cells communicate with each other after γ-irradiation through the ‘radiation induced bystander effect (RIBE) (188). RIBE is characterized by DNA damage in *un-irradiated* cells that is induced by molecular signals produced by their neighboring *irradiated* cells. While many molecular signals involving RIBE have been proposed, a recent study identified Cytochrome-c (cyt-c) as one of main signals inducing RIBE. Specifically, γ-irradiation induces the p53 dependent release of mitochondrial cyt-c, which enters *un-irradiated* neighboring cells through gap junctions (210) and diffusion (174) (Figure 4-8A). The released cytochrome-c then causes DSBs or DNA damage that activates p53 in the *un-irradiated* neighboring cells (Figure 4-8A) (211). In this way, cyt-c can act as an excitatory neurotransmitter and provide a potential mechanism that couples p53 pulses of neighboring cells (Figure 4-8B). Similar couplings via diffusion of molecular signals have been identified in other biological oscillators, including the coupling of circadian rhythms of clock gene expressions via diffusion of VIP signal (212, 213) and coupling of *Dictostelium* cAMP oscillations via the diffusion of cAMP signal (179).

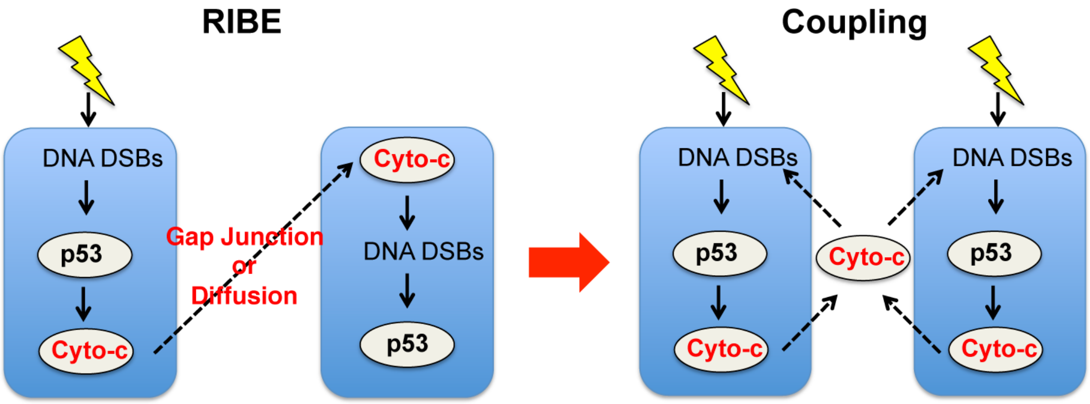

Figure 4-8. Radiation-induced bystander effects (RIBE) can be a potential mechanism that couples p53 pulses.
γ-irradiation stimulates the p53-dependent release of cytochrome-c. The released cytochrome-c can stimulate the upper signal of p53 pathway of neighboring cells. This can be a potential excitatory coupling mechanism of p53 pulses among neighboring cells in response to γ-irradiation.

Given that previous studies of RIBE have explored only the effect on *un-irradiated* cells neighboring *irradiated* cells, the question remains whether the RIBE can activate p53 even in *irradiated* cells. Regarding this question, a recent study has shown the promising result that DSBs induced by RIBE, persist for a longer period than those induced by direct irradiation (214). This suggests that RIBE has a distinct pathway for the activation of p53 different from that of direct γ-irradiation. Thus, DSBs induced by cyt-c could activate p53 even in *irradiated* neighboring cells and provide a potential coupling mechanism, although the strength of coupling may be weak (Figure 4-8B).

4.3.4 Coupling enhances the sustainability of p53 pulses

To determine whether coupling via cyt-c can induce synchronization of p53 pulses among irradiated cells, we extended the current model to include cyt-c. In the model, cyt-c is produced in proportion to activated p53 in each cell after γ-irradiation (see Table C-3 for the description of parameters).

$$\frac{d[Cyt-c_{-i}]}{dt} = \beta_c \frac{[p53_{active-i}]^{n_c}}{[p53_{active-i}]^{n_c} + T_c^{n_c}} - \alpha_c [Cyt-c_{-i}]$$

in which, sub-index *i* represents the i_{th} cell. Total cyt-c from all neighboring cells, representing the exogenous concentration of cyt-c, then activates ATM in all neighboring cells.

$$\beta_s \frac{IR^{N_g}}{T_g + IR^{N_g}} \longrightarrow \beta_s \frac{(IR + \frac{\beta_{cf}}{n}\sum_{i=1}^{n} Cyt-c_{-i})^{N_g}}{T_g + (IR + \frac{\beta_{cf}}{n}\sum_{i=1}^{n} Cyt-c_{-i})^{N_g}}$$

in which, the average of cyt-c produced in each cell represent exogenous concentration of cyt-c. Here, we assumed that cyt-c, released from each cell by 3Gy irradiation, induces DSBs of neighboring cells similar to those induced by ~0.5 Gy irradiation, matching experimental data (27). Although DSBs induced by cyt-c were significantly less than those induced by 3Gy γ-irradiation, the coupling via cyt-c can synchronize p53 pulses of four neighboring cells, all of which initially had different phases (Figure 4-9A). Here, we considered four cells since coupling through diffusion or gap junctions would work only locally.

This result leads to the question of what might be the potential benefit of synchronization through the coupling. Because previous studies have found that synchronization through a coupling can enhance rhythm occurrence in circadian clocks and *Dictostelium* cAMP oscillators (22, 23, 103, 179), we tested whether the coupling can help to sustain p53 pulses.

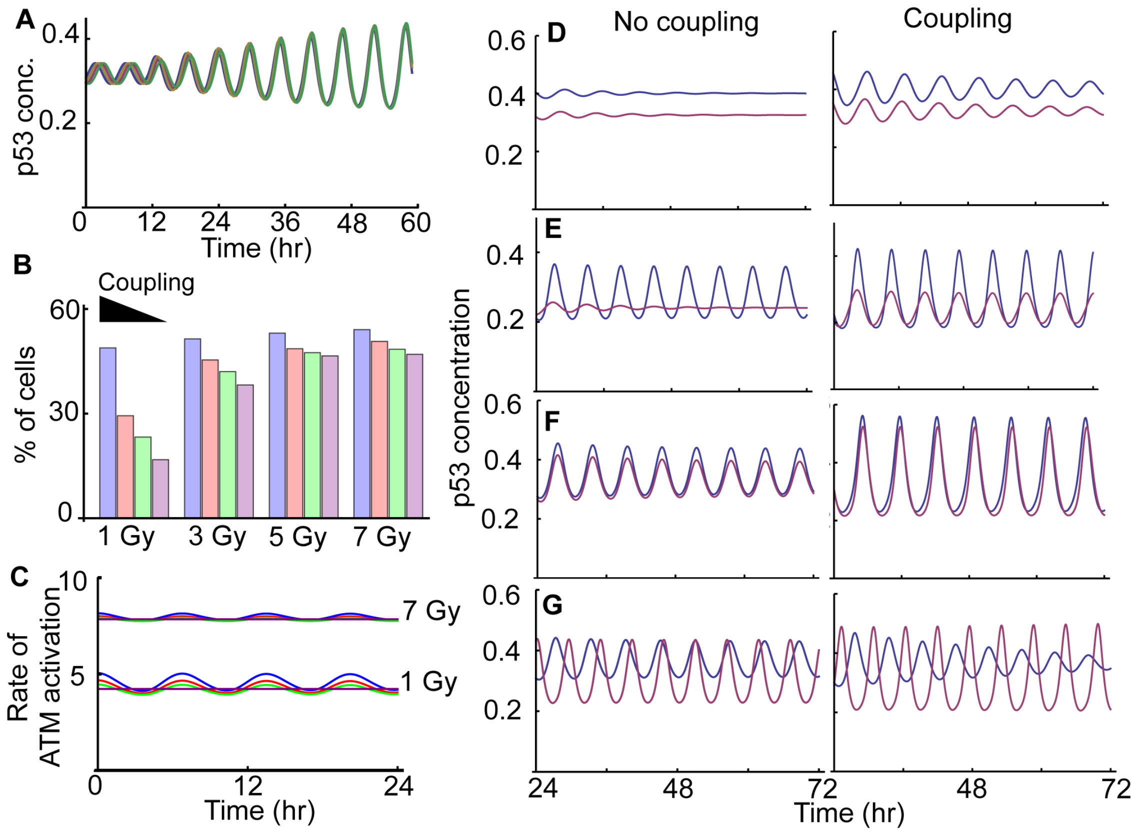

Figure 4-9. Coupling enhances the sustainability of p53 pulses.
(A) After 3 Gy irradiation, coupling through cyt-c synchronizes p53 pulses with different initial phases of four cells. (B) As the strength of coupling becomes stronger, the fraction of cells that can sustain p53 pulses increases. Here, a heterogeneous mixture of 4000 cells is considered, with coupling of four randomly selected cells. p53 pulses were simulated for 72 hours after γ-irradiation with different strengths (1, 3, 5 and 7 Gy). For the different strength of coupling, 6, 3, 1.5 and 0 were used as $\beta_{cu,}$, a coupling strength parameter (Table C-3). (C) The effect of the cyt-c signal on ATM activation becomes weaker as the strength of γ-irradiation becomes stronger. Here, β_{cf} = 6 (blue), 3 (red), 1.5 (green) and 0 (purple). (D-G). Comparison of p53 pulses in two neighboring cells without coupling and with coupling in the presence of 1Gy irradiation. Here, two neighboring cells were considered.

The sustainability of p53 pulses for 3 days in 4000 heterogeneous cells was simulated in response to different strengths of γ-irradiation. Here, parameters of every cell were perturbed by multiplying random numbers e^X ($X \sim N(0, 0.2)$) as we did previously. To test the role of coupling, we randomly coupled every four cells in the 4000 cells. Simulations showed a clear role of the coupling in sustaining p53 pulses after γ-irradiation. That is, as the strength of coupling becomes stronger, more cells can maintain their p53 pulses (Figure 4-9B). For instance, while two cells are unable to generate sustained p53 pulses, coupling can restore their pulses (Figure 4-9D). This is also seen when only one of two cells oscillates (Figure 4-9E). Moreover, when both cells can sustain p53 pulses with a similar period, coupling increases the amplitude of rhythms (Figure 4-9F). In this way, coupling enhances the occurrence of p53 rhythms, but the effect of coupling is reduced as the strength of γ-irradiation increases (Figure 4-9B). This is because ATM activation induced by coupling is too small to compete with activation induced by strong γ-irradiation (Figure 4-9C). Moreover, when both cells sustain p53 pulses with significantly different periods, coupling cannot synchronize p53 pulses and increase the amplitude, but instead coupling reduces the period difference (Figure 4-9G), indicating that the coupling could also play a role in tight regulation of the periods of p53 pulses. Taken together, the coupling of cells via cyt-c can synchronize p53 pulses and enhance the sustainability of the pulses. The effect of coupling becomes even more remarkable when the strength of γ-irradiation becomes weaker and the heterogeneity of periods is smaller.

4.4 Discussion

To explore potential mechanisms that sustain p53 pulses in response to γ-irradiation, we developed a new mathematical model by modifying and extending Batchelor's model (163). While most mathematical models of p53 pulses are based on a single negative feedback loop between p53 and Mdm2 (167-172), recent experimental studies have found that additional negative feedback loops are required to generate p53 pulses. While Batchelor's model includes these newly identified negative feedback loops, it also includes explicit time delays (~1hr), which might be biologically unrealistic and often induce oscillation in systems whose structures are not likely to produce rhythms naturally (2, 189). Thus, rather than including the explicit time delays, we included the intermediate steps associated with Wip1 and Mdm2 production (Figure 4-1A). During this process, we found that a network structure consisting of three interlocked negative feedback loops, could not sustain p53 pulses over a wide range of conditions (Figure 4-1B and D). Interestingly, when we added a recently identified positive feedback loop between p53 and Rorα, both sustainability and amplitude of the p53 pulses were significantly improved, which is consistent with previous studies showing the potential role of additional positive feedback loops (2, 170, 178) (Figure 4-1D and E). Furthermore, our new model with the additional positive feedback loop was able to reproduce many key features of p53 pulses (Figure 4-4 and Figure 4-5). Our model proposes a new network structure, which can generate more robust p53 pulses: three interlocked negative feedback loops with an additional positive feedback loop. Moreover, when we included noise through stochastic simulations, we found that noise can often prevent p53 pulses from dampening even after mutations of essential species of p53 oscillatory systems, such as Wip1$^{-/-}$, SNP309, and Rorα$^{-/-}$ (Figure 4-6D-F), although the overall chances of sustained p53 pulse occurrence are significantly reduced (Figure 4-6G). Finally, we found that when p53 pulses in neighboring cells are coupled via cyt-c signals (Figure 4-8), p53 pulses are synchronized and their sustainability is enhanced unless the difference of periods were significant (Figure 4-9). The coupling effect becomes more significant as the strength of γ-irradiation becomes weaker (Figure 4-9B). Interestingly, a similar influence of coupling has been found in other biological oscillatory systems, such as circadian clocks and cAMP oscillators (23, 103, 179). In summary, we found three potential mechanisms that enhance the sustainability of p53 pulses: 1) an additional positive feedback loop between p53 and Rorα, 2) intrinsic noise, and 3) the intercellular coupling through cyt-c.

Biological oscillatory systems can be categorized according to the driving sources of their rhythms. One category consists of endogenous oscillators (e.g. circadian clocks and sino-atrial node), which can generate rhythms without external stimuli (15, 215). The p53 regulatory system belongs to the other category, exogenous oscillators, which require external stimuli to sustain oscillations. One of the most widely studied exogenous oscillators in cell biology is the neuron. Depending on their responses to external stimuli, most neurons can succinctly be classified as type I or type II neurons (205-207). Type I neurons behave like an integrator, which accumulates various external current inputs that generate rhythms. Type II neurons behave like a resonator, which generate rhythms when an external current with a specific frequency is applied. We found that DNA-damaged cells behave like type II neurons (Figure 4-7). The fact that type II neurons easily synchronize their spikes when they are coupled through excitatory signals (209) led to the question of whether neighboring cells also have a coupling mechanism that synchronizes p53 pulses. Indeed, a recent experimental study found a potential coupling signal (cyt-c) for p53 pulses among neighboring cells (Figure 4-8) (27). When we included this intercellular coupling in the model, we found that coupling through cyt-c can synchronize p53 pulses unless the difference in the periods of coupled cells is significant (Figure 4-9). Moreover, the coupling significantly enhances the sustainability of p53 pulses (Figure 4-9B).

Regarding the synchronization of p53 pulses, a high correlation between the distance among cells and their phase relationship would be an indicator of the presence of local coupling that synchronizes p53 pulses of neighboring cells. Unfortunately, most previous studies measured only the time courses of p53 pulses in individual cells without keeping track of spatial information (26, 162, 163). We did, however, find one set of experimental data that recorded the time courses of p53 pulses among five neighboring cells (26). Interestingly, when we analyzed this data, we found that the five cells could be categorized into two groups, each with the same peak timing of p53 pulses. This indicates that closer cells may have more similar phases or that they may synchronize p53 pulses. However, to derive a significant conclusion about the relationship between p53 phases and distance among cells, a data set much larger than five cells is required. Another interesting experiment would be to test whether cyt-c can act as a coupling mechanism of p53 pulses. For this, we first need to study whether cyt-c increases DNA damage even in *irradiated* neighboring cells since cyt-c induced DNA damage has been studied in only *un-irradiated* neighboring cells (Figure 4-8). If cyt-c could induce DNA damage even in *irradiated* neighboring cells, the next step would be to test whether cyt-c can synchronize p53 pulses and enhance their sustainability. The direct test for this would involve studying the effect of the inhibition of cyt-c via cyclosporine A on the p53 pulses. More specifically, future research could test whether the inhibition of cyt-c yields a wider distribution of phases and periods of p53 pulses and lower chance of sustained p53 pulses occurrence. Moreover, additional future modeling could consider a spatio-temporal modeling approach to study the role of cyt-c in depth (216).

We also found that Rorα may be an essential component in sustaining γ-triggered p53 pulses. That is, sustainability and amplitudes of p53 pulses are significantly reduced in Rorα$^{-/-}$ cells (Figure 4-1D-E and Figure 4-6G-H), although noise can often induce sustained p53 pulses even with Rorα$^{-/-}$ (Figure 4-6F). It would be a worthwhile future experiment to test the role of Rorα on γ-triggered p53 pulses by knocking out Rorα. Interestingly, Rorα is one of core circadian (~24hr) clock genes, whose gene expression shows 24hr periodic rhythms (217). Since p53 also exhibits circadian rhythms at both the mRNA and protein level, various candidate pathways underlying p53 circadian rhythms have been proposed, such as c-myc (218, 219). Our study proposed another potential mechanism that generates the circadian rhythms of p53 protein: positive feedback between p53 and Rorα, which could be an important target for chronotherapy. This hypothesis can be tested by considering the effect of Rorα$^{-/-}$ on circadian rhythms of p53. A previous study suggested that noise in protein production rate with a slow correlation time (10~20h) could be a reason for the variability observed in γ-triggered p53 pulses (26). Circadian rhythms of Rorα gene expression or p53 gene expression could be the source of the slowly varying noise in the protein production rates, causing a large variability in the amplitude of p53 pulses.

Chapter 5 Conclusion

This dissertation developed theorems and mathematical models to approach two fundamental problems in cellular rhythms: identifying the biochemical network structure underlying biological clocks and understanding the functions of these biochemical networks.

In chapter 2, we studied the existence and uniqueness of the mathematical models of biological clocks given oscillating timecourses. For this, we considered a simple, but very general form of mathematical model, which is frequently used to describe molecular biological clocks:

$$\frac{dr}{dt} = f(s) - g(r) \tag{5.1}$$

First, we proved that if there exists a model with the form (5.1), which has solutions matching two given oscillating timecourses $r(t)$ and $s(t)$, then the model is unique in most cases. That is, this theorem indicates that oscillating timecourses can alone determine the biochemical rates of models with the form (5.1). Furthermore, we proved a necessary condition of oscillating timecourses $r(t)$ and $s(t)$ in order for them to be solutions of the models with the form (5.1). If this condition is invalidated, the model having solutions $r(t)$ and $s(t)$ does not exist, which in turn means that two species, r and s have no biochemical interaction. This theorem provides a simple algorithm that identifies unrelated species in biochemical network based on their timecourses:

- Step 1. Given two oscillating timecourses, $r(t)$ and $s(t)$, find $\hat{r}(t)$ and $\hat{s}(t)$, which map one time point to another time point where $r(t)$ and $s(t)$ have the same value, respectively.
- Step 2. Find the composite of $\hat{r}(t)$ and $\hat{s}(t)$: $\phi(t) := \hat{s}(\hat{r}(t))$. Check if $\phi^n(t)$ has a fixed point t for any n.
- Step 3. If there exists a fixed point, which does not satisfy the degenerative condition, $r(t)$ and $s(t)$ cannot be solutions of any model with the form (5.1), indicating that two species r and s have no biochemical interactions.

Since this new algorithm is the very first approach that uses a fixed point criteria to reveal the network structure, more study is needed to apply this algorithm to real data. In particular, the current theory assumes that timecourse data does not have any noise. Since all biological data include noise, future work should test whether this algorithm is stable in the presence of noise. Furthermore, the incorporation of a statistical method, which filters the noise in timecourse data, to the algorithm would be another interesting future project.

In chapter 2, we also considered the existence and uniqueness of models with forms, which are different from (5.1):

$$\frac{df(r)}{dt} = s + g(r), \tag{5.2}$$

and

$$\frac{dr}{dt} = f(r)s - g(r). \tag{5.3}$$

We found that models with these forms have uniqueness and existence over a broader class of timecourses than models with the form (5.1). Interestingly, we also found that most results about the existence and uniqueness of models with these forms were also obtained by studying the fixed points of an iterating map $\phi^n(t)$, indicating the importance and general applicability of map $\phi^n(t)$. Given the results of our work here, several fruitful lines of research could be pursued. First, given the importance of fixed points of the iterating map $\phi^n(t)$, future work should consider the method to more easily determine the fixed points. Second, while the present study considers only models that consist of two species r and s, future work could consider more general models that consist of more than two species. This can lead to a new algorithm that detects biochemical interactions among multiple species. Finally, the algorithm developed in chapter 2 is not limited to only biochemical networks, and so it would be interesting to apply it to detect the structures of other types of complex networks with oscillating outputs (e.g. neuronal networks, ecological systems, climate systems or social networks).

In chapter 3, we developed the most detailed mathematical model of the mammalian circadian clock to date. This model matches various experimental data including time courses and relative concentrations of key transcripts and proteins, mutation phenotypes, and the effects of changes in gene dosage. In particular, the model accurately predicts the phenotype of known mutations of genes in the circadian clock, which was not achieved in previous models. Furthermore, for the accuracy of the model, mass action kinetics was used to explicitly describe dynamics of all possible complexes of monomers. With the simulation of this model, we proposed mechanisms that generate circadian rhythms and maintain 24-hr period over a wide range of conditions:

- Proper stoichiometric balance between activators (BMAL–CLOCK/NPAS2) and repressors (PER1–2/ CRY1–2) of a core negative feedback loop in the circadian clock,
- Tight binding between activators and repressors,
- The NNF (negative-negative feedback loops) structure, in which repressors and activators suppress their own transcription via core negative feedback loop and additional negative feedback loop, respectively,
- Longer half-life of activators than repressors.

These mechanisms synergistically generate rhythms with a nearly constant period even with significant perturbations in transcriptions. The range of the stoichiometry where the rhythms occur widens as binding between activators and repressors tightens. Moreover, to maintain stoichiometry in the range where rhythms occur, the NNF structure allows the regulation of the levels of both activators and repressors. When an additional feedback loop regulates the expression of activators on a slower timescale (i.e. a longer half-life of activators than repressors), the core negative feedback function of rhythm generation is not disrupted by the additional negative feedback loop, which enhances rhythm generation. These mechanisms were also validated by analysis of a simplified mathematical model of the mammalian circadian clock, indicating the generality of these mechanisms.

While the mammalian circadian clock model revealed these mechanisms for robust circadian rhythms, we found that these mechanisms are commonly used by other multicellular organisms (e.g. flies) (53, 54, 64). In the case of unicellular organisms (e.g. *Neurospora*), however, these mechanisms do not appear to be used in generating circadian rhythms (133, 220). This raises the interesting question of why different organisms use different designs for executing the same function of circadian rhythm generation. One hypothesis is that the design of circadian clocks in multicellular organisms might be better at synchronizing rhythms with neighboring cells than the design of circadian clocks in unicellular organisms. To test this hypothesis, the extension of the current single cell model to coupled multi-cell models would be valuable future work.

In chapter 3, we also studied how pharmacological inhibition of CK1δ/ε can modulate the phase of mammalian circadian clocks under a light-dark cycle by using the detailed mathematical model of the mammalian circadian clock. To achieve accurate predictions of the model, experimentally measured PK/PD data of CK1δ/ε inhibitor (PF-670462) were incorporated to the model. The model predicts that chronic inhibition of CK1δ/ε under a LD cycle can yield a constant stable delay of circadian phase depending on dosing amount, dosing timing, day lengths and intrinsic period of circadian rhythms. That is, the model predicts that a constant stable delay is more likely to occur as dosing occurs earlier in the day or/and day length becomes shorter. This work shows how mathematical modeling can be used to determine a dosing strategy of chronic CK1δ/ε inhibition and to estimate the effect of environmental condition on dosing. Furthermore, our work provides a non-traditional approach to stable modulation of the phase circadian rhythms, which can be used to treat the misalignment of circadian clocks (e.g. advanced sleep phase disorder).

This work here indicates that our mathematical model can be used to study the effect of inhibition of the other kinases involving circadian clocks. In particular, an important kinase of circadian clocks, GSK3β could be the focus of interesting future work. An inhibitor of GSK3β, Lithium, also delays circadian phase in a manner similar to the CK1δ/ε inhibitor. Interestingly, the modulation of circadian rhythms induced by Lithium has been proposed to explain the effect of chronic dosing of Lithium on treatment of mood disorders, such as a bipolar disorder. Future work could consider the incorporation of Lithium into our detailed mathematical model. The model could then be used to find an optimized dosing strategy of chronic dosing of Lithium to treat mood disorders.

In chapter 4, we developed a mathematical model of the p53 pulse regulatory system to investigate molecular mechanisms that enhance sustainability of p53 pulses in response to DNA damage. In our development of the mathematical model, we found that the currently known biochemical network structure of the p53 pulse regulatory system, namely three inter-locked negative feedback loops, cannot on their own sustain p53 pulses over a wide range of conditions. We found that the addition of a recently identified positive feedback loop between p53 and Rorα to the original structure significantly improves both sustainability and amplitude of the p53 pulses. This indicates that Rorα is an important component of p53 pulse regulatory system. Interestingly, Rorα is one of core circadian clock genes, which generate and control circadian rhythms in the master circadian clock. Since the level of Rorα also shows circadian rhythms, Rorα can induce circadian rhythms of p53 level via the positive feedback loop between p53 and Rorα. If Rorα were a key link between the p53 regulatory system and circadian clocks, it would be an important target for chronotherapy, which focuses on the relationship between dosing timing and dosing effects on cancer. To explore the Rorα induced circadian rhythms of p53, linking our two models, the circadian clock model and p53 model can be considered for future work.

By simulating the model with the Gillespie algorithm, we also found that intrinsic noise can help sustain p53 pulses in response to the mutation of key species of the p53 pulse regulatory system. We also found that DNA damaged cells behave like type II neurons, which act as resonators. The fact that type II neurons easily synchronize their rhythms when they are coupled led to the question of whether neighboring cells also synchronize p53 pulses. When we included a recently identified potential coupling signal, cyt-c, in the model, indeed, the coupling synchronizes p53 pulses and significantly improves the sustainability of p53 pulses. Future work should look for similarities between neuronal oscillations and other types of externally induced cellular rhythms. Since neurons are the most widely studied biological oscillators, the underlying mechanisms of their dynamical behaviors are relatively well known. Therefore, the identification of similarities between biological clocks with neuronal oscillators could help unravel the mysteries of complex functions in biological clocks, such as the functions we found regarding the synchronization of p53 pulses.

Through the studies described in chapter 2 through 4, this dissertation demonstrates how mathematical theory and modeling can be used to illuminate biochemical networks and core dynamics of biological clocks by integrating experimental data. The revealed core mechanisms that generate cellular rhythm can be used to diagnose the cause of disrupted cellular rhythms and restore the disrupted rhythms. Furthermore, our work also shows the practical applicability of mathematical modeling to test the drug effects on cellular rhythms systemically under various environmental conditions. Given the significant impact of misaligned or disrupted rhythms on various diseases including cancer, insomnia, mood disorders, and diabetes, we believe our studies can contribute to improving human health significantly.

Appendices

Appendix A Description of the detailed model of mammalian circadian clocks

A.1 Variables

Table A-1. The variables used in the detailed model of circadian clock.

Name	**Symbol**
The concentration of *Per1* mRNA in the nucleus/ cytoplasm	MnPo/McPo
The concentration of *Per2* mRNA in the nucleus/ cytoplasm	MnPt/McPt
The concentration of *Cry1* mRNA in the nucleus/ cytoplasm	MnRo/McRo
The concentration of *Cry2* mRNA in the nucleus/ cytoplasm	MnRt/McRt
The concentration of *Bmals* mRNA in the nucleus/ cytoplasm	MnB/McB
The concentration of *Npas2* mRNA in the nucleus/ cytoplasm	MnNp/McNp
The concentration of *Rev-erbs* mRNA in the nucleus/cytoplasm	MnRev/McRev
The concentration of BMALs protein in the cytoplasm	B
The concentration of CLOCK/NPAS2 protein in the cytoplasm	Cl
The concentration of unphosphorylated BMALs-CLOCK/NPAS2	BC
The concentration of unphosphorylated REV-ERBs in the nucleus/cytoplasm	revn/cyrev
The concentration of unphosphorylated REV-ERBs bound with GSK3β in the nucleus/cytoplasm	revng/cyrevg
The concentration of phosphorylated REV-ERBs bound with GSK3β in the nucleus/cytoplasm	revngp/cyrevgp
The concentration of phosphorylated REV-ERBs in the nucleus/cytoplasm	revnp/cyrevp
The probability of the *per1*, *per2*, and *cry1* E-box being activated	G
The probability of the *per1*, *per2*, and *cry1* E-box being repressed	GR
The probability of the *cry2* E-box being activated	Gc
The probability of the *cry2* E-box being repressed	GcR
The probability of the *rev-erbs* E-box being activated	Gr
The probability of the *rev-erbs* E-box being repressed	GrR
The probability of the *npas2* and *cry1* RORE being activated	GB
The probability of the *npas2* and *cry1* RORE being repressed	GBR
The probability of the *Bmals* RORE being activated	GBb
The probability of the *Bmals* RORE being repressed	GBRb
The activity of GSK3β	gto
The strength of transcription drive of light	ltn

Note the protein complexes are separately listed in Table A-2.

Table A-2. The variables of protein complexes used in the detailed model of circadian clock.

Index	j PER	k CRY	l Kinase	m Location	n BMALs-CLK
0	No PER bound	No CRY bound	No Kinases bound	Cytoplasm	No BMALs-CLK bound
1	PER1	CRY1	CKI	Nucleus	BMALs^P-CLK^P
2	PER1^P by CKI	CRY2	GSK3		
3	PER2		CKI&GSK3		
4	PER2^P by CKI				
5	PER2^P by GSK3				
6	PER2^P by both GSK3 and CKI				

Each complex is encoded as x[j][k][l][m][n], where j, k, l, m and n refer to the proteins that are present in the complex, or the location of the complex. We also assume that when BMALs-CLK is phosphorylated when in complex. "^{P}" represents "phosphorylated".

A.2 Parameters

Table A-3. Parameters of the detailed model of circadian clock.

Parameter Description	Symbol	Value	Reference
Transcription rate constant for *Per1*	trPo	25.92	
Transcription rate constant for of *Per2*	trPt	44.85	
Transcription rate constant for of *Cry1*	trRo	23.07	
Transcription rate constant for *Cry2*	trRt	39.94	
Transcription rate constant for *Bmal* (1)	trB	46.10	
Transcription rate constant for *Npas2* (1)	trNp	0.33	
Transcription rate constant for *Rev-Erbs*	trRev	102.9	
Translation rate constant for PER1 and PER2	tlp	1.81	
Translation rate constant for CRY1 and CRY2	tlr	5.038	
Translation rate constant for BMAL (1)	tlb	0.53	
Translation rate constant for CLOCK (1)	tlc	4.645	
Translation rate constant for NPAS2 (1)	tlnp	1.251	
Translation rate constant for REV-ERBs	tlrev	8.907	
Binding rate constant for PER2 to GSK3β (4)	agp	1.396	
Binding rate constant for REV-ERBs to GSK3β (4)	ag	0.162	
Unbinding rate constant for PER2/REV-ERBs to GSK3β (4)	dg	2.935	
Binding rate constant for PER1/2 to CKIε/δ	ac	0.046	
Unbinding rate constant for PER1/2 to CKIε/δ	dc	0.108	
Binding rate constant for PER1/2 to CRY1/2	ar	0.024	
Unbinding rate constant for PER1/2 to CRY1/2	dr	0.605	
Binding rate constant for PER1/2 to BMAL-CLOCK/NPAS2 in the nucleus (2)	bbin	6.926	(84)
Unbinding rate constant for PER1/2 to BMAL-CLOCK/NPAS2 in the nucleus (2)	unbbin	0.13	(84)
Binding rate constant for CRY1/2 to BMAL-CLOCK/NPAS2 in the nucleus (2)	cbbin	6.599	(84)
Unbinding rate constant for CRY1/2 to BMAL-CLOCK/NPAS2 in the nucleus (2)	uncbbin	0.304	(84)
Binding rate constant for BMAL to CLOCK/NPAS2 (1)	cbin	0.045	
Unbinding rate constant for BMAL to CLOCK/NPAS2 (1)	uncbin	7.272	
Binding rate constant for REV-ERBs to GSK3β (4)	ag	0.162	
Normalized binding rate constant for BMAL-CLOCK/NPAS2 to *Per1/2/Cry1* E-box (3)	bin	6.972	
Normalized unbinding rate constant for BMAL-CLOCK/NPAS2 to *Per1/2/Cry1* E-box (3)	unbin	0.255	
Normalized binding rate constant for BMAL-CLOCK/NPAS2 to *Cry2* E-box (3)	binc	0.280	
Normalized unbinding rate constant for BMAL-CLOCK/NPAS2 to *Cry2* E-box (3)	unbinc	0.009	
Normalized binding rate constant for BMAL-CLOCK/NPAS2 to *Rev-erbs* E-box (3)	binr	6.154	
Normalized unbinding rate constant for BMAL-CLOCK/NPAS2 to *Rev-erbs* E-box (3)	unbinr	2.91	

Normalized binding rate constant for REV-ERBs to *Bmal* RORE (1)	binrevb	0.006	
Normalized unbinding rate constant for REV-ERBs to *Bmal* RORE (1)	unbinrevb	5.305	
Normalized binding rate constant for REV-ERBs to *Cry1/Npas2* RORE (1)	binrev	0.012	
Normalized unbinding rate constant for REV-ERBs to *Cry1/Npas2* RORE (1)	unbinrev	10.97	
Rate constant for folding and nuclear export of *Per1/2, Cry1/2, Bmal* and *Npas2* mRNA	tmc	0.164	
Rate constant for folding and nuclear export of *Rev-Erbs* mRNA	tmcrev	9.263	
Nuclear localization rate constant for proteins bound to PER	nl	0.643	
Nuclear export rate constant for protein bound to PER	ne	0.026	
Nuclear localization rate constant for REV-ERBs as well as GSK3β if bound (4)	nlrev	9.637	
Nuclear export rate constant for REV-ERBs as well as GSK3β if bound (4)	nerve	0.015	
Nuclear localization rate constant for BMAL-CLOCK/NPAS2 (1)	nlbc	5.265	
Nuclear export rate constant for unbound kinases GSK3β and CKI (4)	lne	0.595	
Total CK1 concentration	Ct	57.61	(63)
Total GSK3β concentration (4)	Gt	79.73	
CKIε/δ phosphorylation rate constant for PER1	hoo	0.527	(63)
CKIε/δ phosphorylation rate constant for PER2	hto	2.456	(63)
Phosphorylation rate constant for BMAL-CLOCK/NPAS2 (1)	phos	0.291	
Increase rate of GSK3β activity (4)	trgto	0.644	
Decrease rate of GSK3β activity (4)	ugto	0.063	
Degradation rate constant for *Per1*	umPo	0.765	(106)
Degradation rate constant for *Per2*	umPt	0.589	(106)
Degradation rate constant for *Cry1*	umRo	0.403	(106)
Degradation rate constant for *Cry2*	umRt	0.456	(106)
Degradation rate constant for *Bmal* (1)	umB	0.795	(221)
Degradation rate constant for *Npas2* (1)	umNp	0.369	
Degradation rate constant for *Rev-Erbs*	umRev	1.51	(222)
Degradation rate constant for unphosphorylated PER	upu	0.07	(61)
Degradation rate constant for CKI phosphorylated PER	up	3.537	(120)
Degradation rate constant for CRY1	uro	0.174	(106)
Degradation rate constant for CRY2	urt	0.482	(84, 105)
Degradation rate constant for BMAL (1)	ub	0.019	(81)
Degradation rate constant for CLOCK/NPAS2 (1)	uc	0.025	(81)
Degradation rate constant for BMAL-CLOCK/NPAS2 (1)	ubc	0.349	(81)
Degradation rate constant for unphosphorylated REV-ERBs (4)	urev	1.649	(221)
Degradation rate constant for GSK3β phosphorylated REV-ERBs (4)	uprev	0.517	(221)
Ratio of cytoplasmic and nuclear compartment volume	Nf	3.351	(97)
Additional *Per1* transcription rate in the presence of light(5)	lono	0.206	(92)

Additional *Per2* transcription rate in the presence of light (5)	lont	0.396	(92)
Light level (5)	ltI	500	(90)
Rate of activation of pho (5)	lta	0.607	(90)
Light effect decrease (backward) rate (5)	ltb	0.013	(90)

References presenting experimental data on the parameter are indicated. If a parameter has been newly added to the previous model, a number is presented after the parameter description. This number corresponds to the list that describes the changes that were made to the model in the chapter 3.2.1. The units of time are hours, concentrations are expressed in nM and light is presented in Lux. As described in (28), binding rates to promoter elements are considered "normalized" because they are tracked by the probability that they are unbound. Further details can be found in (28).

A.3 Ordinary differential equations

(1) Promoter Activity

E-box

```
GR'=bin*(Sum[x[0][kk][0][1][1],(195)])*(1-G-GR)-unbin*GR

G'=bin*x[0][0][0][1][1]*(1-G-GR)-unbin*G

GrR'=binr*(Sum[x[0][kk][0][1][1],{kk,1,2}])*(1-Gr-GrR)-unbinr*GrR

Gr'=binr*x[0][0][0][1][1]*(1-Gr-GrR)-unbinr*Gr

GcR'=binc*(Sum[x[0][kk][0][1][1],{kk,1,2}])*(1-Gc-GcR)-unbinc*GcR

Gc'=binc*x[0][0][0][1][1]*(1-Gc-GcR)-unbinc*Gc
```

RORE

```
GBR'=binrev*(revn+revng+revngp+revnp)*GB-unbinrev*GBR

GB'=-binrev*(revn+revng+revngp+revnp)*GB+unbinrev*GBR

GBRb'=binrevb*(revn+revng+revngp+revnp)*GBb-unbinrevb*GBRb

GBb'=-binrevb*(revn+revng+revngp+revnp)*GBb+unbinrevb*GBRb
```

(2) Transcription

```
MnPo'=trPo*G-tmc*MnPo-umPo*MnPo

McPo'=tmc*MnPo-umPo*McPo

MnPt'=trPt*G-tmc*MnPt-umPt*MnPt

McPt'=tmc*MnPt-umPt*McPt

MnRt'=trRt*Gc-tmc*MnRt-umRt*MnRt

McRt'=tmc*MnRt-umRt*McRt

MnRev'=trRev*x[0][0][0][1][1]*Gr-tmcrev*MnRev-umRev*MnRev

McRev'=tmcrev*MnRev-umRev*McRev

MnRo'=trRo*G*GB-tmc*MnRo-umRo*MnRo
```

McRo'=tmc*MnRo-umRo*McRo

MnB'=trB*GBb-tmc*MnB-umB*MnB

McB'=tmc*MnB-umB*McB

MnNp'=trNp*GB- tmc*MnNp - umNp*MnNp

McNp'=tmc*MnNp-umNp*McNp

(3) Secondary Loop

B'=tlb*McB-cbin*B*Cl+uncbin*BC-ub*B

Cl'=tlnp*McNp+tlc-cbin*B*Cl+uncbin*BC-uc*Cl

BC'=cbin*B*Cl-uncbin*BC-phos*BC-ubc*BC

cyrev'=tlrev*McRev-(nlrev+urev)*cyrev-ag*cyrev*(x[0][0][2][0][0])+nerev*revn+dg*cyrevg

revn'=-(nerev+urev)*revn-ag*Nf*revn*(x[0][0][2][1][0])+nlrev*cyrev+dg*(revng)

cyrevg'=ag*cyrev*x[0][0][2][0][0]-(dg+gto+urev+nlrev)*cyrevg+nerev*revng

revng'=ag*Nf*revn*x[0][0][2][1][0]-(dg+gto+urev+nerev)*revng+nlrev*cyrevg

cyrevgp'=gto*cyrevg-(dg+uprev+nlrev)*cyrevgp+nerev*revngp

revngp'=gto*revng-(dg+uprev+nerev)*revngp+nlrev*cyrevgp

cyrevp'=dg*(cyrevgp)-(uprev+nlrev)*cyrevp+nerev*revnp

revnp'=dg*(revngp)-(uprev+nerev)*revnp+nlrev*cyrevp

(4) Translation

x[j][k][l][m][n]'=

If[(j=1)&&(k=0)&&(l=0)&&(m=0)&&(n=0),tlp*McPo,0]

+If[(j=3)&&(k=0)&&(l=0)&&(m=0)&&(n=0),tlp*McPt,0]

+If[(j=0)&&(k=1)&&(l=0)&&(m=0)&&(n=0),tlr*McRo,0]

+If[(j=0)&&(k=2)&&(l=0)&&(m=0)&&(n=0),tlr*McRt,0]

(5) Binding/Unbinding

PER-CRY

```
x[j][k][l][m][n]'=
If[(k=0)&&(n=0)&&((j=2)||(j=4)||(j=5)||(j=6)),-
ar*If[m=1,Nf,1]*Sum[x[0][kk][0][m][0],{kk,1,2}]*x[j][k][l][m][n]+dr*Sum[x[j][kk][l][m][n],{kk,1,
2}],0]+
If[(j=0)&&((k=1)||(k=2))&&(l=0)&&(n=0),-
ar*If[m=1,Nf,1]*x[j][k][l][m][n]*Sum[x[jj][0][ll][m][0],{jj,{2,4,5,6}},{ll,0,3}]+dr*Sum[x[jj][k][ll][m]
[n],{jj,{2,4,5,6}},{ll,0,3}],0]+
If[((j=2)||(j=4)||(j=5)||(j=6))&&((k=1)||(k=2))&&(n=0),ar*If[m=1,Nf,1]*x[0][k][0][m][n]*x[j][0][l][
m][0]-dr*x[j][k][l][m][n],0]+
If[(k=0)&&(n=1)&&((j=2)||(j=4)||(j=5)||(j=6))&&(m=1),-
ar*Nf*x[j][k][l][m][n]*Sum[x[0][kk][0][m][0],{kk,1,2}]+dr*Sum[x[j][kk][l][m][n],{kk,1,2}],0]+
If[(j=0)&&((k=1)||(k=2))&&(l=0)&&(m=1)&&(n=0),-
ar*Nf*x[j][k][l][m][n]*Sum[x[jj][0][ll][m][1],{jj,{2,4,5,6}},{ll,0,3}]+dr*Sum[x[jj][k][ll][m][1],{jj,{2,4
,5,6}},{ll,0,3}],0]+
If[((j=2)||(j=4)||(j=5)||(j=6))&&((k=1)||(k=2))&&(m=1)&&(n=1),ar*Nf*x[j][0][l][m][n]*x[0][k][0][
m][0]-dr*x[j][k][l][m][n],0]+
If[(k=0)&&(n=0)&&((j=2)||(j=4)||(j=5)||(j=6))&&(m=1),-
ar*Nf*x[j][k][l][m][n]*Sum[x[0][kk][0][m][1],{kk,1,2}]+dr*Sum[x[j][kk][l][m][1],{kk,1,2}],0]+
If[(j=0)&&((k=1)||(k=2))&&(l=0)&&(m=1)&&(n=1),-
ar*Nf*x[j][k][l][m][n]*Sum[x[jj][0][ll][m][0],{jj,{2,4,5,6}},{ll,0,3}]+dr*Sum[x[jj][k][ll][m][n],{jj,{2,4
,5,6}},{ll,0,3}],0]+
If[((j=2)||(j=4)||(j=5)||(j=6))&&((k=1)||(k=2))&&(m=1)&&(n=1),ar*Nf*x[j][0][l][m][0]*x[0][k][0][
m][1]-dr*x[j][k][l][m][n],0]+
If[(l=0)&&(j>0)&&(n=0),ac*If[m=1,Nf,1]*x[j][k][l][m][n]*x[0][0][1][m][0]+dc*x[j][k][1][m][n],0]
```

PER-CKI

```
x[j][k][l][m][n]'=
```

```
If[(j=0)&&(k=0)&&(l=1)&&(n=0),-
ac*If[m=1,Nf,1]*x[j][k][l][m][n]*Sum[x[jj][kk][0][m][0],{jj,1,6},{kk,0,2}]+dc*Sum[x[jj][kk][l][m][
0],{jj,1,6},{kk,0,2}],0]+
If[(j>0)&&(l=1)&&(n=0),ac*If[m=1,Nf,1]*x[0][0][1][m][0]*x[j][k][0][m][n]-dc*x[j][k][l][m][n],0]+
If[(l=0)&&(j>0)&&(m=1)&&(n=1),-
ac*Nf*x[j][k][l][m][n]*x[0][0][1][m][0]+dc*x[j][k][1][m][n],0]+
If[(j=0)&&(k=0)&&(l=1)&&(m=1)&&(n=0),-
ac*Nf*x[j][k][l][m][n]*Sum[x[jj][kk][0][m][1],{jj,1,6},{kk,0,2}]+dc*Sum[x[jj][kk][l][m][1],{jj,1,6},{
kk,0,2}],0]+
If[(j>0)&&(l=1)&&(m=1)&&(n=1),ac*Nf*x[0][0][1][m][0]*x[j][k][0][m][n]-dc*x[j][k][l][m][n],0]+
If[(j>2)&&(l=2)&&(n=0),-
ac*If[m=1,Nf,1]*x[j][k][l][m][n]*x[0][0][1][m][0]+dc*x[j][k][3][m][n],0]+
If[(j=0)&&(k=0)&&(l=1)&&(n=0),-
ac*If[m=1,Nf,1]*x[j][k][l][m][n]*Sum[x[jj][kk][2][m][0],{jj,3,6},{kk,0,2}]+dc*Sum[x[jj][kk][3][m][
0],{jj,3,6},{kk,0,2}],0]+
If[(j>2)&&(l=3)&&(n=0),ac*If[m=1,Nf,1]*x[0][0][1][m][0]*x[j][k][2][m][n]-dc*x[j][k][l][m][n],0]+
If[(j>2)&&(l=2)&&(m=1)&&(n=1),-
ac*Nf*x[j][k][l][m][n]*x[0][0][1][m][0]+dc*x[j][k][3][m][n],0]+
If[(j=0)&&(k=0)&&(l=1)&&(m=1)&&(n=0),-
ac*Nf*x[j][k][l][m][n]*Sum[x[jj][kk][2][m][1],{jj,3,6},{kk,0,2}]+dc*Sum[x[jj][kk][3][m][1],{jj,3,6},
{kk,0,2}],0]+
If[(j>2)&&(l=3)&&(m=1)&&(n=1),ac*Nf*x[0][0][1][m][0]*x[j][k][2][m][n]-dc*x[j][k][l][m][n],0]
```

PER-GSK3β

```
x[j][k][l][m][n]'=
If[(j>2)&&((l=0)||(l=1)),-
If[m=1,Nf,1]*agp*x[j][k][l][m][n]*x[0][0][2][m][0]+dg*x[j][k][l+2][m][n],0]+
```

```
If[(j=0)&&(k=0)&&(l=2)&&(n=0),-
If[m=1,Nf,1]*agp*Sum[x[jj][kk][ll][m][nn],{jj,3,6},{kk,0,2},{ll,0,1},{nn,0,1}]*x[j][k][l][m][n]+dg*
Sum[x[jj][kk][ll][m][nn],{jj,3,6},{kk,0,2},{ll,2,3},{nn,0,1}],0]+
If[(j>2)&&((l=2)||(l=3)),If[m=1,Nf,1]*agp*x[j][k][l-2][m][n]*x[0][0][2][m][0]-dg*x[j][k][l][m][n],0]
```

PER-BMALs-CLOCK/NPAS2

```
x[j][k][l][m][n]'=
If[(j>0)&&(m=1)&&(n=0),-bbin*Nf*x[j][k][l][m][n]*x[0][0][0][m][1]+unbbin*x[j][k][l][m][1],0]+
If[(j=0)&&(k=0)&&(l=0)&&(m=1)&&(n=1),-
bbin*Nf*Sum[x[jj][kk][ll][m][0],{jj,1,6},{kk,0,2},{ll,0,3}]*x[j][k][l][m][n]+unbbin*Sum[x[jj][kk][ll][
m][n],{jj,1,6},{kk,0,2},{ll,0,3}],0]+
If[(j>0)&&(m=1)&&(n=1),bbin*Nf*x[j][k][l][m][0]*x[0][0][0][m][n]-unbbin*x[j][k][l][m][n],0]
```

CRY-BMALs-CLOCK/NPAS2

```
x[j][k][l][m][n]'=
If[(j=0)&&(k>0)&&(l=0)&&(m=1)&&(n=0),-
cbbin*Nf*x[j][k][l][m][n]*x[0][0][0][m][1]+uncbbin*x[j][k][l][m][1],0]+
If[(j=0)&&(k=0)&&(l=0)&&(m=1)&&(n=1),-
cbbin*Nf*Sum[x[0][kk][0][m][0],{kk,1,2}]*x[j][k][l][m][n]+uncbbin*Sum[x[0][kk][0][m][n],{kk,1
,2}],0]+
If[(j=0)&&(k>0)&&(l=0)&&(m=1)&&(n=1),cbbin*Nf*x[j][k][l][m][0]*x[0][0][0][m][n]-
uncbbin*x[j][k][l][m][n],0]+
```

REV-ERBs-GSK3β

```
x[j][k][l][m][n]'=
If[(j=0)&&(k=0)&&(l=2)&&(m=0)&&(n=0),-
ag*cyrev*x[j][k][l][m][n]+(dg)*cyrevg+(dg)*cyrevgp,0]+
```

```
If[(j=0)&&(k=0)&&(l=2)&&(m=1)&&(n=0),-
ag*Nf*revn*x[j][k][l][m][n]+(dg)*revng+(dg)*revngp,0]
```

(6) Translocation

PER binding proteins

```
x[j][k][l][m][n]'=
If[((j=2)||(j=4)||(j=5)||(j=6))&&(m=1),-
ne*If[(n=0),1,0]*x[j][k][l][m][n]+If[(n=0),1,0]*nl*x[j][k][l][0][n],0]+
If[((j=2)||(j=4)||(j=5)||(j=6))&&(m=0),ne*If[(n=0),1,0]*x[j][k][l][1][n]-
If[(n=0),1,0]*nl*x[j][k][l][m][n],0]+
```

BMALs-CLOCK/NPAS2

```
x[j][k][l][m][n]'=
If[(j=0)&&(k=0)&&(l=0)&&(m=1)&&(n=1, nlbc*x[j][k][l][0][n],0]+
If[(j=0)&&(k=0)&&(l=0)&&(m=0)&&(n=1),-nlbc*x[j][k][l][m][n],0]+
```

Kinase

```
x[j][k][l][m][n]'=
If[(j=0)&&(k=0)&&((l=1)||(l=2))&&(m=1)&&(n=0),-lne*x[j][k][l][m][n],0]+
If[(j=0)&&(k=0)&&((l=1)||(l=2))&&(m=0)&&(n=0),lne*x[j][k][l][1][n],0]
```

(7) Phosphorylation

```
x[j][k][l][m][n]'=
If[((j=1))&&(l=1)&&(k=0)&&(m=0)&&(n=0),-hoo*x[j][k][l][m][n],0]+
If[((j=2))&&(l=1)&&(k=0)&&(m=0)&&(n=0),+hoo*x[1][k][l][m][n],0]+
If[((j=3)||(j=5))&&((l=1)||(l=3))&&(k=0),-hto*x[j][k][l][m][n],0]+
If[((j=4)||(j=6))&&((l=1)||(l=3))&&(k=0),hto*x[j-1][k][l][m][n],0]+
```

```
If[((j=3)||(j=4))&&((l=2)||(l=3)),-gto*x[j][k][l][m][n],0]+If[((j=5)||(j=6))&&((l=2)||(l=3)),gto*x[j-2][k][l][m][n],0]+
If[(j=0)&&(k=0)&&(l=0)&&(m=0)&&(n=1),phos*BC,0]
```

(8) Degradation

PER and CRY

```
x[j][k][l][m][n]'=
If[(j=0)&&(k=1)&&(l=0)&&(n=0),-uro*x[j][k][l][m][n],0]+
If[(j=0)&&(k=2)&&(l=0)&&(n=0),-urt*x[j][k][l][m][n],0]+
If[(j=0)&&(k=1)&&(l=0)&&(m=1)&&(n=1),-uro*x[j][k][l][m][n],0]+
If[(j=0)&&(k=2)&&(l=0)&&(m=1)&&(n=1),-urt*x[j][k][l][m][n],0]+
If[(j=0)&&(k=0)&&(l=0)&&(m=1)&&(n=1),uro*x[j][1][l][m][n]+urt*x[j][2][l][m][n],0]+
If[((j=1)||(j=3)||(j=5))&&(k=0),-If[(m=0)&&(n=1),0,1]*upu*x[j][k][l][m][n],0]+
If[((j=2)||(j=4)||(j=6))&&(k=0),-If[(m=0)&&(n=1),0,1]*up*x[j][k][l][m][n],0]+
If[(j=0)&&(k=0)&&(l=1)&&(n=0),up*Sum[x[jj][0][ll][m][nn],{jj,2,6,2},{nn,0,1},{ll,1,3,2}]+upu*Sum[x[jj][0][ll][m][nn],{jj,1,5,2},{nn,0,1},{ll,1,3,2}],0]+
If[(j=0)&&(k=0)&&(l=2)&&(n=0),up*Sum[x[jj][0][ll][m][nn],{jj,2,6,2},{ll,2,3},{nn,0,1}]+upu*Sum[x[jj][0][ll][m][nn],{jj,1,5,2},{ll,2,3},{nn,0,1}],0]+
If[(j=0)&&(k=0)&&(l=0)&&(n=1)&&(m=1),up*Sum[x[jj][0][ll][m][n],{jj,2,6,2},{ll,0,3}]+upu*Sum[x[jj][0][ll][m][n],{jj,1,5,2},{ll,0,3}],0]
```

BMALs-CLOCK/NPAS2 and REV-ERBs

```
x[j][k][l][m][n]'=
If[(j>0)&&(k=0)&&(m=1)&&(n=1),-ubc*x[j][k][l][m][n],0]+
If[(j=0)&&(k=0)&&(l=0)&&(n=1),-ubc*x[j][k][l][m][n],0]+
If[(j>0)&&(k=0)&&(m=1)&&(n=0),ubc*x[j][k][l][m][1],0]+
If[(j=0)&&(k=0)&&(l=2)&&(m=0)&&(n=0),urev*cyrevg+uprev*cyrevgp,0]+
If[(j=0)&&(k=0)&&(l=2)&&(m=1)&&(n=0),urev*revng+uprev*revngp,0]
```

(9) Transcriptional Activity of GSK3β

gto'=trgto*G*GB-ugto*gto

(10) Light Activity

ltn'=60*lta*(1-ltn)-ltb*ltn

MnPo'=trPo*G-tmc*MnPo-umPo*MnPo+lono*19.9*lta*(1-ltn[t])*trPo

MnPt'=trPt*G-tmc*MnPt-umPt*MnPt+lont*19.9*lta*(1-ltn[t])*trPt

(11) The way to understand the equations of multi-state variables

x[j][k][l][m][n]'=If[(j=1)&&(k=0)&&(l=0)&&(m=0)&&(n=0),tlp*McPo,0] is same with x[1][0][0][0][0]'= tlp*McPo. This means PER1 proteins are translated from cytoplasmic Per1 mRNA (McPo) with the rate, tlp.

x[j][k][l][m][n]'=If[(j=0)&&(k=0)&&(l=0)&&(m=1)&&(n=1), nlbc*x[j][k][l][0][n],0] is same with x[0][0][0][1][1]'= nlbc*x[0][0][0][0][1]. This means that BMALs-CLOCK/NPAS in cytoplasm (x[0][0][0][0][1]) enters the nucleus and becomes x[0][0][0][1][1], with rate nlbc.

Appendix B Mathematical analysis of the simple model of circadian clocks

B.1 Description and nondimensionalization of the simple model

The simple model is generated by modifying the well-studied Goodwin model to include an activator, which can be inactivated when bound in complex with the repressor. The mRNA (M) is transcribed proportional to the % of unbound free activator *f* (P, A, K_d), which indicates the activity of the promoter (112, 117). Then, as in the Goodwin model, mRNA is translated to cytoplasmic protein P_c. P_c enters the nucleus (denoted P). P then represses transcription by inhibiting activator A through binding with dissociation constant K_d.

$$\frac{dM}{dt} = \alpha_1 f(P, A, K_d) - \beta_1 M$$

$$\frac{dP_c}{dt} = \alpha_2 M - \beta_2 P_c$$

$$\frac{dP}{dt} = \alpha_3 P_c - \beta_3 P$$

$$f(P, A, K_d) = \frac{1}{2}\left(1 - P/A - K_d/A + \sqrt{(1 - P/A - K_d/A)^2 + 4K_d/A}\right)$$

B.1.1 The SNF Model

The model has 8 parameters. We reduce the number of parameters by scaling and assuming degradation rates are the same to increase the chance of the oscillations. In scaling all variables, we have

$$M = \hat{M}M^*, P = \hat{P}P^*, P_c = \hat{P}_c P_c^*, A = \hat{A}A^*, K_d = \hat{K}_d K_d^*, t = \hat{t}t^* .$$

and the model equations are

$$
\begin{aligned}
&\frac{d\hat{M}M^*}{d\hat{t}t^*} = \alpha_1 f(\hat{P}P^*, \hat{A}A^*, \hat{K}_d K_d^*) - \beta_1 \hat{M}M^* \\
&\frac{d\hat{P}_c P_c^*}{d\hat{t}t^*} = \alpha_2 \hat{M}M^* - \beta_2 \hat{P}_c P_c^* \\
&\frac{d\hat{P}P^*}{d\hat{t}t^*} = \alpha_3 \hat{P}_c P_c^* - \beta_3 \hat{P}P^* \\
&f(\hat{P}P^*, \hat{A}A^*, \hat{K}_d K_d^*) = \frac{1}{2}\left(1 - \hat{P}P^* / \hat{A}A^* - \hat{K}_d K_d^* / \hat{A}A^* + \sqrt{(1 - \hat{P}P^* / \hat{A}A^* - \hat{K}_d K_d^* / \hat{A}A^*)^2 + 4\hat{K}_d K_d^* / \hat{A}A^*}\right)
\end{aligned}
$$

By selecting the scale of each variables as

$$M^* = \frac{\alpha_1}{\beta_1}, P_C^* = \frac{\alpha_1\alpha_2}{\beta_1\beta_2}, P^* = A^* = K_d^* = \frac{\alpha_1\alpha_2\alpha_3}{\beta_1\beta_2\beta_3}, t^* = \frac{1}{\beta_1}$$

and assuming the entire degradation rates are the same to increase the chance of oscillations (17) as

$$\beta_1 = \beta_2 = \beta_3$$

the system becomes

$$
\begin{aligned}
&\frac{d\hat{M}}{d\hat{t}} = f(\hat{P}, \hat{A}, \hat{K}_d) - \hat{M} \\
&\frac{d\hat{P}_c}{d\hat{t}} = \hat{M} - \hat{P}_c \\
&\frac{d\hat{P}}{d\hat{t}} = \hat{P}_c - \hat{P} \\
&f(\hat{P}, \hat{A}, \hat{K}_d) = \frac{1}{2}\left(1 - \hat{P} / \hat{A} - \hat{K}_d / \hat{A} + \sqrt{(1 - \hat{P} / \hat{A} - \hat{K}_d / \hat{A})^2 + 4\hat{K}_d / \hat{A}}\right)
\end{aligned}
$$

This system has now two non-dimensional parameters, dissociation constant ($\hat{K}_d$) and the concentration of the activator ($\hat{A}$). Because these two parameters are scaled by the all the original parameters, these two parameters represents combined effect of all original parameters on the behavior of the system. Therefore, the model's behavior including the range of stoichiometry where the model becomes rhythmic (Figure 3-3D), the sensitivity of the stoichiometry (Figure 3-6B) and the robustness of the rhythms as parameters are perturbed (Figure 3-9A) can be understood by the effects of these two parameters.

B.1.2 The NNF and PNF models

This single negative feedback loop (SNF) model can be extended by adding additional negative or positive feedback loops controlling the production of activator.

$$\begin{aligned} \frac{dR}{dt} &= \gamma_1 f(P, A, K_d) - \delta_1 R \\ \frac{dA}{dt} &= \frac{\gamma_2}{R} - \delta_2 A \end{aligned} \qquad \text{(Additional Negative Feedback Loop)}$$

$$\begin{aligned} \frac{dR}{dt} &= \gamma_1 f(P, A, K_d) - \delta_1 R \\ \frac{dA}{dt} &= \gamma_2 R - \delta_2 A \end{aligned} \qquad \text{(Additional Positive Feedback Loop)}$$

We can also reduce the number of parameters by scaling the R and assuming the degradation rate of R and A are the same.

$$\begin{aligned} \frac{d\hat{R}}{d\hat{t}} &= f(\hat{P}, \hat{A}, \hat{K}_d) - \delta \hat{R} \\ \frac{d\hat{A}}{d\hat{t}} &= \frac{\gamma}{\hat{R}} - \delta \hat{A} \end{aligned} \qquad \text{(Additional Negative Feedback Loop)}$$

$$\frac{d\hat{R}}{d\hat{t}} = f(\hat{P}, \hat{A}, \hat{K}_d) - \delta\hat{R}$$

(Additional Positive Feedback Loop)

$$\frac{d\hat{A}}{d\hat{t}} = \gamma\hat{R} - \delta\hat{A}$$

Then, both the NNF (Negative-Negative Feedback Loops) model and the PNF (Positive-Negative Feedback Loops) model have three free parameters, a dissociation constant ($\hat{K}_d$), a transcription rate of the activator (γ) and a degradation rate of the activator (δ). The SNF model has two free parameters, dissociation constant ($\hat{K}_d$) and the fixed level of activator concentration ($\hat{A}$). Because $\delta = \delta_1 / \beta_1$, δ also represents the relative speed of the additional feedback loop.

B.2 Analysis showing that a balanced stoichiometry promotes oscillations

Recent studies have shown that when repressor binds to an activator to repress transcription, an ultrasensitive response (a large change in transcription rate for a small change in repressor or activator concentration) can be seen when the stoichiometry of the activator and repressor is near 1-1 (112, 117). Many previous studies have argued that ultrasensitive responses can cause oscillations in feedback loops (2, 116). These results are built on a longstanding mathematical theory (2, 17, 223). The combination of these results shows why a balanced stoichiometry leads to oscillations in transcription-translation feedback loops.

These previous studies also match our simulation results (Figure 3-3D). To provide further evidence for these results, we now provide detailed mathematical analysis of our simplified mathematical model (See below). Additionally, we showed that a 1-1 stoichiometry leads to the ultra-sensitivity in our detailed and simple models (Figure 3-5A).

This analysis first considers the stability of the fixed point of the model. By the theory of Mallet-Paret and Smith, instability of the fixed point implies that the model will oscillate (224). The "Secant Condition" proposed by Thron and several earlier authors can be used to determine whether the fixed point is unstable (223, 225) . This gives a range of stoichiometry around 1-1 where oscillations can be seen. We then also use recent nonlinear analysis presented in (17) to show that if the fixed point is stable, that no oscillations can be seen. We then show that if the stoichiometry is far from 1-1, no oscillations can be seen.

B.2.1 Local instability analysis when K_d=0

The secant condition shows that the fixed point will be unstable if

$$\left|\frac{df}{dP}\frac{P}{f}\right| > (\sec\pi/3)^3 = 8 \; (2.1)$$

and as shown above, the nondimensionalized model has the following form:

$$\begin{aligned} dM/dt &= f(P,A,K_d) - M \\ dP_C/dt &= M - P_C \qquad\qquad (2.2) \\ dP/dt &= P_C - P \end{aligned}$$

at the fixed point, $P/f = 1$, so (2.1) is equivalent to

$$\left|\frac{df}{dP}\right| > (\sec\pi/3)^3 = 8 \; (2.3)$$

Since the dissociation constant (K_d) is small when rhythms occur (Figure 3-3D), let us, for the moment, consider it to be zero (this assumption will be relaxed later). Then:

$$f(P,A,K_d) = \frac{1}{2}\left(1 - P/A - K_d/A + \sqrt{(1-P/A-K_d/A)^2 + 4K_d/A}\right) = \begin{Bmatrix} 1-P/A & P/A \le 1 \\ 0 & otherwise \end{Bmatrix} \equiv \lfloor 1-P/A \rfloor$$

Therefore, the secant condition implies that the system will oscillate if

$$\left|\frac{df}{dP}\right| = \frac{1}{A} > (\sec \pi / 3)^3 = 8$$

Since $1 - P/A = P$ at the fixed point, the model oscillates if

$$S = \frac{P}{A} = \frac{1}{A+1} > \frac{8}{9}$$

We also note, that if the steady state of stoichiometry is greater than 1, the transcription rate of this model is zero, which implies that the value of P at the fixed point would be zero. So the steady state of stoichiometry must be bounded from above by 1. Thus:

$$8/9 < S \leq 1$$

B.2.2 An accurate approximation for $f(P, A, K_d)$ when $K_d \neq 0$

Before analyzing the stability of the simple model ($K_d \neq 0$), we find a simple approximation for $f(P, A, K_d)$. Since oscillations occur only when K_d is small ($<10^{-4}$) (Figure 3-3D), let us assume that $\varepsilon = K_d / A$ is small which implies that the activators and repressors form a stable complex, which is also supported by experimental data (see above). Because we want to show that the model loses rhythms if the stoichiometry is not 1-1, we only consider the case where the stoichiometry is not 1-1. In this case, we can derive a simple approximation for *f*. That is, if the stoichiometry is

$$\frac{P}{A} << 1 - (2\sqrt{2\varepsilon^2 + \varepsilon} - 3\varepsilon) \text{ or } \frac{P}{A} >> 1 + (2\sqrt{2\varepsilon^2 + \varepsilon} + 3\varepsilon)$$

(where the right hand side of these inequalities is very close to 1 when ε is small). These inequalities are equivalent to

$$(1-\frac{P}{A}+\varepsilon)^2 >> 4\varepsilon\frac{P}{A}$$

which allows the Taylor series expansion of *f* and a simple approximation for *f*.

$$\begin{aligned}
&f(P,A,K_d)=\frac{1}{2}\left(1-P/A-K_d/A+\sqrt{(1-P/A-K_d/A)^2+4K_d/A}\right)\\
&= \ \frac{1}{2}\left(1-P/A-\varepsilon+\sqrt{(1-P/A-\varepsilon)^2+4\varepsilon}\right)\\
&=\frac{1}{2}\left(1-P/A-\varepsilon+\sqrt{(1-P/A+\varepsilon)^2+4\varepsilon P/A}\right)\\
&\approx \ \frac{1}{2}\left(1-P/A-\varepsilon+\left|(1-P/A+\varepsilon)\right|+\frac{2\varepsilon P/A}{\left|(1-P/A+\varepsilon)\right|}\right) \quad if\ (1-P/A \ +\varepsilon)^2 << 4\varepsilon P/A \qquad (2.4)\\
&=\begin{cases} 1-\dfrac{P}{A}+\dfrac{\varepsilon P/A}{(1-P/A+\varepsilon)} & if\ P/A << 1-(2\sqrt{2\varepsilon^2+\varepsilon}-3\varepsilon)\ or\ 1-P/A+\varepsilon >> 2\sqrt{2\varepsilon^2+\varepsilon}-2\varepsilon>0\\ \dfrac{\varepsilon(1+\varepsilon)}{(P/A-1-\varepsilon)} & if\ \dfrac{P}{A} >> 1+(2\sqrt{2\varepsilon^2+\varepsilon}+3\varepsilon)\ or\ 1-P/A+\varepsilon << -2\sqrt{2\varepsilon^2+\varepsilon}-2\varepsilon<0 \end{cases}\\
&\approx\begin{cases} 1-P/A & if\ P/A << 1-(2\sqrt{2\varepsilon^2+\varepsilon}-3\varepsilon)\\ \varepsilon/(P/A-1) & if\ P/A >> 1+(2\sqrt{2\varepsilon^2+\varepsilon}+3\varepsilon) \end{cases}
\end{aligned}$$

This approximation matches the original function well (see Figure B-1).

B.2.3 Local instability analysis when $K_d \neq 0$

First, we find a lower bound of the steady state of stoichiometry (*S*) where the model oscillates. If $S = P/A << 1-(2\sqrt{2\varepsilon^2+\varepsilon}-3\varepsilon)$, $f \approx 1-P/A$ by (2.4). Then, the secant condition (2.3) implies

$$\left|df/dP\right| \approx 1/A > 8 \ (2.5)$$

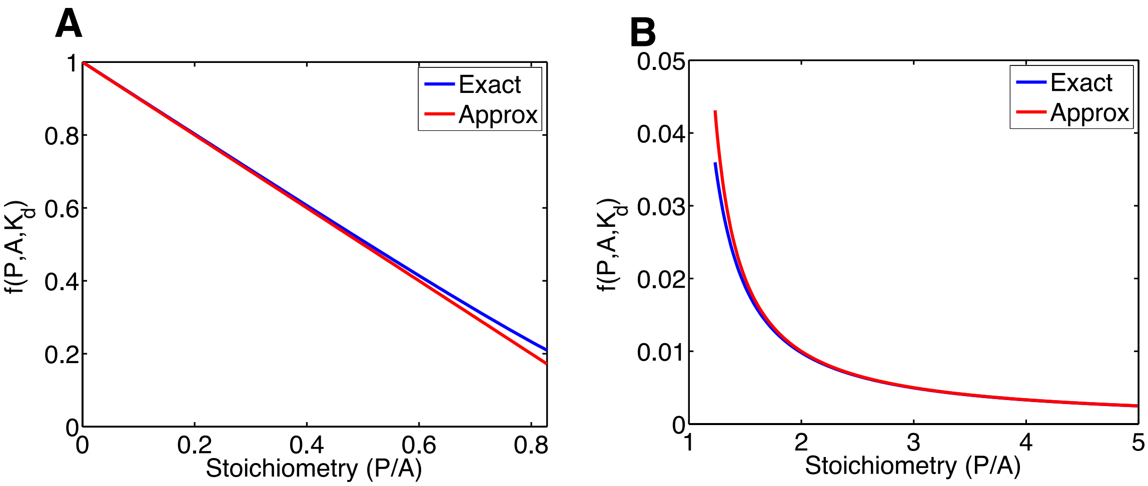

Figure B-1. Approximation of *f*(*P, A, K*$_d$).

(A) Approximation of $f(P,A,K_d)$ with $1-P/A$ when $P/A<1-(2\sqrt{2\varepsilon^2+3\varepsilon}-2\varepsilon)$ and $\varepsilon=K_d/A$ is small. Here, $A=10^{-3}$ and $K_d=10^{-5}$. See Appendix B for details. (B) Approximation of $f(P,A,K_d)$ with $\varepsilon/(P/A-1)$ when $P/A>1+(2\sqrt{2\varepsilon^2+\varepsilon}+3\varepsilon)$.

Since at the fixed point $1-P/A\approx f=P$ or $P\approx A/(A+1)$, (2.5) is equivalent with

$$S\approx\frac{1}{A+1}>\frac{8}{9}\,(2.6)$$

This provides the lower bound of S where the fixed point is unstable. Now, let us find the upper bound. If $S=\dfrac{P}{A}>>1+(2\sqrt{2\varepsilon^2+\varepsilon}+3\varepsilon)$, $f\approx\varepsilon/(P/A-1)$. The secant condition (2.3) implies

$$\left|df/dP\right|\approx\varepsilon A/(P-A)^2>8\,(2.7)$$

Since at the fixed point $\varepsilon/(P/A-1)\approx f=P$, (2.7) is equivalent with

$$\left|f'\right|\approx\frac{\varepsilon A}{(P-A)^2}\approx\frac{P}{P-A}=\frac{P/A}{P/A-1}>8\,(2.8)$$

or

$$P / A > 8(P / A - 1) \quad (2.9)$$

From (2.9), we can get an upper bound on the steady state of stoichiometry where the fixed point is unstable:

$$S = \frac{P}{A} < \frac{8}{7} \quad (2.10)$$

Thus, (2.6) and (2.10) provides the approximate range of the steady state of stoichiometry where the model is locally unstable:

$$\frac{8}{9} < S < \frac{8}{7}$$

Indeed, this approximation matches with the actual stoichiometry range, which is calculated without approximation (see Figure 3-5B). Since the instability of the fixed point implies the oscillation in the model by the theory of Mallet-Paret and Smith, the model can be rhythmic when the steady state of the stoichiometry is around 1-1.

B.2.4 Global stability analysis

At the previous section, we showed that if $S < 8/7$, the model is locally stable. Here, we show that in this case, the model is globally stable (i.e. oscillation does not occur).

(1) *Global stability conditions*

The model becomes globally stable (oscillations cannot be seen) if the gain of $f(P, A, K_d)$ satisfies

$$\left|\frac{f-\langle f\rangle}{P(t)-pm}\right|<8\ (2.11)$$

, where $\langle f\rangle$ is mean of *f* and *pm* is defined by $f(pm,A,K_d)=\langle f\rangle$ (17). The left hand side of the equation is the average slope of *f* between $(pm,\langle f\rangle)$ and $(P(t),f(P(t),A,K_d))$, and since $d^2f/dP^2\geq 0$ (e.g. see Figure 3-4A) we have:

$$\left|\frac{f-\langle f\rangle}{P(t)-pm}\right|\leq\left|\frac{1-\langle f\rangle}{0-pm}\right|=\left|\frac{1-\langle f\rangle}{pm}\right|$$

Therefore,

$$\left|\frac{1-\langle f\rangle}{pm}\right|<8\ (2.12)$$

will be a sufficient condition to show the global stability of the model.

(2) *The average value of P is greater than or equal to the value of P at the fixed point*

The average value of *P* ($\langle P\rangle$) and the average value of *f* ($\langle f(P,A,K_d)\rangle$) of our model (2.2) satisfies $\langle f(P,A,K_d)\rangle=\langle P\rangle$ (17). Since $d^2f/dP^2\geq 0$,

$$\langle f(P,A,K_d)\rangle\geq f(\langle P\rangle,A,K_d)\ (2.13)$$

or

$$\langle P\rangle=\langle f(P,A,K_d)\rangle=f(\langle P\rangle,A,K_d)+\delta \text{ and } \delta\geq 0$$

Since at the fixed point, $P = f(P, A, K_d)$, if $\delta = 0$, the average of P and the steady state of P are the same. If $\delta > 0$, the average of P is greater than the steady state of P or

$$\langle P \rangle \geq P \text{ (2.14)}$$

, where *P* represents the steady state of *P*.

(3) *Global stability when S<8/9*

Since $f(pm, A, K_d) = \langle P \rangle$ and $f(P, A, K_d) = P$ at the fixed point, (2.14) implies that

$$f(pm, A, K_d) = \langle P \rangle \geq P = f(P, A, K_d)$$

Since *f* is a decreasing function of *P*, we find

$$pm \leq P \text{ (2.15)}$$

Therefore,

$$\frac{pm}{A} \leq \frac{P}{A} = S < \frac{8}{9}$$

and we can use approximation (2.4). That is $\langle f \rangle = f(pm, A, K_d) \approx 1 - pm / A$ or $pm \approx A(1 - \langle f \rangle)$. Then, the global stability condition (2.12) is equivalent to

$$\left| \frac{1 - \langle f \rangle}{pm} \right| \approx \left| \frac{1 - \langle f \rangle}{A(1 - \langle f \rangle)} \right| = \frac{1}{A} < 8 \text{ (2.16)}$$

From (2.5) and (2.6), S<8/9 implies that $1/A$<8. Therefore, if S<8/9, the model is globally stable as well as locally stable.

B.2.5 Bounds on the average stoichiometry

If S<8/9, the model is globally stable and $S = \langle S \rangle$. As described above, when S = 8/9, the fixed point becomes unstable and oscillations are seen. At this point, stoichiometry is low and $f \approx 1 - P/A$. Then, the linearity of $f \approx 1 - P/A$ implies the equality of (2.13) and (2.14) or $S \approx \langle S \rangle$ when S = 8/9. Therefore, the model becomes rhythmic when the average stoichiometry is greater than 8/9. This explains the lower bounds of the average stoichiometry that appear in Figure 3-3D.

Since $\langle P \rangle$ is greater than or equal to the steady state shown (2.13), the average stoichiometry ($\langle S \rangle$) is also greater than equal to the steady state of stoichiometry (S). Therefore, if $\langle S \rangle$ is less than 8/7, then S is also less than 8/7 and the model is rhythmic due to (2.10). Therefore, if $\langle S \rangle$ is between 8/9 and 8/7 or $\langle S \rangle$ is around 1-1, the model becomes rhythmic. This explains why a 1-1 average stoichiometry generates the rhythms in the model (Figure 3-3D). However, the upper bound is a sufficient condition (but not a necessary one), so $\langle S \rangle$ is greater than equal to 8/7 does not mean that the model necessarily loses rhythms.

The upper bound of $\langle S \rangle$ increases as K_d is decreases, which can be seen in Figure 3-3D. Here we explain this behavior. When the steady state stoichiometry S reaches its lower bound 8/9, near the fixed point, $S = \langle S \rangle$ or $P = \langle P \rangle$ as shown above**.** This implies that steady state of P/A and pm/A are the same since $f(P) = P$ and $f(pm) = \langle P \rangle$. As the activator concentration decreases, both P/A and pm/A increase from 8/9 to 8/7. When $S = P/A$ reaches its upper bound 8/7, we can expect $pm/A > 1 + (2\sqrt{2\varepsilon^2 + \varepsilon} + 3\varepsilon)$ as in the approximation of *f* above. Then, $< f > \approx \varepsilon / (pm / A - 1) < \varepsilon / (2\sqrt{2\varepsilon^2 + \varepsilon} + 3\varepsilon)$ by (2.4). Since $< f > = < p >$,

$$\frac{< p >}{A} < \frac{\varepsilon}{A(2\sqrt{2\varepsilon^2 + \varepsilon} + 3\varepsilon)} = \frac{1}{A(2\sqrt{2 + \varepsilon^{-1}} + 3)} \quad (2.16)$$

When $S = P / A$ reaches its upper bound 8/7, by (2.7), $A = 7\sqrt{K_d / 8}$ and $\varepsilon = \sqrt{8K_d} / 7$. Then (2.16) becomes

$$\frac{< p >}{A} < \frac{\sqrt{8}}{7\sqrt{K_d}(2\sqrt{2 + 7 / \sqrt{8 / K_d}} + 3)} = \frac{\sqrt{8}}{7(2\sqrt{2K_d + 7\sqrt{K_d / 8}} + 3\sqrt{K_d})} \approx \frac{2}{7\sqrt{7\sqrt{K_d / 2}}} \quad (2.17)$$

(2.17) implies that the upper bound of average stoichiometry $\langle S \rangle$ will increase as K_d decreases, which is seen in Figure 3-3D. Furthermore, (2.17) explains why the model does not oscillate when K_d is too large. For instance, the upper bound of the average stoichiometry becomes 0.61 when $K_d = 10^{-3}$, which is less than the lower bound 8/9. This is why the model does not oscillate when $K_d = 10^{-3}$ (Figure 3-3D). Moreover, the upper bound is 1.16 when $K_d = 10^{-4}$ which matches our simulations in Figure 3-3D. In summary, the mathematical analysis about the range of average stoichiometry implies that

- If $\langle S \rangle < 8/9$, the model is globally stable and does not oscillates.
- If $8/9 < \langle S \rangle < 8/7$, the model is locally instable and oscillates.
- If $S = 8/7$, $\frac{< p >}{A} < \frac{\sqrt{8}}{7(2\sqrt{2K_d + 7\sqrt{K_d / 8}} + 3\sqrt{K_d})} \approx \frac{2}{7\sqrt{7\sqrt{K_d / 2}}}$

This is in agreement with simulations shown in Figure 3-3D: 1) Oscillations are seen around a 1-1 stoichiometry; 2) the stoichiometry needs to be greater than 8/9 for oscillations; 3) as the dissociation constant decreases, oscillations are seen over a larger range of stoichiometry.

B.3 Analysis of the role of an additional feedback loop in balancing a 1-1 stoichiometry

Our simulations showed that an additional negative feedback loop improves the regulation of stoichiometric balance (Figure 3-6B). Here, we provide the mathematical analysis for the simulation results in Figure 3-6B. Because the model only oscillates when the dissociation constant is small (<10^{-4}) (Figure 3-3D), we assume that the dissociation constant is small for the simplicity of the analysis. In this case, the % of free activator equation can be simplified to

$$f(P,A,K_d)=\frac{1}{2}\left(1-P/A-K_d/A+\sqrt{(1-P/A-K_d/A)^2+4K_d/A}\right)\approx\left\{\begin{array}{cc}1-P/A & P/A\le 1\\ 0 & otherwise\end{array}\right\}=\lfloor 1-P/A\rfloor$$

B.3.1 The SNF model

With the approximation, the system can be simplified as

$$\begin{aligned}\frac{dM}{dt}&=\alpha_1\left\lfloor 1-\frac{P}{A}\right\rfloor-\beta_1 M\\ \frac{dP_C}{dt}&=\alpha_2 M-\beta_2 P_C\\ \frac{dP}{dt}&=\alpha_3 P_C-\beta_3 P\end{aligned}$$

Then, the steady state of the system becomes

$$\frac{p/a}{\lfloor 1-p/a\rfloor}a=\frac{\alpha_1\alpha_2\alpha_3}{\beta_1\beta_2\beta_3}\,(3.1)$$

, where *p* and *a* are steady state of *P* and *A* in the system. Since activator is constant, *A* and *a* are the same. Then,

$$\frac{1-\varepsilon}{\varepsilon} = C/a = C_1 \quad (3.2)$$

, where $\varepsilon = \lfloor 1 - p/a \rfloor$ representing the steady state of % of free activator and C_1 represents all parameters of the system.

$$\varepsilon = \frac{1}{1+C_1} \quad (3.3)$$

Now, let's calculate the relative sensitivity of ε with respect to C_1 from the above equation. If this sensitivity is low, then we can expect the % of free activator of this system is stable for the perturbation of any parameters.

$$\frac{d\varepsilon}{dC_1}\frac{C_1}{\varepsilon} = \frac{-1}{(1+C_1)^2} C_1 \frac{1+C_1}{1} = \frac{-C_1}{1+C_1} \quad (3.4)$$

Because the system oscillates only when the stoichiometry between *p* and *a* is close to 1 (Figure 3-3D), ε will become close to 0 and C_1 becomes large from (3.2) or (3.3) when the model oscillates. Therefore, we can expect the relative sensitivity would be around -1 from (3.4) (Figure 3-6C).

B.3.2 The NNF model

Additional secondary loop in the NNF also becomes simple with the assumption K_d=0.

$$\frac{dR}{dt} = \gamma_1 \left\lfloor 1 - \frac{P}{A} \right\rfloor - \delta_1 R$$

$$\frac{dA}{dt} = \frac{\gamma_2}{R} - \delta_2 A$$

Then, the steady state of the activator *A* becomes

$$a = \frac{\gamma_2\delta_1}{\gamma_1\delta_2}\frac{1}{\lfloor 1-p/a\rfloor} = \frac{D}{\lfloor 1-p/a\rfloor} = \frac{D}{\varepsilon} \quad (3.5)$$

By combining two steady state equations (3.1) and (3.5), we can get

$$\frac{1-\varepsilon}{\varepsilon}a = \frac{1-\varepsilon}{\varepsilon}\frac{D}{\varepsilon} = C <=> \frac{1-\varepsilon}{\varepsilon^2} = C/D = C_2$$

Again, C_2 represents the all parameters in NNF.

$$\varepsilon = \frac{-1+\sqrt{1+4C_2}}{2C_2}$$

$$\frac{d\varepsilon}{dC_2}\frac{C_2}{\varepsilon} = \left(\frac{1}{C_2\sqrt{1+4C_2}} - \frac{-1+\sqrt{1+4C_2}}{2C_2^2}\right)C_2\frac{2C_2}{-1+\sqrt{1+4C_2}}$$

For small ε, the relative sensitivity becomes about -0.5 (Figure 3-6C), which is half of that of SNF.

B.3.3 The PNF model

In a similar way used to analyze NNF, we can also derive the steady state of the activator in PNF,

$$a = \frac{\gamma_1\gamma_2}{\delta_1\delta_2}\lfloor 1-p/a\rfloor = E\lfloor 1-p/a\rfloor (3.6)$$

By combining two steady state equations (3.2) and (3.6), we can get

$$\frac{1-\varepsilon}{\varepsilon}A=\frac{1-\varepsilon}{\varepsilon}E\varepsilon=C <=> 1-\varepsilon=C/E=C_3 \quad (3.7)$$

$$\varepsilon=1-C_3 \quad (3.8)$$

$$\frac{d\varepsilon}{dC_3}\frac{C_3}{\varepsilon}=-C_3\frac{1}{1-C_3}=\frac{-C_3}{1-C_3} \quad (3.9)$$

For small ε, 1- C_3 is small by (3.8). Then, we can expect the sensitivity will be huge for small ε (Figure 3-6C) from (3.9). In fact, by combining (3.8) and (3.9),

$$\frac{d\varepsilon}{dC_3}\frac{C_3}{\varepsilon}=\frac{-C_3}{1-C_3}=\frac{-1+\varepsilon}{\varepsilon}\approx\frac{1}{\varepsilon}$$

We can see that the sensitivity is approximately 1/ε.

B.3.4 Summary

The relative sensitivity of the % of free activator (ε) for any parameter perturbation becomes about 1, 0.5 and $1/\varepsilon$ in NF, NNF and PNF, respectively (Figure 3-6C). This means % of free activator (ε) is most robust for parameter perturbation in NNF structure. Because $\varepsilon=\lfloor 1-p/a\rfloor=\lfloor 1-stoichiometry\rfloor$, the robustness of ε in NNF implies the robustness of stoichiometry in the NNF structure. In the previous section, we showed that the model becomes rhythmic when the steady state of stoichiometry is in appropriate range (Figure 3-6C). Since an additional negative feedback loop improves the regulation of the stoichiometric balance, the NNF structure is the best to maintain the rhythms for the perturbations.

B.4 Analysis of the role of an additional negative feedback loop in maintaining a fixed period

We showed that the NNF structure has a nearly constant period in the presence of large changes in gene expression levels (Figure 3-11D). Here, we provide the mathematical analysis for the simulation results in Figure 3-11D. As we showed at the previous section, the simple model can be approximated as

$$\begin{aligned} dM/dt &= \lfloor 1 - P/A \rfloor - M \\ dP_C/dt &= M - P_C \\ dP/dt &= P_C - P \end{aligned} \qquad (4.1)$$

If the transcription rate is increased by α, then the model is changed to

$$\begin{aligned} dM/dt &= \alpha \lfloor 1 - P/A \rfloor - M \\ dP_C/dt &= M - P_C \\ dP/dt &= P_C - P \end{aligned} \qquad (4.2)$$

If we define new variable $\tilde{M} = M/\alpha$, $\tilde{P}_C = P_C/\alpha$ and $\tilde{P} = P/\alpha$, the model (4.2) becomes

$$\begin{aligned} d\tilde{M}/dt &= \lfloor 1 - \alpha\tilde{P}/A \rfloor - \tilde{M} \\ d\tilde{P}_C/dt &= \tilde{M} - \tilde{P}_C \\ d\tilde{P}/dt &= \tilde{P}_C - \tilde{P} \end{aligned} \qquad (4.3)$$

These equations are the same with the original equations (4.1) except for the transcription term, $\lfloor 1 - \alpha\tilde{P}/A \rfloor$. We have shown that the additional negative feedback loop maintains the stoichiometric balance by adjusting the level of the activators according to the change of the repressor levels. In this case, the repressor level is increased by α, so in ideal case, the activator level (A) can be increased by α through the additional negative feedback loop. This makes $\lfloor 1 - \alpha\tilde{P}/A \rfloor$ to the $\lfloor 1 - \tilde{P}/A \rfloor$. That is, with the additional negative feedback loop, (4.3) becomes

$$\begin{aligned} d\tilde{M}/dt &= \lfloor 1-\tilde{P}/A \rfloor - \tilde{M} \\ d\tilde{P}_C/dt &= \tilde{M}-\tilde{P}_C \qquad\qquad (4.4) \\ d\tilde{P}/dt &= \tilde{P}_C - \tilde{P} \end{aligned}$$

Therefore, the model (4.4) has the solution with the same period of the solution of the original model (4.1) while the amplitude of solution ($\tilde{P}$) is increased by α since $\tilde{P} = P/\alpha$.

Appendix C Mathematical description of the p53 model.

Table C-1. Parameters of the model of p53 pulses

Name	Description	Value	Sensitivity	Min	Max
β_{p}	p53$_{inactive}$ production rate	0.9 Cs h^{-1}	-0.03	0.67	>10
β_{sp}	Saturating production rate of p53$_{active}$	10 h^{-1}	-0.04	0.44	>10
β_{mm}	**p53-dependent Mdm2 mRNA production rate**	**9.425 h^{-1}**	**-0.23**	**0.39**	**1.55**
β_{mi}	**p53-independent Mdm2 mRNA production rate**	**0.08 C$_s$ h^{-1}**	**-0.01**	**0**	**5.71**
β_{m}	Mdm2 translation rate	0.9 h^{-1}	-0.24	0.41	1.5
β_{im}	**p53-dependent Wip1 mRNA production rate**	**2.2437 h^{-1}**	**0.18**	**0.79**	**3.22**
β_{i}	Wip1 translation rate	0.25 h^{-1}	0.18	0.79	3.22
β_{rm}	**p53-dependent Rorα mRNA production rate**	**0.52 h^{-1}**	**0.02**	**0**	**>10**
β_{rmi}	**p53-independent Rorα mRNA production rate**	**0.574 C$_s$ h^{-1}**	**0.16**	**0.5**	**3.3**
β_{r}	**Rorα translation rate**	**1.223 h^{-1}**	**0.17**	**0.53**	**2.94**
β_{s}	**Saturating production rate of ATM-P**	**100 Cs h^{-1}**	**-0.12**	**0.77**	**1.92**
α_{mpi}	Saturating MDM2 and Rorα dependent p53$_{inactive}$ degradation rate	5 Cs^{-1} h^{-1}	0.03	0	4.94
α_{pi}	p53$_{inactive}$ degradation rate	2 h^{-1}	0.02	0	2.46
α_{ipa}	Wip1-dependent p53$_{active}$ inactivation rate	0.14 Cs^{-1} h^{-1}	0.01	0	>10
α_{mpa}	Saturating Mdm2 and Rorα dependent p53$_{active}$ degradation rate	1.4 Cs^{-1} h^{-1}	-0.27	0.39	1.5
α_{mm}	**Mdm2 mRNA degradation rate**	**0.583 h^{-1}**	**0.17**	**0.69**	**1.87**
α_{m}	MDM2 degradation rate	1 h^{-1}	0.11	0.47	1.77
α_{sm}	ATM-P-dependent MDM2 inactivation rate	0.5 Cs^{-1} h^{-1}	0.05	0.15	>10
α_{im}	**Wip1 mRNA degradation rate**	**0.769 h^{-1}**	**-0.43**	**0.43**	**1.25**
α_{i}	WIP1 degradation rate	0.7 h^{-1}	-0.42	0.48	1.29

α_{rm}	**Rorα mRNA degradation rate**	**0.295 h^{-1}**	**-0.17**	**0.33**	**1.86**
α_{r}	**RORα degradation rate**	**1.091 h^{-1}**	**-0.17**	**0.33**	**1.91**
α_{is}	Saturating WIP1-dependent ATM-P degradation rate	50 h^{-1}	0.06	0.73	>10
α_{s}	WIP1-independent ATM-P degradation rate	7.5 h^{-1}	0.01	0	1.16
T_s	ATM-P concentration for half-maximal p53 production	1 Cs	0.17	0.57	1.34
T_i	WIP1 concentration for half-maximal ATM-P degradation	0.2 Cs	-0.19	0.32	1.26
T_{rr}	**RORα concentration for half-maximal p53 degradation**	**0.976 Cs^{-1}**	**-0.17**	**0.34**	**1.89**
T_g	**DNA damage for half-maximal ATP-production**	**24**	**0.12**	**0.48**	**1.31**
n_s	Hill coefficient of active p53 production by ATM-P	4	0.15	0.88	>10
n_i	Hill coefficient of ATM-P degradation by WIP1	4	-0.03	0.88	>10
IR	**Strength of γ-irradiation**	**0 ~10 Gy**	**-0.01**	**0.51**	**>10**
n_g	**Constant converting strength of γ-irradiation to DNA damage**	**0.4**	**-0.07**	**0.58**	**2.13**
	$p53_{inactive}$ initial condition	0.243 Cs			
	$p53_{active}$ initial condition	0.077 Cs			
	Mdm2 mRNA initial condition	1.065 Cs			
	MDM2 initial condition	2.336 Cs			
	Wip1 mRNA initial condition	0.081 Cs			
	WIP1 initial condition	0.348 Cs			
	Rorα mRNA initial condition	1.39 Cs			
	RORα initial condition	0.226 Cs			
	ATM-p initial condition	2.083 Cs			

Cs = simulated concentration units. Newly added parameters are highlighted in bold. The name of parameters follows the original model (162, 163). Sensitivity was calculated by $d\log(period)/d\log(parameter)$ in response to 5Gy irradiation. Minimum and maximum factor of parameters between 0 and 10 that can generate sustained p53 pulses were also calculated.

Table C-2. Reaction steps and probabilities in stochastic simulations of p53 pulses.

Reaction Number	Reaction step	Probability of Reaction
1	$* \rightarrow p53_{inactive}$	$\beta_P \times \Omega$
2	$p53_{inactive} \rightarrow *$	$\alpha_{mpi} \times [p53_{inactive}] \times [MDM2] \times \frac{\Omega T_{rr}}{\Omega T_{rr} + [ROR\alpha]}$
3	$p53_{inactive} \rightarrow *$	$\alpha_{pi} \times [p53_{inactive}]$
4	$p53_{inactive} \rightarrow p53_{active}$	$\beta_{sp} \times [p53_{inactive}] \times \frac{[ATM]^{n_s}}{(T_s \times \Omega)^{n_s} + [ATM]^{n_s}}$
5	$p53_{active} \rightarrow *$	$\alpha_{mpa} \times [p53_{active}] \times [MDM2] \times \frac{\Omega T_{rr}}{\Omega T_{rr} + [ROR\alpha]}$
6	$p53_{active} \rightarrow p53_{inactive}$	$\alpha_{ipa} \times [p53_{active}] \times [WIP1]$
7	$* \rightarrow Mdm2$	$\beta_{mi} \times \Omega$
8	$* \rightarrow Mdm2$	$\beta_{mm} \times [p53_{active}]$
9	$Mdm2 \rightarrow *$	$\alpha_{mm} \times [Mdm2]$
10	$* \rightarrow MDM2$	$\beta_m \times [Mdm2]$
11	$MDM2 \rightarrow *$	$\alpha_m \times [MDM2]$
12	$MDM2 \rightarrow *$	$\alpha_{sm} \times [MDM2] \times [ATM]/\Omega$
13	$* \rightarrow Ror\alpha$	$\beta_{rmi} \times \Omega$
14	$* \rightarrow Ror\alpha$	$\beta_{rm} \times [p53_{active}]$
15	$Ror\alpha \rightarrow *$	$\alpha_{rm} \times [Ror\alpha]$
16	$* \rightarrow ROR\alpha$	$\beta_r \times [Ror\alpha]$
17	$ROR\alpha \rightarrow *$	$\alpha_r \times [ROR\alpha]$
18	$* \rightarrow Wip1$	$\beta_{im} \times [p53_{active}]$
19	$Wip1 \rightarrow *$	$\alpha_{im} \times [Wip1]$
20	$* \rightarrow WIP1$	$\beta_i \times [Wip1]$
21	$WIP1 \rightarrow *$	$\alpha_i \times [WIP1]$
22	$* \rightarrow ATM$	$\beta_s \times \Omega \times \frac{IR^{n_g}}{T_g + IR^{n_g}}$
23	$ATM \rightarrow *$	$\alpha_{is} \times [ATM] \times \frac{[WIP1]^{n_i}}{(T_i \times \Omega)^{n_i} + [WIP1]^{n_i}}$
24	$ATM \rightarrow *$	$\alpha_i \times [ATM]$

The parameter Ω represents the number of molecules in the system. Here, we assumed that Ω=100 as did in previous studies (167, 198).

Table C-3. Parameters that describe coupling through Cytochrome-C.

Parameter	Description	Value
β_c	Saturating p53-dependent Cyt-c production rate	1 h^{-1}
α_c	Cyt-c degradation rate	5 h^{-1}
n_c	Hill coefficient of Cyt-c production by $p53_{active}$	2
β_{cf}	Strength of coupling	6
T_c	p53 concentration for half-maximal Cyt-c production	0.1

Table C-4. Ranges of the random parameter sets.

Name	Description	Range
β_{mm}	p53-dependent Mdm2 mRNA production rate	0-50
β_{mi}	p53-independent Mdm2 mRNA production rate	0-50
β_{im}	p53-dependent Wip1 mRNA production rate	0-50
β_{rm}	p53-dependent Rorα mRNA production rate	0-50
β_{rmi}	p53-independent Rorα mRNA production rate	0-50
β_r	Rorα translation rate	0-50
α_{mm}	Mdm2 mRNA degradation rate	0-10
α_{im}	Wip1 mRNA degradation rate	0-10
α_{rm}	Rorα mRNA degradation rate	0-10
α_r	RORα degradation rate	0-10
T_{rr}	RORα concentration for half-maximal p53 degradation	0-10

The random parameters were drawn from the uniform distributions in Figure 4-1D-E. The wider supports or ranges of uniform distributions were used for production rates than degradation rates.

Bibliography

(1) Lahav, G. Oscillations by the p53-Mdm2 feedback loop. *Adv Exp Med Biol* **641**, 28-38 (2008).

(2) Novak, B. & Tyson, J.J. Design principles of biochemical oscillators. *Nat Rev Mol Cell Biol* **9**, 981-91 (2008).

(3) Tsai, T.Y., Choi, Y.S., Ma, W., Pomerening, J.R., Tang, C. & Ferrell, J.E., Jr. Robust, tunable biological oscillations from interlinked positive and negative feedback loops. *Science* **321**, 126-9 (2008).

(4) Goldbeter, A., Gerard, C., Gonze, D., Leloup, J.C. & Dupont, G. Systems biology of cellular rhythms. *FEBS Lett* **586**, 2955-65 (2012).

(5) Schibler, U. & Sassone-Corsi, P. A web of circadian pacemakers. *Cell* **111**, 919-22 (2002).

(6) Purvis, J.E., Karhohs, K.W., Mock, C., Batchelor, E., Loewer, A. & Lahav, G. p53 dynamics control cell fate. *Science* **336**, 1440-4 (2012).

(7) Pomerening, J.R., Kim, S.Y. & Ferrell, J.E., Jr. Systems-level dissection of the cell-cycle oscillator: bypassing positive feedback produces damped oscillations. *Cell* **122**, 565-78 (2005).

(8) Yamada, Y. & Forger, D. Multiscale complexity in the mammalian circadian clock. *Curr Opin Genet Dev* **20**, 626-33 (2010).

(9) Dunlap, J.C. Molecular bases for circadian clocks. *Cell* **96**, 271-90 (1999).

(10) Sancar, A. The intelligent clock and the Rube Goldberg clock. *Nat Struct Mol Biol* **15**, 23-4 (2008).

(11) Tyson, J.J., Albert, R., Goldbeter, A., Ruoff, P. & Sible, J. Biological switches and clocks. *J R Soc Interface* **5 Suppl 1**, S1-8 (2008).

(12) Evans, T., Rosenthal, E.T., Youngblom, J., Distel, D. & Hunt, T. Cyclin: a protein specified by maternal mRNA in sea urchin eggs that is destroyed at each cleavage division. *Cell* **33**, 389-96 (1983).

(13) Emmert-Streib, F. & Glazko, G.V. Network biology: a direct approach to study biological function. *Wiley Interdiscip Rev Syst Biol Med* **3**, 379-91 (2011).

(14) Tyson, J.J., Chen, K. & Novak, B. Network dynamics and cell physiology. *Nat Rev Mol Cell Biol* **2**, 908-16 (2001).

(15) Ko, C.H. & Takahashi, J.S. Molecular components of the mammalian circadian clock. *Hum Mol Genet* **15**, R271-R7 (2006).

(16) Newman, M.E.J. *Networks : an introduction* (Oxford University Press: Oxford ; New York, 2010).

(17) Forger, D.B. Signal processing in cellular clocks. *P Natl Acad Sci USA* **108**, 4281-5 (2011).

(18) Baggs, J.E., Price, T.S., DiTacchio, L., Panda, S., Fitzgerald, G.A. & Hogenesch, J.B. Network features of the mammalian circadian clock. *PLoS Biol* **7**, e52 (2009).

(19) Hughes, M.E. *et al.* Harmonics of circadian gene transcription in mammals. *PLoS Genet* **5**, e1000442 (2009).

(20) Alon, U. Design principles of biological circuits. *Febs J* **277**, 1- (2010).

(21) Gallego, M. & Virshup, D.M. Post-translational modifications regulate the ticking of the circadian clock. *Nat Rev Mol Cell Biol* **8**, 139-48 (2007).

(22) Kim, J.R., Shin, D., Jung, S.H., Heslop-Harrison, P. & Cho, K.H. A design principle underlying the synchronization of oscillations in cellular systems. *J Cell Sci* **123**, 537-43 (2010).

(23) Ko, C.H. *et al.* Emergence of noise-induced oscillations in the central circadian pacemaker. *PLoS Biol* **8**, e1000513 (2010).

(24) Sahar, S. & Sassone-Corsi, P. Metabolism and cancer: the circadian clock connection. *Nat Rev Cancer* **9**, 886-96 (2009).

(25) Meek, D.W. Tumour suppression by p53: a role for the DNA damage response? *Nat Rev Cancer* **9**, 714-23 (2009).

(26) Geva-Zatorsky, N. *et al.* Oscillations and variability in the p53 system. *Mol Syst Biol* **2**, 2006 0033 (2006).

(27) He, M., Zhao, M., Shen, B., Prise, K.M. & Shao, C. Radiation-induced intercellular signaling mediated by cytochrome-c via a p53-dependent pathway in hepatoma cells. *Oncogene* **30**, 1947-55 (2011).

(28) Forger, D.B. & Peskin, C.S. A detailed predictive model of the mammalian circadian clock. *P Natl Acad Sci USA* **100**, 14806-11 (2003).

(29) Mirsky, H.P., Liu, A.C., Welsh, D.K., Kay, S.A. & Doyle, F.J., 3rd. A model of the cell-autonomous mammalian circadian clock. *Proc Natl Acad Sci U S A* **106**, 11107-12 (2009).

(30) Goodwin, B.C. Oscillatory behavior in enzymatic control processes. *Adv Enzyme Regul* **3**, 425-38 (1965).

(31) Griffith, J.S. Mathematics of cellular control processes. I. Negative feedback to one gene. *J Theor Biol* **20**, 202-8 (1968).

(32) Ruoff, P., Vinsjevik, M., Monnerjahn, C. & Rensing, L. The Goodwin model: simulating the effect of light pulses on the circadian sporulation rhythm of Neurospora crassa. *J Theor Biol* **209**, 29-42 (2001).

(33) Miao, H., Xia, X., Perelson, A.S. & Wu, H. On Identifiability of Nonlinear Ode Models and Applications in Viral Dynamics. *SIAM Rev Soc Ind Appl Math* **53**, 3-39 (2011).

(34) Sontag, E.D. Modularity, Retroactivity, and Structural Identification. *Design and Analysis of Biomolecular Circuits:Engineering Approaches to Systems and Synthetic Biology*, 183-200 (2011).

(35) D'Haeseleer, P., Liang, S. & Somogyi, R. Genetic network inference: from co-expression clustering to reverse engineering. *Bioinformatics* **16**, 707-26 (2000).

(36) Pigolotti, S., Krishna, S. & Jensen, M.H. Oscillation patterns in negative feedback loops. *P Natl Acad Sci USA* **104**, 6533-7 (2007).

(37) Wang, Y., Zhang, X.S. & Chen, L. A network biology study on circadian rhythm by integrating various omics data. *Omics* **13**, 313-24 (2009).

(38) Jensen, M.H., Pigolotti, S. & Krishna, S. Genetic oscillation patterns. *The European Physical Journal Special Topics* **178**, 45-56 (2010).

(39) Konopka, T. Automated analysis of biological oscillator models using mode decomposition. *Bioinformatics* **27**, 961-7 (2011).

(40) Geva-Zatorsky, N., Dekel, E., Batchelor, E., Lahav, G. & Alon, U. Fourier analysis and systems identification of the p53 feedback loop. *Proc Natl Acad Sci U S A* **107**, 13550-5 (2010).

(41) Meiss, J.D. *Differential dynamical systems* (Society for Industrial and Applied Mathematics: Philadelphia, 2007).

(42) Craciun, G. & Pantea, C. Identifiability of chemical reaction networks. *Journal of Mathematical Chemistry* **44**, 244-59 (2007).

(43) Marcus, S. On Locally Recurrent Functions. *Am Math Mon* **70**, 822-& (1963).

(44) Ueda, H.R. *et al.* System-level identification of transcriptional circuits underlying mammalian circadian clocks. *Nat Genet* **37**, 187-92 (2005).

(45) Levi, F. & Schibler, U. Circadian rhythms: mechanisms and therapeutic implications. *Annu Rev Pharmacol Toxicol* **47**, 593-628 (2007).

(46) Dibner, C., Schibler, U. & Albrecht, U. The mammalian circadian timing system: organization and coordination of central and peripheral clocks. *Annu Rev Physiol* **72**, 517-49 (2010).

(47) Harmer, S.L. The circadian system in higher plants. *Annu Rev Plant Biol* **60**, 357-77 (2009).

(48) Dunlap, J.C., Loros, J.J. & DeCoursey, P.J. *Chronobiology : biological timekeeping* (Sinauer Associates: Sunderland, Mass., 2004).

(49) Ko, C.H. & Takahashi, J.S. Molecular components of the mammalian circadian clock. *Hum Mol Genet* **15 Spec No 2**, R271-7 (2006).

(50) Dibner, C. *et al.* Circadian gene expression is resilient to large fluctuations in overall transcription rates. *Embo J* **28**, 123-34 (2009).

(51) Stricker, J., Cookson, S., Bennett, M.R., Mather, W.H., Tsimring, L.S. & Hasty, J. A fast, robust and tunable synthetic gene oscillator. *Nature* **456**, 516-9 (2008).

(52) Tigges, M., Marquez-Lago, T.T., Stelling, J. & Fussenegger, M. A tunable synthetic mammalian oscillator. *Nature* **457**, 309-12 (2009).

(53) Blau, J. & Young, M.W. Cycling vrille expression is required for a functional Drosophila clock. *Cell* **99**, 661-71 (1999).

(54) Benito, J., Zheng, H. & Hardin, P.E. PDP1epsilon functions downstream of the circadian oscillator to mediate behavioral rhythms. *J Neurosci* **27**, 2539-47 (2007).

(55) Liu, A.C., Tran, H.G., Zhang, E.E., Priest, A.A., Welsh, D.K. & Kay, S.A. Redundant function of REV-ERBalpha and beta and non-essential role for Bmal1 cycling in transcriptional regulation of intracellular circadian rhythms. *PLoS Genet* **4**, e1000023 (2008).

(56) Glossop, N.R., Lyons, L.C. & Hardin, P.E. Interlocked feedback loops within the Drosophila circadian oscillator. *Science* **286**, 766-8 (1999).

(57) Preitner, N. *et al.* The orphan nuclear receptor REV-ERBalpha controls circadian transcription within the positive limb of the mammalian circadian oscillator. *Cell* **110**, 251-60 (2002).

(58) Bugge, A. *et al.* Rev-erbalpha and Rev-erbbeta coordinately protect the circadian clock and normal metabolic function. *Genes Dev* **26**, 657-67 (2012).

(59) Cho, H. *et al.* Regulation of circadian behaviour and metabolism by REV-ERB-alpha and REV-ERB-beta. *Nature* **485**, 123-7 (2012).

(60) Etchegaray, J.P. *et al.* Casein kinase 1 delta regulates the pace of the mammalian circadian clock. *Mol Cell Biol* **29**, 3853-66 (2009).

(61) Lee, H., Chen, R., Lee, Y., Yoo, S. & Lee, C. Essential roles of CKIdelta and CKIepsilon in the mammalian circadian clock. *Proc Natl Acad Sci U S A* **106**, 21359-64 (2009).

(62) Lee, Y., Chen, R., Lee, H.M. & Lee, C. Stoichiometric relationship among clock proteins determines robustness of circadian rhythms. *J Biol Chem* **286**, 7033-42 (2011).

(63) Lee, C., Etchegaray, J.P., Cagampang, F.R., Loudon, A.S. & Reppert, S.M. Posttranslational mechanisms regulate the mammalian circadian clock. *Cell* **107**, 855-67 (2001).

(64) Menet, J.S., Abruzzi, K.C., Desrochers, J., Rodriguez, J. & Rosbash, M. Dynamic PER repression mechanisms in the Drosophila circadian clock: from on-DNA to off-DNA. *Genes Dev* **24**, 358-67 (2010).

(65) He, Q., Shu, H., Cheng, P., Chen, S., Wang, L. & Liu, Y. Light-independent phosphorylation of WHITE COLLAR-1 regulates its function in the Neurospora circadian negative feedback loop. *J Biol Chem* **280**, 17526-32 (2005).

(66) Huang, G. *et al.* Protein kinase A and casein kinases mediate sequential phosphorylation events in the circadian negative feedback loop. *Genes Dev* **21**, 3283-95 (2007).

(67) Oda, G.A. & Friesen, W.O. Modeling two-oscillator circadian systems entrained by two environmental cycles. *PLoS One* **6**, e23895 (2011).

(68) Kripke, D.F., Mullaney, D.J., Atkinson, M. & Wolf, S. Circadian rhythm disorders in manic-depressives. *Biol Psychiatry* **13**, 335-51 (1978).

(69) Wehr, T.A., Turner, E.H., Shimada, J.M., Lowe, C.H., Barker, C. & Leibenluft, E. Treatment of rapidly cycling bipolar patient by using extended bed rest and darkness to stabilize the timing and duration of sleep. *Biol Psychiatry* **43**, 822-8 (1998).

(70) Lenox, R.H., Gould, T.D. & Manji, H.K. Endophenotypes in bipolar disorder. *Am J Med Genet* **114**, 391-406 (2002).

(71) McClung, C.A. Circadian rhythms and mood regulation: insights from pre-clinical models. *Eur Neuropsychopharmacol* **21 Suppl 4**, S683-93 (2011).

(72) Hirota, T., Lewis, W.G., Liu, A.C., Lee, J.W., Schultz, P.G. & Kay, S.A. A chemical biology approach reveals period shortening of the mammalian circadian clock by specific inhibition of GSK-3beta. *P Natl Acad Sci USA* **105**, 20746-51 (2008).

(73) Pandi-Perumal, S.R., Trakht, I., Spence, D.W., Srinivasan, V., Dagan, Y. & Cardinali, D.P. The roles of melatonin and light in the pathophysiology and treatment of circadian rhythm sleep disorders. *Nat Clin Pract Neurol* **4**, 436-47 (2008).

(74) Isojima, Y. *et al.* CKIepsilon/delta-dependent phosphorylation is a temperature-insensitive, period-determining process in the mammalian circadian clock. *P Natl Acad Sci USA* **106**, 15744-9 (2009).

(75) Hirota, T. *et al.* Identification of small molecule activators of cryptochrome. *Science* **337**, 1094-7 (2012).

(76) Badura, L. *et al.* An inhibitor of casein kinase I epsilon induces phase delays in circadian rhythms under free-running and entrained conditions. *J Pharmacol Exp Ther* **322**, 730-8 (2007).

(77) Walton, K.M. *et al.* Selective inhibition of casein kinase 1 epsilon minimally alters circadian clock period. *J Pharmacol Exp Ther* **330**, 430-9 (2009).

(78) Meng, Q.J. *et al.* Entrainment of disrupted circadian behavior through inhibition of casein kinase 1 (CK1) enzymes. *P Natl Acad Sci USA* **107**, 15240-5 (2010).

(79) Kim, J.K. & Forger, D.B. A mechanism for robust circadian timekeeping via stoichiometric balance. *Mol Syst Biol* **8**, 630 (2012).

(80) Gallego, M., Eide, E.J., Woolf, M.F., Virshup, D.M. & Forger, D.B. An opposite role for tau in circadian rhythms revealed by mathematical modeling. *P Natl Acad Sci USA* **103**, 10618-23 (2006).

(81) Kwon, I. *et al.* BMAL1 shuttling controls transactivation and degradation of the CLOCK/BMAL1 heterodimer. *Mol Cell Biol* **26**, 7318-30 (2006).

(82) Kondratov, R.V., Kondratova, A.A., Lee, C., Gorbacheva, V.Y., Chernov, M.V. & Antoch, M.P. Post-translational regulation of circadian transcriptional CLOCK(NPAS2)/BMAL1 complex by CRYPTOCHROMES. *Cell Cycle* **5**, 890-5 (2006).

(83) Dardente, H., Fortier, E.E., Martineau, V. & Cermakian, N. Cryptochromes impair phosphorylation of transcriptional activators in the clock: a general mechanism for circadian repression. *Biochem J* **402**, 525-36 (2007).

(84) Chen, R. *et al.* Rhythmic PER abundance defines a critical nodal point for negative feedback within the circadian clock mechanism. *Mol Cell* **36**, 417-30 (2009).

(85) Ye, R., Selby, C.P., Ozturk, N., Annayev, Y. & Sancar, A. Biochemical analysis of the canonical model for the mammalian circadian clock. *J Biol Chem* **286**, 25891-902 (2011).

(86) Akashi, M., Tsuchiya, Y., Yoshino, T. & Nishida, E. Control of intracellular dynamics of mammalian period proteins by casein kinase I epsilon (CKIepsilon) and CKIdelta in cultured cells. *Mol Cell Biol* **22**, 1693-703 (2002).

(87) Vielhaber, E., Eide, E., Rivers, A., Gao, Z.H. & Virshup, D.M. Nuclear entry of the circadian regulator mPER1 is controlled by mammalian casein kinase I epsilon. *Mol Cell Biol* **20**, 4888-99 (2000).

(88) Iitaka, C., Miyazaki, K., Akaike, T. & Ishida, N. A role for glycogen synthase kinase-3beta in the mammalian circadian clock. *J Biol Chem* **280**, 29397-402 (2005).

(89) Yin, L., Wang, J., Klein, P.S. & Lazar, M.A. Nuclear receptor Rev-erbalpha is a critical lithium-sensitive component of the circadian clock. *Science* **311**, 1002-5 (2006).

(90) Kronauer, R.E., Forger, D.B. & Jewett, M.E. Quantifying human circadian pacemaker response to brief, extended, and repeated light stimuli over the phototopic range. *J Biol Rhythms* **14**, 500-15 (1999).

(91) Wilsbacher, L.D. *et al.* Photic and circadian expression of luciferase in mPeriod1-luc transgenic mice invivo. *Proc Natl Acad Sci U S A* **99**, 489-94 (2002).

(92) Challet, E., Poirel, V.J., Malan, A. & Pevet, P. Light exposure during daytime modulates expression of Per1 and Per2 clock genes in the suprachiasmatic nuclei of mice. *J Neurosci Res* **72**, 629-37 (2003).

(93) Okamura, H. *et al.* Photic induction of mPer1 and mPer2 in cry-deficient mice lacking a biological clock. *Science* **286**, 2531-4 (1999).

(94) Reppert, S.M. & Weaver, D.R. Coordination of circadian timing in mammals. *Nature* **418**, 935-41 (2002).

(95) Sahar, S., Zocchi, L., Kinoshita, C., Borrelli, E. & Sassone-Corsi, P. Regulation of BMAL1 protein stability and circadian function by GSK3beta-mediated phosphorylation. *PLoS One* **5**, e8561 (2010).

(96) Harada, Y., Sakai, M., Kurabayashi, N., Hirota, T. & Fukada, Y. Ser-557-phosphorylated mCRY2 is degraded upon synergistic phosphorylation by glycogen synthase kinase-3 beta. *J Biol Chem* **280**, 31714-21 (2005).

(97) Miller, M.M., Gould, B.E. & Nelson, J.F. Aging and long-term ovariectomy alter the cytoarchitecture of the hypothalamic-preoptic area of the C57BL/6J mouse. *Neurobiol Aging* **10**, 683-90 (1989).

(98) Gonzalez, O.R., Kuper, C., Jung, K., Naval, P.C., Jr. & Mendoza, E. Parameter estimation using Simulated Annealing for S-system models of biochemical networks. *Bioinformatics* **23**, 480-6 (2007).

(99) Reppert, S.M. & Weaver, D.R. Molecular analysis of mammalian circadian rhythms. *Annu Rev Physiol* **63**, 647-76 (2001).

(100) Yoo, S.H. *et al.* A noncanonical E-box enhancer drives mouse Period2 circadian oscillations in vivo. *P Natl Acad Sci USA* **102**, 2608-13 (2005).

(101) Leloup, J.C. & Goldbeter, A. Toward a detailed computational model for the mammalian circadian clock. *P Natl Acad Sci USA* **100**, 7051-6 (2003).

(102) Relógio, A., Westermark, P.O., Wallach, T., Schellenberg, K., Kramer, A. & Herzel, H. Tuning the Mammalian Circadian Clock: Robust Synergy of Two Loops. *PLoS Comput Biol* **7**, e1002309 (2011).

(103) Liu, A.C. *et al.* Intercellular coupling confers robustness against mutations in the SCN circadian clock network. *Cell* **129**, 605-16 (2007).

(104) Ukai-Tadenuma, M., Yamada, R.G., Xu, H., Ripperger, J.A., Liu, A.C. & Ueda, H.R. Delay in Feedback Repression by Cryptochrome 1 Is Required for Circadian Clock Function. *Cell* **144**, 268-81 (2011).

(105) Busino, L. *et al.* SCFFbxl3 controls the oscillation of the circadian clock by directing the degradation of cryptochrome proteins. *Science* **316**, 900-4 (2007).

(106) Siepka, S.M. *et al.* Circadian mutant Overtime reveals F-box protein FBXL3 regulation of cryptochrome and period gene expression. *Cell* **129**, 1011-23 (2007).

(107) Vitaterna, M.H. *et al.* Mutagenesis and mapping of a mouse gene, Clock, essential for circadian behavior. *Science* **264**, 719-25 (1994).

(108) Herzog, E.D., Takahashi, J.S. & Block, G.D. Clock controls circadian period in isolated suprachiasmatic nucleus neurons. *Nat Neurosci* **1**, 708-13 (1998).

(109) Debruyne, J.P., Noton, E., Lambert, C.M., Maywood, E.S., Weaver, D.R. & Reppert, S.M. A clock shock: mouse CLOCK is not required for circadian oscillator function. *Neuron* **50**, 465-77 (2006).

(110) Yamaguchi, S. *et al.* Synchronization of cellular clocks in the suprachiasmatic nucleus. *Science* **302**, 1408-12 (2003).

(111) Khan, S.K. *et al.* Identification of a novel cryptochrome differentiating domain required for feedback repression in circadian clock function. *J Biol Chem* **287**, 25917-26 (2012).

(112) Buchler, N.E. & Cross, F.R. Protein sequestration generates a flexible ultrasensitive response in a genetic network. *Mol Syst Biol* **5**, 272 (2009).

(113) Froy, O., Chang, D.C. & Reppert, S.M. Redox potential: differential roles in dCRY and mCRY1 functions. *Curr Biol* **12**, 147-52 (2002).

(114) Francois, P. & Hakim, V. Core genetic module: the mixed feedback loop. *Phys Rev E Stat Nonlin Soft Matter Phys* **72**, 031908 (2005).

(115) Sato, T.K. *et al.* Feedback repression is required for mammalian circadian clock function. *Nat Genet* **38**, 312-9 (2006).

(116) Kim, S.Y. & Ferrell, J.E., Jr. Substrate competition as a source of ultrasensitivity in the inactivation of Wee1. *Cell* **128**, 1133-45 (2007).

(117) Buchler, N.E. & Louis, M. Molecular titration and ultrasensitivity in regulatory networks. *J Mol Biol* **384**, 1106-19 (2008).

(118) Barkai, N. & Leibler, S. Circadian clocks limited by noise. *Nature* **403**, 267-8 (2000).

(119) Smolen, P., Baxter, D.A. & Byrne, J.H. A reduced model clarifies the role of feedback loops and time delays in the Drosophila circadian oscillator. *Biophys J* **83**, 2349-59 (2002).

(120) Meng, Q.J. *et al.* Setting clock speed in mammals: the CK1 epsilon tau mutation in mice accelerates circadian pacemakers by selectively destabilizing PERIOD proteins. *Neuron* **58**, 78-88 (2008).

(121) Syed, S., Saez, L. & Young, M.W. Kinetics of doubletime kinase-dependent degradation of the Drosophila period protein. *J Biol Chem* **286**, 27654-62 (2011).

(122) Lamaze, A., Lamouroux, A., Vias, C., Hung, H.C., Weber, F. & Rouyer, F. The E3 ubiquitin ligase CTRIP controls CLOCK levels and PERIOD oscillations in Drosophila. *EMBO Rep* **12**, 549-57 (2011).

(123) Gonzalez, O.R., Kuper, C., Jung, K., Naval, P.C. & Mendoza, E. Parameter estimation using Simulated Annealing for S-system models of biochemical networks. *Bioinformatics* **23**, 480-6 (2007).

(124) Goldbeter, A. A model for circadian oscillations in the Drosophila period protein (PER). *Proc Biol Sci* **261**, 319-24 (1995).

(125) Winfree, A.T. *The geometry of biological time* (Springer Verlag: New York, 1980).

(126) Glass, L. & Winfree, A.T. Discontinuities in phase-resetting experiments. *Am J Physiol* **246**, R251-8 (1984).

(127) Daan, S. & Pittendrigh, C.S. Functional-Analysis of Circadian Pacemakers in Nocturnal Rodents .2. Variability of Phase Response Curves. *J Comp Physiol* **106**, 253-66 (1976).

(128) Comas, M., Beersma, D.G., Spoelstra, K. & Daan, S. Phase and period responses of the circadian system of mice (Mus musculus) to light stimuli of different duration. *J Biol Rhythms* **21**, 362-72 (2006).

(129) Fan, Y., Hida, A., Anderson, D.A., Izumo, M. & Johnson, C.H. Cycling of CRYPTOCHROME proteins is not necessary for circadian-clock function in mammalian fibroblasts. *Curr Biol* **17**, 1091-100 (2007).

(130) Shearman, L.P. *et al.* Interacting molecular loops in the mammalian circadian clock. *Science* **288**, 1013-9 (2000).

(131) Becker-Weimann, S., Wolf, J., Herzel, H. & Kramer, A. Modeling feedback loops of the Mammalian circadian oscillator. *Biophys J* **87**, 3023-34 (2004).

(132) Leloup, J.C. & Goldbeter, A. Modeling the mammalian circadian clock: sensitivity analysis and multiplicity of oscillatory mechanisms. *J Theor Biol* **230**, 541-62 (2004).

(133) Baker, C.L., Loros, J.J. & Dunlap, J.C. The circadian clock of Neurospora crassa. *FEMS Microbiol Rev* **36**, 95-110 (2012).

(134) Welsh, D.K., Yoo, S.H., Liu, A.C., Takahashi, J.S. & Kay, S.A. Bioluminescence imaging of individual fibroblasts reveals persistent, independently phased circadian rhythms of clock gene expression. *Curr Biol* **14**, 2289-95 (2004).

(135) Leise, T.L., Wang, C.W., Gitis, P.J. & Welsh, D.K. Persistent cell-autonomous circadian oscillations in fibroblasts revealed by six-week single-cell imaging of PER2::LUC bioluminescence. *PLoS One* **7**, e33334 (2012).

(136) Langmesser, S., Tallone, T., Bordon, A., Rusconi, S. & Albrecht, U. Interaction of circadian clock proteins PER2 and CRY with BMAL1 and CLOCK. *BMC Mol Biol* **9**, 41 (2008).

(137) Forger, D.B. & Peskin, C.S. Stochastic simulation of the mammalian circadian clock. *P Natl Acad Sci USA* **102**, 321-4 (2005).

(138) Li, D. & Li, C. Noise-induced dynamics in the mixed-feedback-loop network motif. *Phys Rev E Stat Nonlin Soft Matter Phys* **77**, 011903 (2008).

(139) Pokhilko, A., Fernandez, A.P., Edwards, K.D., Southern, M.M., Halliday, K.J. & Millar, A.J. The clock gene circuit in Arabidopsis includes a repressilator with additional feedback loops. *Mol Syst Biol* **8**, 574 (2012).

(140) Rust, M.J., Markson, J.S., Lane, W.S., Fisher, D.S. & O'Shea, E.K. Ordered phosphorylation governs oscillation of a three-protein circadian clock. *Science* **318**, 809-12 (2007).

(141) Sprouse, J., Reynolds, L., Kleiman, R., Tate, B., Swanson, T.A. & Pickard, G.E. Chronic treatment with a selective inhibitor of casein kinase I delta/epsilon yields cumulative phase delays in circadian rhythms. *Psychopharmacology (Berl)* **210**, 569-76 (2010).

(142) Morgenthaler, T.I. *et al.* Practice parameters for the clinical evaluation and treatment of circadian rhythm sleep disorders. An American Academy of Sleep Medicine report. *Sleep* **30**, 1445-59 (2007).

(143) Gooley, J.J. Treatment of circadian rhythm sleep disorders with light. *Ann Acad Med Singapore* **37**, 669-76 (2008).

(144) Barion, A. Circadian rhythm sleep disorders. *Dis Mon* **57**, 423-37 (2011).
(145) Price, M.A. CKI, there's more than one: casein kinase I family members in Wnt and Hedgehog signaling. *Genes Dev* **20**, 399-410 (2006).
(146) Cheong, J.K. *et al.* IC261 induces cell cycle arrest and apoptosis of human cancer cells via CK1delta/varepsilon and Wnt/beta-catenin independent inhibition of mitotic spindle formation. *Oncogene* **30**, 2558-69 (2011).
(147) McCarthy, M.J. & Welsh, D.K. Cellular circadian clocks in mood disorders. *J Biol Rhythms* **27**, 339-52 (2012).
(148) Kennaway, D.J. Clock genes at the heart of depression. *J Psychopharmacol* **24**, 5-14 (2010).
(149) Arey, R. & McClung, C.A. An inhibitor of casein kinase 1 epsilon/delta partially normalizes the manic-like behaviors of the Clock Delta 19 mouse. *Behav Pharmacol* **23**, 392-6 (2012).
(150) Perreau-Lenz, S. *et al.* Inhibition of the casein-kinase-1-epsilon/delta prevents relapse-like alcohol drinking. *Neuropsychopharmacology* **37**, 2121-31 (2012).
(151) Maier, S.F. Learned helplessness and animal models of depression. *Prog Neuropsychopharmacol Biol Psychiatry* **8**, 435-46 (1984).
(152) Spanagel, R. *et al.* The clock gene Per2 influences the glutamatergic system and modulates alcohol consumption. *Nat Med* **11**, 35-42 (2005).
(153) Prickaerts, J. *et al.* Transgenic mice overexpressing glycogen synthase kinase 3beta: a putative model of hyperactivity and mania. *J Neurosci* **26**, 9022-9 (2006).
(154) Roybal, K. *et al.* Mania-like behavior induced by disruption of CLOCK. *P Natl Acad Sci USA* **104**, 6406-11 (2007).
(155) Hampp, G. *et al.* Regulation of monoamine oxidase A by circadian-clock components implies clock influence on mood. *Curr Biol* **18**, 678-83 (2008).
(156) Hanahan, D. & Weinberg, R.A. Hallmarks of cancer: the next generation. *Cell* **144**, 646-74 (2011).
(157) Jain, H.V., Nor, J.E. & Jackson, T.L. Modeling the VEGF-Bcl-2-CXCL8 pathway in intratumoral agiogenesis. *Bulletin of Mathematical Biology* **70**, 89-117 (2008).
(158) Croce, C.M. Oncogenes and cancer. *N Engl J Med* **358**, 502-11 (2008).
(159) Hofseth, L.J., Hussain, S.P. & Harris, C.C. p53: 25 years after its discovery. *Trends Pharmacol Sci* **25**, 177-81 (2004).
(160) Jin, S. & Levine, A.J. The p53 functional circuit. *J Cell Sci* **114**, 4139-40 (2001).
(161) Loewer, A., Batchelor, E., Gaglia, G. & Lahav, G. Basal dynamics of p53 reveal transcriptionally attenuated pulses in cycling cells. *Cell* **142**, 89-100 (2010).
(162) Batchelor, E., Loewer, A., Mock, C. & Lahav, G. Stimulus-dependent dynamics of p53 in single cells. *Mol Syst Biol* **7**, 488 (2011).
(163) Batchelor, E., Mock, C.S., Bhan, I., Loewer, A. & Lahav, G. Recurrent initiation: a mechanism for triggering p53 pulses in response to DNA damage. *Mol Cell* **30**, 277-89 (2008).
(164) Hamstra, D.A., Bhojani, M.S., Griffin, L.B., Laxman, B., Ross, B.D. & Rehemtulla, A. Real-time evaluation of p53 oscillatory behavior in vivo using bioluminescent imaging. *Cancer Res* **66**, 7482-9 (2006).
(165) Lahav, G. *et al.* Dynamics of the p53-Mdm2 feedback loop in individual cells. *Nat Genet* **36**, 147-50 (2004).

(166) Harris, S.L. & Levine, A.J. The p53 pathway: positive and negative feedback loops. *Oncogene* **24**, 2899-908 (2005).

(167) Ouattara, D.A., Abou-Jaoude, W. & Kaufman, M. From structure to dynamics: frequency tuning in the p53-Mdm2 network. II Differential and stochastic approaches. *J Theor Biol* **264**, 1177-89 (2010).

(168) Hunziker, A., Jensen, M.H. & Krishna, S. Stress-specific response of the p53-Mdm2 feedback loop. *BMC Syst Biol* **4**, 94 (2010).

(169) Ma, L., Wagner, J., Rice, J.J., Hu, W., Levine, A.J. & Stolovitzky, G.A. A plausible model for the digital response of p53 to DNA damage. *P Natl Acad Sci USA* **102**, 14266-71 (2005).

(170) Ciliberto, A., Novak, B. & Tyson, J.J. Steady states and oscillations in the p53/Mdm2 network. *Cell Cycle* **4**, 488-93 (2005).

(171) Vogelstein, B., Lane, D. & Levine, A.J. Surfing the p53 network. *Nature* **408**, 307-10 (2000).

(172) Lev Bar-Or, R., Maya, R., Segel, L.A., Alon, U., Levine, A.J. & Oren, M. Generation of oscillations by the p53-Mdm2 feedback loop: a theoretical and experimental study. *P Natl Acad Sci USA* **97**, 11250-5 (2000).

(173) Toettcher, J.E., Mock, C., Batchelor, E., Loewer, A. & Lahav, G. A synthetic-natural hybrid oscillator in human cells. *P Natl Acad Sci USA* **107**, 17047-52 (2010).

(174) Sun, T., Yang, W., Liu, J. & Shen, P. Modeling the basal dynamics of p53 system. *PLoS One* **6**, e27882 (2011).

(175) Iwamoto, K., Hamada, H., Eguchi, Y. & Okamoto, M. Mathematical modeling of cell cycle regulation in response to DNA damage: exploring mechanisms of cell-fate determination. *Biosystems* **103**, 384-91 (2011).

(176) Li, Z., Ni, M., Li, J., Zhang, Y., Ouyang, Q. & Tang, C. Decision making of the p53 network: Death by integration. *J Theor Biol*, (2010).

(177) Sun, T., Chen, C., Wu, Y., Zhang, S., Cui, J. & Shen, P. Modeling the role of p53 pulses in DNA damage- induced cell death decision. *BMC Bioinformatics* **10**, 190 (2009).

(178) Zhang, T., Brazhnik, P. & Tyson, J.J. Exploring mechanisms of the DNA-damage response: p53 pulses and their possible relevance to apoptosis. *Cell Cycle* **6**, 85-94 (2007).

(179) Kim, J., Heslop-Harrison, P., Postlethwaite, I. & Bates, D.G. Stochastic noise and synchronisation during dictyostelium aggregation make cAMP oscillations robust. *PLoS Comput Biol* **3**, e218 (2007).

(180) Moortgat, K.T., Bullock, T.H. & Sejnowski, T.J. Gap junction effects on precision and frequency of a model pacemaker network. *J Neurophysiol* **83**, 984-97 (2000).

(181) Herzog, E.D., Aton, S.J., Numano, R., Sakaki, Y. & Tei, H. Temporal precision in the mammalian circadian system: a reliable clock from less reliable neurons. *J Biol Rhythms* **19**, 35-46 (2004).

(182) Li, Q. & Wang, Y. Coupling and internal noise sustain synchronized oscillation in calcium system. *Biophys Chem* **129**, 23-8 (2007).

(183) Mayo, L.D., Dixon, J.E., Durden, D.L., Tonks, N.K. & Donner, D.B. PTEN protects p53 from Mdm2 and sensitizes cancer cells to chemotherapy. *J Biol Chem* **277**, 5484-9 (2002).

(184) Martoriati, A., Doumont, G., Alcalay, M., Bellefroid, E., Pelicci, P.G. & Marine, J.C. dapk1, encoding an activator of a p19ARF-p53-mediated apoptotic checkpoint, is a transcription target of p53. *Oncogene* **24**, 1461-6 (2005).

(185) Deguin-Chambon, V., Vacher, M., Jullien, M., May, E. & Bourdon, J.C. Direct transactivation of c-Ha-Ras gene by p53: evidence for its involvement in p53 transactivation activity and p53-mediated apoptosis. *Oncogene* **19**, 5831-41 (2000).

(186) Ongusaha, P.P. *et al.* p53 induction and activation of DDR1 kinase counteract p53-mediated apoptosis and influence p53 regulation through a positive feedback loop. *Embo J* **22**, 1289-301 (2003).

(187) Kim, H. *et al.* DNA damage-induced RORalpha is crucial for p53 stabilization and increased apoptosis. *Mol Cell* **44**, 797-810 (2011).

(188) Little, J.B. Cellular radiation effects and the bystander response. *Mutat Res* **597**, 113-8 (2006).

(189) Mackey, M.C. & Glass, L. Oscillation and chaos in physiological control systems. *Science* **197**, 287-9 (1977).

(190) Josic, K., Lopez, J.M., Ott, W., Shiau, L. & Bennett, M.R. Stochastic delay accelerates signaling in gene networks. *PLoS Comput Biol* **7**, e1002264 (2011).

(191) Alon, U., Surette, M.G., Barkai, N. & Leibler, S. Robustness in bacterial chemotaxis. *Nature* **397**, 168-71 (1999).

(192) Barkai, N. & Leibler, S. Robustness in simple biochemical networks. *Nature* **387**, 913-7 (1997).

(193) Savageau, M.A. Are There Rules Governing Patterns of Gene-Regulation. *Theoretical Biology*, 42-66 (1989).

(194) Wang, Y., Solt, L.A., Kojetin, D.J. & Burris, T.P. Regulation of p53 stability and apoptosis by a ROR agonist. *PLoS One* **7**, e34921 (2012).

(195) Bakkenist, C.J. & Kastan, M.B. Initiating cellular stress responses. *Cell* **118**, 9-17 (2004).

(196) Huang, L.C., Clarkin, K.C. & Wahl, G.M. Sensitivity and selectivity of the DNA damage sensor responsible for activating p53-dependent G1 arrest. *P Natl Acad Sci USA* **93**, 4827-32 (1996).

(197) Gillespie, D.T. Exact Stochastic Simulation of Coupled Chemical-Reactions. *J Phys Chem-Us* **81**, 2340-61 (1977).

(198) Gonze, D., Halloy, J. & Goldbeter, A. Deterministic versus stochastic models for circadian rhythms. *J Biol Phys* **28**, 637-53 (2002).

(199) Rao, C.V. & Arkin, A.P. Stochastic chemical kinetics and the quasi-steady-state assumption: Application to the Gillespie algorithm. *J Chem Phys* **118**, 4999-5010 (2003).

(200) Barik, D., Paul, M.R., Baumann, W.T., Cao, Y. & Tyson, J.J. Stochastic simulation of enzyme-catalyzed reactions with disparate timescales. *Biophys J* **95**, 3563-74 (2008).

(201) Wilkins, A.K., Barton, P.I. & Tidor, B. The Per2 negative feedback loop sets the period in the mammalian circadian clock mechanism. *PLoS Comput Biol* **3**, e242 (2007).

(202) Loewer, A. & Lahav, G. We are all individuals: causes and consequences of non-genetic heterogeneity in mammalian cells. *Curr Opin Genet Dev* **21**, 753-8 (2011).

(203) Hu, W. *et al.* A single nucleotide polymorphism in the MDM2 gene disrupts the oscillation of p53 and MDM2 levels in cells. *Cancer Res* **67**, 2757-65 (2007).

(204) Bond, G.L. *et al.* A single nucleotide polymorphism in the MDM2 promoter attenuates the p53 tumor suppressor pathway and accelerates tumor formation in humans. *Cell* **119**, 591-602 (2004).

(205) Izhikevich, E.M. Resonance and selective communication via bursts in neurons having subthreshold oscillations. *Biosystems* **67**, 95-102 (2002).

(206) Hodgkin, A.L. The local electric changes associated with repetitive action in a non-medullated axon. *J Physiol* **107**, 165-81 (1948).

(207) Izhikevich, E.M., Desai, N.S., Walcott, E.C. & Hoppensteadt, F.C. Bursts as a unit of neural information: selective communication via resonance. *Trends Neurosci* **26**, 161-7 (2003).

(208) AIzhikevich, E.M. & Massachusetts Institute of Technology. Dynamical systems in neuroscience the geometry of excitability and bursting. 457 p. (MIT Press, Cambridge, Mass., 2007).

(209) Hansel, D., Mato, G. & Meunier, C. Synchrony in excitatory neural networks. *Neural Comput* **7**, 307-37 (1995).

(210) Peixoto, P.M., Ryu, S.Y., Pruzansky, D.P., Kuriakose, M., Gilmore, A. & Kinnally, K.W. Mitochondrial apoptosis is amplified through gap junctions. *Biochem Biophys Res Commun* **390**, 38-43 (2009).

(211) Banaz-Yasar, F., Lennartz, K., Winterhager, E. & Gellhaus, A. Radiation-induced bystander effects in malignant trophoblast cells are independent from gap junctional communication. *J Cell Biochem* **103**, 149-61 (2008).

(212) Brown, T.M., Colwell, C.S., Waschek, J.A. & Piggins, H.D. Disrupted neuronal activity rhythms in the suprachiasmatic nuclei of vasoactive intestinal polypeptide-deficient mice. *J Neurophysiol* **97**, 2553-8 (2007).

(213) Aton, S.J., Colwell, C.S., Harmar, A.J., Waschek, J. & Herzog, E.D. Vasoactive intestinal polypeptide mediates circadian rhythmicity and synchrony in mammalian clock neurons. *Nat Neurosci* **8**, 476-83 (2005).

(214) Ojima, M., Furutani, A., Ban, N. & Kai, M. Persistence of DNA double-strand breaks in normal human cells induced by radiation-induced bystander effect. *Radiat Res* **175**, 90-6 (2011).

(215) Rosenblum, M. & Pikovsky, A. Synchronization: from pendulum clocks to chaotic lasers and chemical oscillators. *Contemp Phys* **44**, 401-16 (2003).

(216) Sturrock, M., Terry, A.J., Xirodimas, D.P., Thompson, A.M. & Chaplain, M.A.J. Spatio-temporal modelling of the Hes1 and p53-Mdm2 intracellular signalling pathways. *J Theor Biol* **273**, 15-31 (2011).

(217) Sato, T.K. *et al.* A functional genomics strategy reveals rora as a component of the mammalian circadian clock. *Neuron* **43**, 527-37 (2004).

(218) Antoch, M.P. & Kondratov, R.V. Circadian Proteins and Genotoxic Stress Response. *Circ Res* **106**, 68-78 (2010).

(219) Filipski, E. *et al.* Effects of light and food schedules on liver and tumor molecular clocks in mice. *J Natl Cancer I* **97**, 507-17 (2005).

(220) He, Q. & Liu, Y. Molecular mechanism of light responses in Neurospora: from light-induced transcription to photoadaptation. *Genes Dev* **19**, 2888-99 (2005).

(221) Suter, D.M., Molina, N., Gatfield, D., Schneider, K., Schibler, U. & Naef, F. Mammalian genes are transcribed with widely different bursting kinetics. *Science* **332**, 472-4 (2011).

(222) Chawla, A. & Lazar, M.A. Induction of Rev-ErbA alpha, an orphan receptor encoded on the opposite strand of the alpha-thyroid hormone receptor gene, during adipocyte differentiation. *J Biol Chem* **268**, 16265-9 (1993).

(223) Thron, C.D. The secant condition for instability in biochemical feedback control. I. The role of cooperativity and saturability. *Bulletin of Mathematical Biology*, 383–401 (1991).

(224) Mallet-Paret, J. & Smith, H. The Poincare-Bendixon theorem for monotone cyclic feedback systems. *Journal of Dynamics and DIfferetial Equations* **2**, 367-421 (1990).

(225) Sontag, E.D. Passivity gains and the "secant condition" for stability. *Systems & Control Letters* **55**, 177-83 (2006).